A TRIDENT SCHOLAR PROJECT REPORT

NO. 459

Development of a Mechanically Mediated RF-to-Optical Transducer

by

Midshipman 1/C Christopher L. Panuski, USN

UNITED STATES NAVAL ACADEMY
ANNAPOLIS, MARYLAND

USNA-1531-2

REPORT DOCUMENTATION PAGE

Form Approved
OMB No. 0704-0188

1. REPORT DATE *(DD-MM-YYYY)*	**2. REPORT TYPE**	**3. DATES COVERED** *(From - To)*
05-22-17		

4. TITLE AND SUBTITLE
Development of a Mechanically Mediated RF-to-Optical Transducer

5a. CONTRACT NUMBER

5b. GRANT NUMBER

5c. PROGRAM ELEMENT NUMBER

6. AUTHOR(S)
Panuski, Christopher L.

5d. PROJECT NUMBER

5e. TASK NUMBER

5f. WORK UNIT NUMBER

7. PERFORMING ORGANIZATION NAME(S) AND ADDRESS(ES)

8. PERFORMING ORGANIZATION REPORT NUMBER

9. SPONSORING / MONITORING AGENCY NAME(S) AND ADDRESS(ES)
U.S. Naval Academy
Annapolis, MD 21402

10. SPONSOR/MONITOR'S ACRONYM(S)

11. SPONSOR/MONITOR'S REPORT NUMBER(S)
Trident Scholar Report no. 459 (2017)

12. DISTRIBUTION / AVAILABILITY STATEMENT

This document has been approved for public release; its distribution is UNLIMITED.

13. SUPPLEMENTARY NOTES

14. ABSTRACT

Detection and transmission of weak radio-frequency (RF) signals poses a significant challenge for modern electronic systems, in which lossy copper wires and thermal noise can corrupt sensitive information. Conversion, or "transduction" of these signals into the optical domain, however, enables enhanced detection sensitivity as well as long distance, low-loss transmission in optical fibers. Mechanically mediated transduction architectures, which rely upon the coupling of electronic and optical signals to a common mechanical oscillator, have sparked recent research interest for this application due to their ability to efficiently couple signals of drastically different frequencies. Here, extending upon previous work on sensitive optomechanical interactions, we explore a novel, fully integrated technique for RF-to-optical transduction. In the proposed system, an RF signal displaces a coupled mechanical resonator placed within the evanescent field of an optical waveguide. This resulting displacement subsequently induces an optical phase shift due to the resonator's proximity to the underlying optical waveguide. Placing this "phase shifter" within an interferometer enables sensitive optical phase detection, thus completing the conversion from an RF to an optical signal. To quantify the expected device performance, a theoretical model was developed and evaluated based upon the results of computational finite element simulations. A complete fabrication cycle was then conducted at the Naval Research Laboratory's Nanoscience Institute, which yielded devices for experimental verification of these conclusions and enabled a proof-of-concept implementation of the proposed architecture. This research thus provides a complete theoretical, computational, and experimental characterization of a novel scheme for RF-to-optical transduction which may have future applications for enhanced sensing and for fundamental research into coherent quantum state transfer.

15. SUBJECT TERMS
integrated photonics, micro-electro-mechanical systems, RF-to-optical transduction, mechanically mediated transduction, optomechanics, optical modulation

16. SECURITY CLASSIFICATION OF:			**17. LIMITATION OF ABSTRACT**	**18. NUMBER OF PAGES**	**19a. NAME OF RESPONSIBLE PERSON**
a. REPORT	**b. ABSTRACT**	**c. THIS PAGE**		80	**19b. TELEPHONE NUMBER** *(include area code)*

U.S.N.A. --- Trident Scholar project report; no. 459 (2017)

DEVELOPMENT OF A MECHANICALLY MEDIATED RF-TO-OPTICAL TRANSDUCER

by

Midshipman 1/C Christopher L. Panuski
United States Naval Academy
Annapolis, Maryland

Certification of Advisers Approval

Associate Professor R. Brian Jenkins
Electrical and Computer Engineering Department

_____
(signature)

_____
(date)

Professor Nicolas J. Frigo
Physics Department

_____
(signature)

_____
(date)

Associate Professor Deborah M. Mechtel
Electrical and Computer Engineering Department

_____
(signature)

_____
(date)

Professor Carl E. Mungan
Physics Department

_____
(signature)

_____
(date)

Acceptance for the Trident Scholar Committee

Professor Maria J. Schroeder
Associate Director of Midshipman Research

_____
(signature)

_____
(date)

USNA-1531-2

1 Abstract

Abstract

Detection and transmission of weak radio-frequency (RF) signals poses a significant challenge for modern electronic systems, in which lossy copper wires and thermal noise can corrupt sensitive information. Conversion, or "transduction" of these signals into the optical domain, however, enables enhanced detection sensitivity as well as long distance, low-loss transmission in optical fibers. Mechanically mediated transduction architectures, which rely upon the coupling of electronic and optical signals to a common mechanical oscillator, have sparked recent research interest for this application due to their ability to efficiently couple signals of drastically different frequencies. Recent advances in photonic integrated circuits (PICs), which enable the manufacture of complex optical circuits, have demonstrated the potential to integrate mechanical resonators into optical designs, and therefore serve as an ideal platform for transducer development.

Here, extending upon previous work on sensitive optomechanical interactions, we explore a novel, fully integrated technique for RF-to-optical transduction. In the proposed system, an RF signal displaces a coupled mechanical resonator placed within the evanescent field of an optical waveguide. This resulting displacement subsequently induces an optical phase shift due to the resonator's proximity to the underlying optical waveguide. Placing this "phase shifter" within an interferometer enables sensitive optical phase detection, thus completing the conversion from an RF to an optical signal. To quantify the expected device performance, a theoretical model was developed and evaluated based upon the results of computational finite element simulations. A complete fabrication cycle was then conducted at the Naval Research Laboratory's Nanoscience Institute, which yielded devices for experimental verification of these conclusions and enabled a proof-of-concept implementation of the proposed architecture. This research thus provides a complete theoretical, computational, and experimental characterization of a novel scheme for RF-to-optical transduction which may have future applications for enhanced sensing and for fundamental research into coherent quantum state transfer.

Keywords: integrated photonics, micro-electro-mechanical systems, RF-to-optical transduction, mechanically mediated transduction, optomechanics, optical modulation

2 Acknowledgments

There are unfortunately far too many people that I have to thank than can fit on this page...

I'll start with my advisors on this project at the Naval Academy, who have continuously and graciously offered me their knowledge, support, and expertise over the past few years. After intently searching for research projects to work on at the Academy, Professor Mungan was the first to bring me into his lab and to get me started working on an undergraduate research project. Around the same time, Professor Mechtel was my electromagnetics professor, and encouraged me to pursue my interests outside of the classroom. Prof. Jenkins, my academic and research adviser, has always been an excellent sounding board for ideas, and somehow still puts up with me randomly dropping by his office. Professor Frigo, who got the ball rolling on this project by putting me in touch with Dr. Stievater's group at the Naval Research Laboratory, never lets me walk away from our discussions without having learned something new and having thought of a new question (or wondering where his pop culture references come from).

It goes without saying that I couldn't be more thankful for the rest of my classroom professors and personal mentors that I've had at the Naval Academy, all of whom have developed me into the person who I am today. Capt Cory Kampf, Professor Firebaugh, Professor Blanco, Professor McCarthy, Professor Brereton, and LCDR Wood are a few of those who have been especially influential. Reaching back to my time at the North Carolina School of Science and Math, I think it's safe to say that I'd never be where I am today without having met Dr. John Kolena, who has been the ultimate teacher, mentor, and friend. Don't worry John, I'm still working on my cultural literacy...

At the Naval Research Laboratory, I can't thank Dr. Marcel Pruessner enough for letting me come to work with him and the rest of Code 5654 – without their support, this work surely would not have been possible. And of course, how could I not thank Dr. Dmitry Kozak for his constant jokes and for welcoming me into the underground NRL cleanroom arm wrestling bracket...

As for funding, I was fortunate enough to be supported by the USNA Trident Scholar program as well as the Stamps Leadership Scholarship. Their financial support was invaluable, and provided me with a wonderful experience that I'll always remember with great fondness.

Finally, I can never thank my family – my mother and father, as well as my two awesome brothers Patrick and Benjamin – enough for their support and never-ending sense of humor. You guys are the best.

Contents

3 Introduction

The transmission and detection of weak radio-frequency (RF) signals – signals with frequencies between 3 kHz and 300 MHz – is of direct importance to naval missions which rely upon precision signals intelligence, surveillance, and reconnaissance operations worldwide. However, these processes also pose a significant challenge for modern electronic systems, in which lossy copper wires and thermal noise can corrupt or mask sensitive information. Converting, or "transducing," these signals into optical signals, however, enables enhanced detection sensitivity as well as long distance, low-loss transmission in fiber optic systems [1].

Recent research in optomechanics, a growing field of investigation which explores the interaction between light and matter, has sparked interest in the study of of mechanically mediated transduction schemes, as RF and optical signals with drastically different frequencies can be coupled to a common mechanical resonator [3]. This approach has been experimentally verified in recent research [4, 5, 6]; however, the segmented architectures implemented in these studies impedes their integration into deployable systems.

The use of photonic integrated circuits (PICs) affords one possible avenue for integration of mechanical structures and micro-electro-mechanical systems (MEMS) into pre-existing optical technologies [13]. In general, the field of integrated photonics allows the traditionally segmented optics components used for optomechanical investigations to be combined into miniaturized circuits that can be easily fabricated using mature processes developed within the semiconductor transistor industry.

Here, we leverage these capabilities of integrated photonics to explore a novel, fully integrated electro-opto-mechanical technique for RF-to-optical transduction. Specifically, we extend upon a previous study [12] which investigated the tunable interaction between an electrostatically-actuated mechanical resonator and an on-chip optical signal. This technique is extended from a static DC characterization to a more general dynamic RF analysis. The proposed approach may have advantages over traditional transduction techniques such as thermo-optic and electro-optic methods which rely upon relatively weak effects and thus require significant input power or long interaction lengths to operate efficiently [2].

If fully integrated, an efficient electro-opto-mechanical transducer for RF and optical signals would serve as a compact, scalable solution for the sensitive detection of weak electrical signals – a feat of crucial importance for a variety of fields challenged with detection of small signals buried below thermal noise floors. Although this project involves a fundamental exploration of performance at the device level, several system-level applications could be envisioned given the realization of an ideal RF-to-optical transducer. For example, large, expensive, cryogenically-cooled pre-amplifiers used to eliminate thermal Johnson noise in radio astronomy receivers could be replaced by this noise-tolerant transducer, thus dramatically reducing the system's size and cost [7]. Such a transducer may also enable low-loss transmission of faint electronic signals or quantum coherent upconversion and transmission of sensitive low-frequency quantum states [4]. Seeing the numerous feasible defense applications, DARPA has initiated several projects to advance the constituent technologies involved within this project [8, 9].

However, before these future applications can be pursued, the appropriate underlying technologies must be fully explored and characterized. This research comprises a complete theoretical, computa-

tional, and experimental investigation of a newly proposed method for RF-to-optical transduction, and thus advances this ongoing active field of research.

4 Transduction Architecture

Due to their ability to transfer energy and information across different domains, transducers have become essential enablers of numerous technologies ranging from everyday smartphones and sensors to complex naval systems. A typical loudspeaker, for example, converts an input electrical signal into the mechanical motion of a membrane, which in turn produces an audible pressure wave in air – a physical representation of the original electronic information that can be readily interpreted by the human ear. Functioning in reverse, naval hydrophone arrays facilitate the conversion of acoustic signals, which propagate efficiently in an underwater environment, to electronic signals that are easily transmitted, processed, and stored in above-water computer systems.

The principal advantage demonstrated by these two examples – namely the ability to convert energy in one domain, such as electrical, optical, mechanical, or thermal, to energy contained in a more advantageous signal type – is echoed by RF-to-optical transducers. While RF signals may experience notable interference and loss in electronic systems, their placement onto an optical "carrier" enables isolated, low-loss transmission over hundreds of kilometers in optical fiber. The higher carrier frequencies characteristic of optical signals also provides for a larger data carrying capacity, or bandwidth. Of note for sensitive naval operations, both line-of-sight optical links as well as fiber-contained systems afford enhanced data security over traditional electronic transmission techniques, which can be intercepted with an appropriately placed antenna or wire-tap.

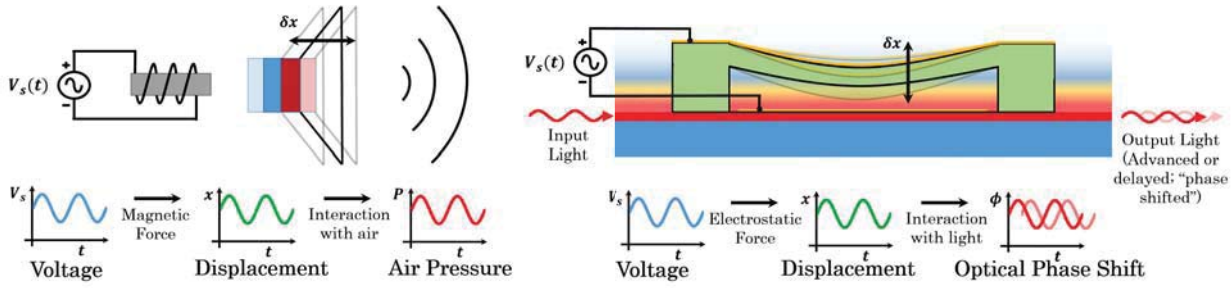

Figure 1: In a common loudspeaker, an input electrical signal is passed through a wire coil, thus producing an electrically-dependent magnetic field. Variations in this induced field displace a magnetic membrane. A pressure wave is then created through the diaphragm's interaction with the surrounding air. Likewise, the proposed electro-opto-mechanical transducer leverages the electrostatic force created by applying a bias voltage across a mechanical oscillator – a MEMS microbridge in this case – to yield a parametric displacement. As the microbridge enters more deeply into the "evanescent field" (pale blue to red in figure), it changes the index of refraction of the guided light ("input" to "output"). This, in turn, causes a small change in the optical phase of the output light.

As shown in Figure 1, our proposed transduction technique for this favorable conversion is an optical analog to the aforementioned loudspeaker. In both systems, a mechanical resonator is used to communicate interactions between the input and output signals. For these mechanically mediated transducers, two key conversions are required: 1) the input signal must first displace the mechanical device, and 2) this displacement must then impart some measurable change on a physical parameter of the output signal. In short, both the input and output signals must be mutually coupled to a common mechanical structure. For our proposed transduction architecture, we term these two required processes "electromechanical coupling" and "optomechanical coupling," respec-

tively. Substituting air for light as the medium of information transfer, the mechanically mediated RF-to-optical conversion process explored here can be qualitatively understood as an "optical loudspeaker" [1].

When integrated, the combination of these two processes yields a complete electro-opto-mechanical transducer. A block diagram of our proposed architecture is shown in Figure 2. In the following sections, each of the conversion processes are described for the proposed architecture.

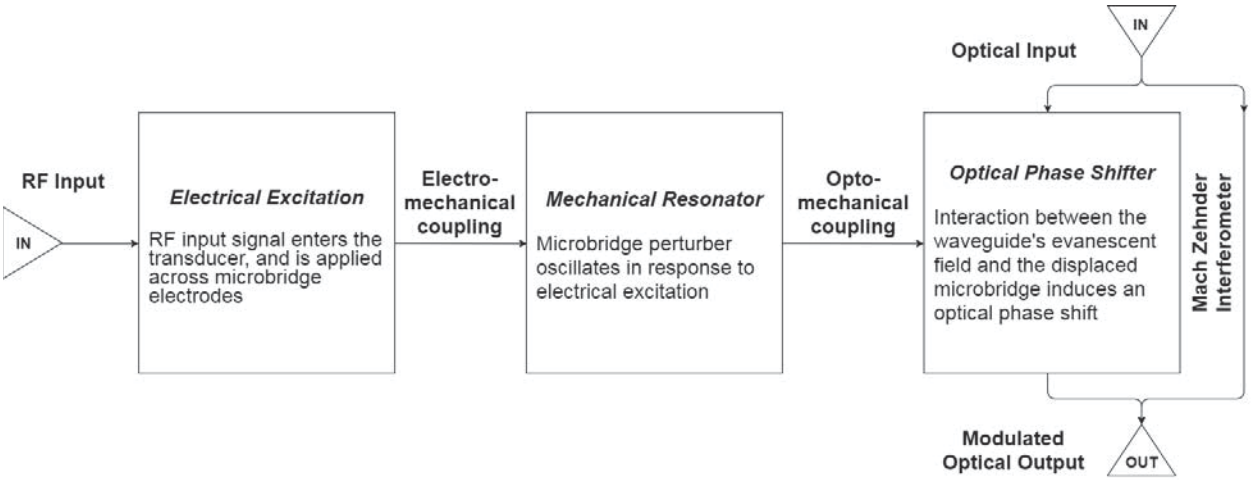

Figure 2: A schematic depiction of the proposed architecture. Electrical excitations displace a microbridge oscillator placed within the evanescent field of an optical signal, which in turn creates a variable optical phase shift. When integrated into a Mach-Zehnder interferometer – a sensitive phase detector – the resulting phase shift modulates the optical intensity at the interferometer's output. The effectiveness of the RF-to-mechanical and mechanical-to-optical conversion steps are governed by the electromechanical and optomechanical coupling parameters, G_{em} and G_{om} respectively.

4.1 Electromechanical Coupling

Here, an electrostatically actuated silicon nitride MEMS (micro-electro-mechanical system) doubly-clamped beam, or "microbridge" [10], is utilized as the system's mechanical resonator. An image of a typical bridge is provided in Figure 3. By applying a bias voltage between the suspended bridge's electrode and a vertically depressed side electrode, the bridge resembles a flexible capacitor which can be displaced in a controlled manner via the electrostatic force, $\vec{F}^{\text{bridge}}_{\text{electrostatic}} = -\nabla U_{\text{capacitor}}$, where $U_{\text{capacitor}}$ is the potential energy stored in the microbridge capacitor. The coupling efficiency of this method is theoretically evaluated in Section 5. As a proposed improvement to the electromechanical coupling, the microbridge can be integrated as a portion of the capacitive element of a LC electrical resonator. This approach, which multiplies the effective voltage applied to the microbridge, is further explored in Appendix C.

4.2 Optomechanical Coupling

By placing the MEMS microbridge within the evanescent electric field of a propagating optical signal, any electrically-induced bridge displacement yields a slight shift of the optical signal in time, i.e., a "phase shift," due to a variable optomechanical interaction. The physical mechanism for this

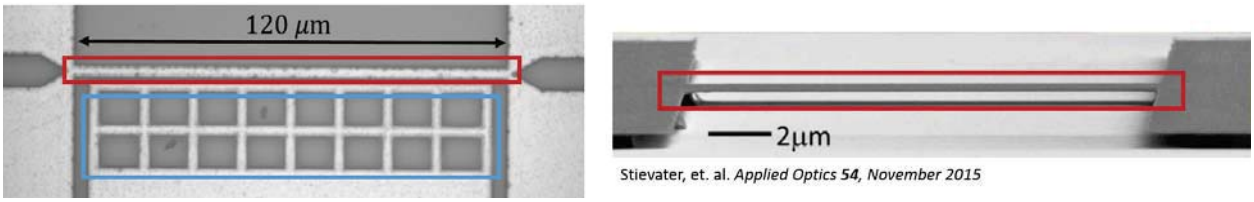

Figure 3: Images of suspended microbridges. An overhead view of a 120 μm MEMS silicon nitride suspended microbridge (red box) with actuation electrodes is shown on the left, while a side profile of a shorter suspended bridge (red), depicting a visible air gap between the bridge and substrate, is on the right. An applied bias between the bridge (red) and side (blue) electrodes can be used to displace the microbridge.

phase shift is further described here.

To achieve compatibility with existing integrated photonic designs, the mechanical microbridge is suspended directly above and parallel to an underlying optical waveguide, or "wire" for light. Similar to an optical fiber, this waveguide features a core material with a larger index of refraction "n" than its surrounding layers (air above and silicon dioxide insulator below), and thus utilizes the principle of total internal reflection to guide optical signals. Furthermore, the specific waveguide implemented in this investigation is specifically designed [11] to maximize the fraction of optical field lying outside of the waveguide's core. This exponentially decaying residual electromagnetic field is known as the "evanescent field," and extends well into the air and oxide layers surrounding the waveguide core. A two-dimensional cross section of these elements is illustrated in Figure 4.

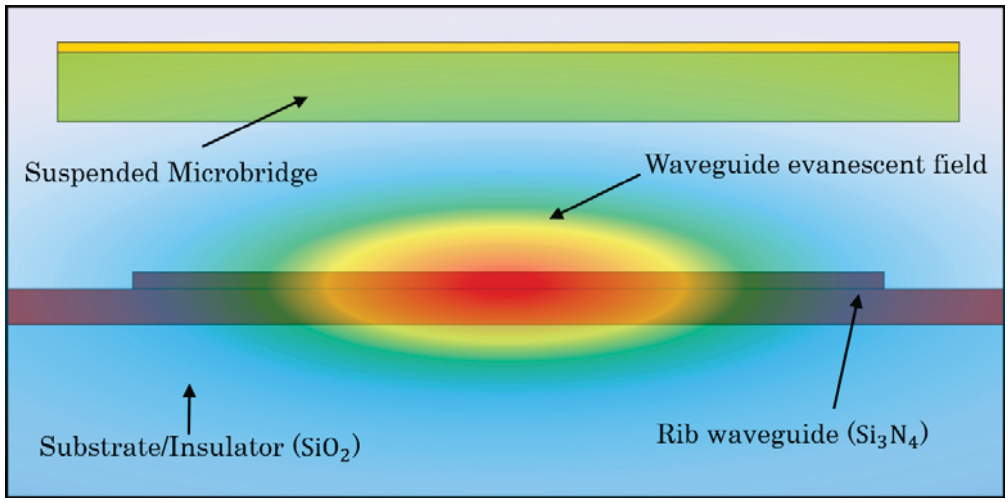

Figure 4: A illustration of the optomechanical device's cross section. A suspended microbridge (green) is displaced vertically above an underlying waveguide. The weakly confining silicon nitride rib waveguide (red) is specifically designed to maximize the evanescent field.

When actuated with an electric signal, the bridge penetrates deeper into the evanescent field, thus producing a variable optical phase shift in the waveguide. More precisely, an optical phase shift is created by changing the effective index of refraction n_{eff} in the waveguide near the displaced bridge. Since the overall phase change, from input to output, is determined by n_{eff}, small changes in this parameter result in changes in the optical phase. The effective index, determined by evalu-

ating the confinement of the optical mode within several materials with different refractive indices, determines the phase propagation speed of light in the region, i.e. $v_{\text{phase}} = c/n_{\text{eff}}$. Therefore, a change in n_{eff} will change the speed of light in the region, thus inducing an optical phase shift relative to the signal in the region characterized by the unmodified effective index. This evanescent field perturbation method, further described in [11], has been utilized in previous devices to create sensitive optical phase shift elements [12].

In the proposed architecture, the effective index is efficiently tuned through this evanescent field perturbation method. As depicted by the simulated optical mode profiles shown in Figure 5, displacing a silicon nitride ($n \approx 1.8$) microbridge further into the evanescent field increases the effective index, since the optical confinement within the bridge, whose refractive index is greater than that of air ($n = 1$), increases. As an analogy, consider the waveguide signal to be a fast moving lane of traffic on a highway, and the microbridge to be a lane filled with slow-moving traffic. When the traffic in the fast lane can not see the slow traffic, the cars continue along at their original speed. However, when the slow traffic is in sight – an analog of the microbridge being lowered further into the optical signal – the fast moving cars naturally slow down as well. Just as the proximity to slow moving traffic influences the average speed of cars on the highway, the height of the microbridge affects the speed of the optical signal in the waveguide, causing it to shift in time.

Consequently, the coupled microbridge-waveguide optomechanical arrangement forms a sensitive, tunable phase shift element which can be used to effectively modify the properties of an optical signal in response to a mechanical displacement, thus achieving the second required step for an RF-to-optical transducer. When combined with the electrostatic control of the microbridge's displacement through the applied bias voltage, the apparatus constitutes a completely integrated device for converting RF input signals into optical phase shifts.

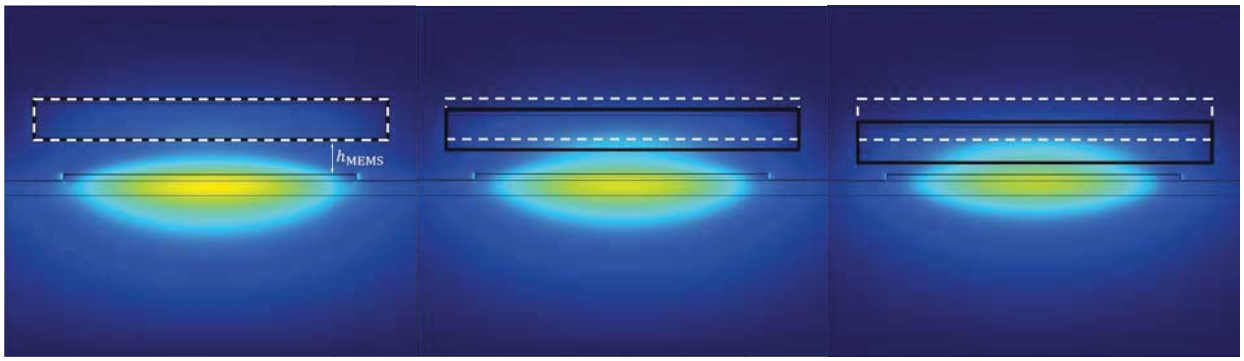

(a) $h_{\text{MEMS}} = 300$ nm, $n_{\text{eff}} = 1.53$ (b) $h_{\text{MEMS}} = 200$ nm, $n_{\text{eff}} = 1.55$ (c) $h_{\text{MEMS}} = 100$ nm, $n_{\text{eff}} = 1.59$

Figure 5: Simulated mode profiles of the weakly-confined rib waveguide described earlier [12] at 1550 nm. The magnitude of the horizontal electric field of the fundamental TE mode is represented in color, with blue being the smallest and orange being largest. As h_{MEMS}, the height of the air gap between the MEMS perturber and the underlying waveguide, decreases, the effective index increases exponentially due to greater optical confinement within the silicon nitride perturber ($n \approx 1.8$).

4.3 Phase Shift Readout

The microbridge phase shift element can be incorporated into an integrated photonic interferometer, which, serving as a sensitive phase detector, converts small changes in optical phase into easily measurable variations in output light intensity. Figure 6 details the key components of the Mach-Zehnder interferometers (MZIs) used in this research. In an MZI, input light is separated into two separate waveguide "arms." When these arms are of equal length and no internal phase shift is added to either arm, the two independent optical signals propagate through to a recombination point at the interferometer output, where they constructively interfere to yield an output signal with an equal amplitude as that of the input. Otherwise, if the arms contain a discrete path length imbalance, the two recombined signals at the interferometer output have a constant phase imbalance $\Delta\phi$ which leads to a modified output intensity. For example, if one of the arms is half an optical wavelength longer than the other, the recombined signals will be π radians out of phase, and will destructively interfere upon recombination to yield zero output intensity.

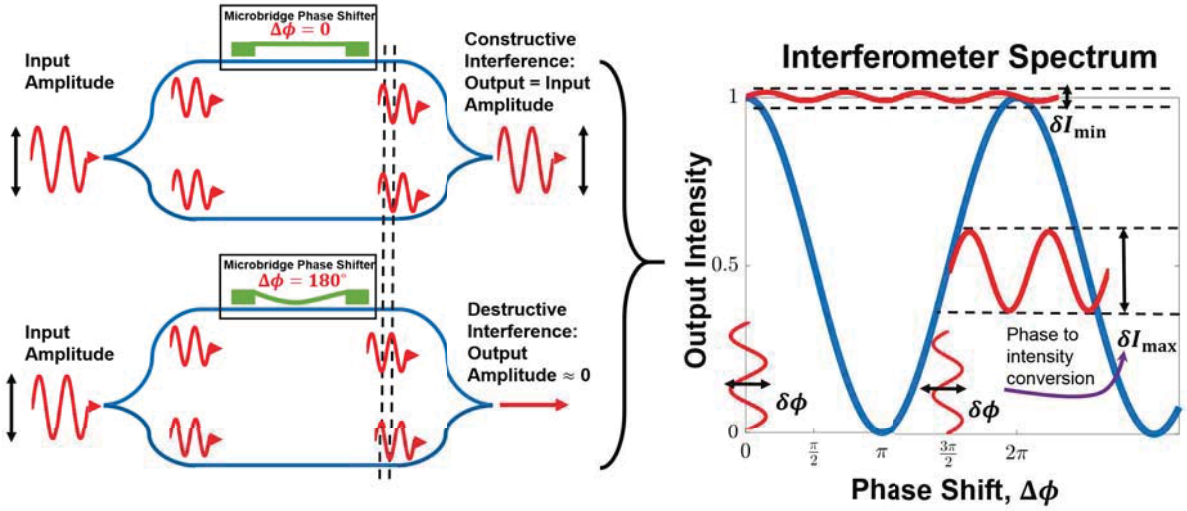

Figure 6: A Mach-Zehnder interferometer (MZI) can be used to convert small changes in phase induced by microbridge displacements into intensity variations in the interferometer's output signal. As depicted on the left, an MZI splits incident continuous wave laser light into two "arms." In one arm, the light is delayed due to the presence of the electrically-controlled microbridge perturber. Thus, the intensity of the recombined output light is dependent upon the phase shift imparted within the interferometer, and obeys a sinusoidal dependence on this phase imbalance.

The phase imbalance can be tuned by introducing an internal optical phase shift to *one* of the interferometer arms. As previously mentioned, the mechanical microbridge coupled to the underlying interferometer waveguide serves as this phase shifter for our study. Assuming a phase-matched condition in the absence of this perturber, the output optical intensity will vary according to the MZI transfer function

$$I_o = \frac{I_i}{2}[1 + cos(\Delta\phi)], \tag{1}$$

where I_o and I_i are the output and input optical intensities, respectively, and $\Delta\phi$ is the bridge-induced phase shift. This relationship between output optical intensity and overall phase imbalance

$\Delta\phi$ results in the continuous curve shown on the RHS in Figure 6.

The overall phase shift can be described usefully as composed of two parts: a constant "DC" component $\Delta\phi_0$ and a time-varying "ac" component $\delta\phi$. At any instant of time, the output intensity can be read off the blue curve's dependence on the overall phase at that time. Figure 6 shows two cases in which the DC component of the overall phase is changed while the ac component is a given sinusoidal signal. When the DC component is $\Delta\phi_0 = \frac{3\pi}{2}$, the operating point for the interferometer rides up and down the steep part of the blue curve. This creates an optical intensity which is detected as a voltage variation $\delta V_{\max}$. On the other hand, if the DC component were $\Delta\phi_0 = 0$ (left trace) the operating point would oscillate along the top of the cosine curve and give a limited output signal, $\delta V_{\min}$.

Thus, with a constant DC bias applied to the microbridge, a set phase shift $\Delta\phi$, which depends on the change in optomechanical coupling between the bridge and underlying waveguide, is realized. If an RF signal is then applied to the bridge, small mechanical oscillations will yield corresponding fluctuations $\delta\phi$ in the interferometer phase imbalance. These fluctuations, depicted as vertical red sinusoids in Figure 6, yield different output intensity fluctuation amplitudes depending upon the DC bias point. Theoretically, the maximum output fluctuation amplitude is achieved when tuned to a half-power point in which $I_o(\Delta\phi) = I_i/2$. This optimal operation point can be achieved in several ways: a fixed length imbalance between the arms; a DC voltage applied to the microbridge; or adjustment of the optical wavelength of light on the interferometer. This last method is the most practical, for reasons to be discussed later. From a communications perspective, the MZI enables the conversion of phase modulation within the interferometer arm to amplitude modulation of the recombined output signal.

A complete derivation of the theoretical MZI transfer function relating variations in phase, effective index, wavelength, and physical path length imbalance to output intensity is provided in Appendix B. Its characteristics are further discussed in Section 5.

4.4 Summary

In this section, we have introduced the enabling technologies which comprise the proposed RF-to-optical transduction architecture. Namely, the implementation of an electrostatically actuated microbridge realizes the RF-to-optical transduction requirement for an electrically controllable displacement of a mechanical resonator. The conversion of displacement to an optical phase shift is achieved by placing the mechanical microbridge within the evanescent field of a weakly confined silicon nitride waveguide. Finally, the RF-to-optical conversion process is completed by integrating the microbridge phase shifter into an arm of a Mach-Zehnder interferometer, a placement which enables the optical readout of small phase changes as variations in intensity. Given this background, the overall device theoretical transfer function and performance will now be introduced.

5 Transduction Theory

The theory involved with maximizing the optomechanical coupling strength through the optimization of various waveguide parameters has been previously described [11, 12]. In this section, the performance of the proposed electromechanical coupling technique (Section 4.1), which governs the effectiveness of converting an input voltage into a mechanical microbridge displacement, is explored and a device transfer function is proposed.

Using the electro-opto-mechanical effective index tuning methodology described in Section 4 [12, 2], a simple "bare" architecture can be developed for electromechanical coupling. In this mechanically mediated transducer, a flexible microbridge is electrostatically actuated by grounding an electrode patterned on the bridge and applying a bias voltage to a neighboring side electrode, as shown in Figure 7. A theoretical performance analysis can be conducted using a Lagrangian approach (see Appendix A for a complete derivation). The resulting transfer function,

$$T_{\text{bare}} = \underbrace{\frac{\delta\Phi(j\omega)}{\delta V_s(j\omega)}}_{\text{gain}} = \frac{2\pi}{\lambda} G_{om} L_{\text{MEMS}} \chi_m^0(j\omega) \frac{\partial C(x)}{\partial x}\bigg|_{x=x_0} V_{\text{dc}}, \tag{2}$$

correlates small input signal fluctuations δV_s to the resulting optical phase shift $\delta\Phi$ that they induce. In this function, λ is the wavelength of the laser input into the interferometer, V_{dc} is the DC bias voltage used to displace the microbridge to an equilibrium position, $\chi_m^0 \equiv \frac{\delta X(j\omega)}{\delta F_{\text{ext}}(j\omega)}\Big|_{\delta V_s=0} = \frac{1}{m(\Omega_m^2-\omega^2-j\omega\Gamma_m)}$ (in units of [m/N]) is the mechanical susceptibility (force to displacement transfer function) of a microbridge with mass m, resonant frequency Ω_m, and damping rate Γ_m, L_{MEMS} is the microbridge length, $G_{om} \equiv \partial n_{\text{eff}}/\partial x$ is the optomechanical coupling coefficient, and $C(x)$ is the displacement-dependent microbridge capacitance. The transfer function can thus be seen as the product of 1) the susceptibility to a driving signal $V_s(t)$ (i.e. $\chi_m^0 \frac{\partial C(x)}{\partial x}|_{x=x_0} V_{\text{dc}}$) and 2) the optical phase shift per unit displacement (i.e. $\frac{2\pi}{\lambda} G_{om} L_{\text{MEMS}}$). Introducing the electromechanical coupling parameter $G_{em} = |\chi_m^0 \frac{\partial C(x)}{\partial x}|_{x=x_0} V_{\text{dc}}|$, the transduction gain can be rewritten as

$$|T_{\text{bare}}| = \frac{2\pi}{\lambda} G_{om} G_{em} L_{\text{MEMS}}.$$

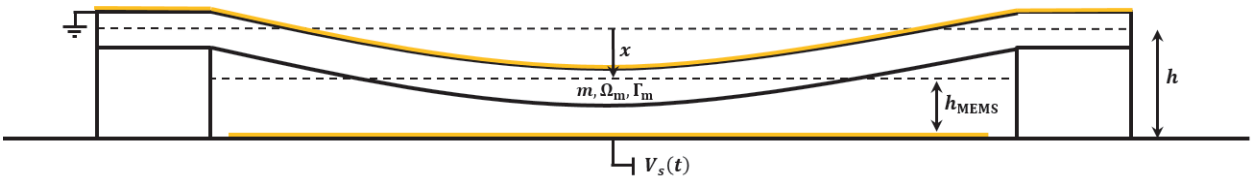

Figure 7: A bare transducer includes a microbridge resonator of length L_{MEMS}, mass m, resonant frequency Ω_m, and damping rate Γ_m that is electrostatically actuated by a source potential $V_s(t)$ placed between the bridge ground and an underlying electrode. The center of mass of the unactuated bridge rests at a height h above the underlying electrode, but is displaced a distance x by the applied electrostatic force. The height h_{MEMS} represents the average gap between the microbridge and underlying electrode. The underlying optical waveguide is not pictured.

For a combined DC and RF bias $V(t) = V_{DC} + \delta V_s(t)$, the resulting optical phase shift is similarly composed of small oscillations about a fixed bias point (i.e. $\Delta\phi(t) = \Delta\phi_0 + \delta\phi(t)$). Given the

bridge's placement within the integrated MZI, this phase shift produced by bridge motion modifies the interferometer output intensity, which is read out as a voltage V_{out} on a photodetector. Since the detected voltage is proportional to the optical intensity, the amplitude of output voltage fluctuations δV_{out} for a given $\delta\phi$ can be found by differentiating Equation 1 to find

$$\frac{\delta V_{\text{out}}}{\delta \phi} = -\frac{V_i}{2}\sin(\Delta\phi_0), \tag{3}$$

where $\Delta\phi_0$ is the equilibrium interferometer phase offset and V_i is the maximum output voltage which corresponds to the input power in a lossless configuration. When biased at a half power point ($\Delta\phi_0 = \pi/2, 3\pi/2, 5\pi/2, ...$) – typically adjusted by varying the input wavelength due to the built in physical path length difference between the two arms of the interferometer – the maximum amplitude of the output voltage fluctuations is found to be

$$\delta V_{\text{out}} = \frac{V_i}{2}\delta\phi.$$

This relationship is of fundamental importance to the experimental testing described in Section 10, as it connects the desired transfer function quantity $\delta\phi$ to the measured parameter δV_{out} to enable the transduction gain $|\delta\phi/\delta V_s|$ to be quantified.

In future design iterations, an integrated LC circuit can be fabricated to improve the electromechanical coupling performance. This method, thoroughly explored in Appendices A and C, amplifies the voltage across the microbridge capacitor by a factor of Q_{LC}, the quality factor of the coupled LC circuit.

5.1 Overview and Direction

The transfer function described here enables a quantitative performance analysis of the entire RF-to-optical transduction system. Mirroring the dependence qualitatively described in Section 4, the transduction gain – the magnitude of the transfer function $|T_{\text{bare}}|$ – depends on the efficiency of two processes: 1) the displacement resulting from an applied electrical bias, and 2) the phase shift resulting from that electrically-induced displacement. Next, we explore the electromechanical and optomechanical coupling strengths through a variety of computational multiphysics simulations, and combine these results to predict the overall transduction performance. After establishing this baseline numerical understanding of the system, the fabrication of test devices followed by an experimental verification of the proposed behavior will be described.

6 Electromechanical Simulation

To characterize the electromechanical system and quantify the expected electromechanical coupling coefficient G_{em} for our device architecture, a computational FEM model was developed in COMSOL [21] for several different geometries. These models were subsequently used to simulate the displacement of an electrostatically actuated microbridge under various conditions.

6.1 Geometries

Three different geometries, shown in Figure 8, were created in COMSOL: one to model a bare microbridge, and two to model the principal electrostatic actuation techniques – direct electrostatic actuation and Kelvin polarization force-based actuation.

(a) Bare (b) Direct Electrostatic (c) Kelvin Polarization Force

Figure 8: Three different geometries designed for FEM simulations in COMSOL. The bare device consists of a silicon nitride (SiN_x) MEMS resonator supported by oxide posts which rest on a thin Si_3N_4 layer with underlying oxide. Gold electrodes are patterned on and beside the bridge for direct electrostatic actuation, while two side electrodes are patterned beside the bare bridge for the polarization-induced actuation.

Parameter	Value	Description
L_{MEMS}	100 μm	Length of microbridge
w_{MEMS}	3 μm	Width of microbridge
t_{MEMS}	300 nm	Microbridge thickness
h_{MEMS}	230 nm	Thickness of oxide posts supporting microbridge
$t_{Si_3N_4}$	175 nm	Thickness of stoichiometric silicon nitride layer above oxide
t_{SiO_2}	5 μm	Thickness of buried oxide
$\mathbf{S}_{0,11/22}$	variable	Horizontal (x/y) intrinsic stress in PECVD microbridge

Table 1: Geometry dimensions and parameters for bare microbridge architecture in COMSOL.

The bare geometry shown in Figure 8a was developed to study the mechanical oscillator dynamics of a silicon nitride (PECVD SiN_x) microbridge resonator. The model consists of a 175 nm thick stoichiometric silicon nitride (Si_3N_4, shown in red) layer placed above a 5 μm thick silicon dioxide layer (blue). Two 230 nm thick oxide posts (green) are placed at either end of the structure to support a variable length, 300 nm thick SiN_x microbridge (green). A 5 μm thick layer of air overlies

the entire geometry. A summary of the model dimensions is provided in Table 1. The material parameters for the plasma-enhanced chemical vapor deposited (PECVD) materials used to construct the silicon nitride microbridge, which vary depending upon the deposition technique and method, were taken from [18].

The two models developed to study electrostatic actuation of the microbridge resembled a similar geometry, but were slightly modified in order to replicate the two principal electrostatic actuation methods. For the direct electrostatic actuation geometry shown in Figure 8b, a 35 nm thick side and bridge electrode were patterned. The side electrode, horizontally displaced 1 μm from the bridge, lies on a 300 nm thick PECVD silicon nitride layer to mimic the fabrication process [12]. For direct electrostatic actuation, a bias voltage placed between these two electrodes creates an electrostatic force which displaces the microbridge. The microbridge thickness for the modified geometry was also increased to 300 nm to account for the gold plated bridge, which protects the underlying silicon nitride from etching during the fabrication process [12].

The Kelvin polarization force-based actuation geometry (Figure 8c) adds two 55 nm thick gold electrodes on the stoichiometric silicon nitride layer beside the microbridge with a default spacing of 4 μm between electrodes. In this configuration, electrostatic displacement is achieved via the inhomogenious gradient electric field created by a bias placed between the electrodes. The electric field polarizes the dielectric and results in an attractive force, the Kelvin polarization force, on the microbridge towards the underlying electrodes [22, 23]. As demonstrated in Appendix F, this method proves to be a less efficient method for displacing the microbridge. Therefore, the direct electrostatic architecture was chosen for use in the following studies.

6.2 Resonant Frequency

Initial simulations focused on characterizing the unbiased microbridge's resonant frequency, along with its scaling with respect to changes in various dimensions and parameters. Visualization of the fundamental bridge modes (Figure 9) demonstrates that the first order mode, along with several subsequent, is a flexural mode. Furthermore, the initial results quantify the fundamental resonance for a 100 micron bridge to be on the order of 1 MHz.

As illustrated in Figure 10, the fundamental resonance frequency for the microbridge decreases as the length of the bridge is increased. Furthermore, the addition of a patterned 35 nm gold electrode atop the resonator yields a slight (on the order of 10%) decrease in resonant frequency.

Using an intrinsic stress of 100 MPa, a value listed in [12], the simulated fundamental resonant frequencies decrease by a factor of approximately 2.5. The dependence of resonance frequency upon intrinsic stress is depicted in Figure 11[1]. Since the actual film stress is variable and highly dependent upon the deposition technique (see Section 9), an experimental measurement of stress [47] in required to resolve this ambiguity.

[1]Of note, highly stressed PECVD silicon nitride films have demonstrated great promise for optomechanical applications due to their uncharacteristically large quality factors, which can be primarily attributed to an increasing resonant frequency with a nearly constant damping rate as intrinsic stress increases [20, 24]. Although higher resonant frequencies are not necessarily of direct benefit for a RF-to-optical transducer (see Appendix C for a thorough discussion), the effect of stress upon the oscillator dynamics should still be studied and understood for other potential applications in which the maximum possible coupling strength is desired.

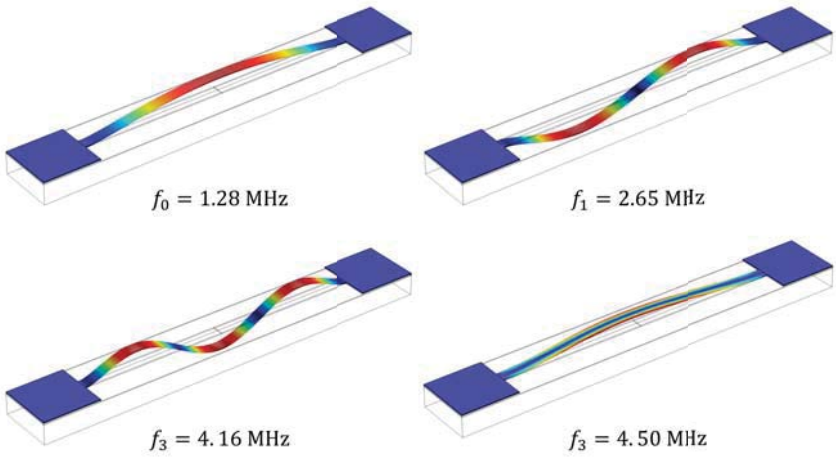

Figure 9: The first four fundamental resonance modes of a 75 micron long silicon nitride resonator with 100 MPa of intrinsic stress. The first three modes are flexural, while the fourth is torsional [10].

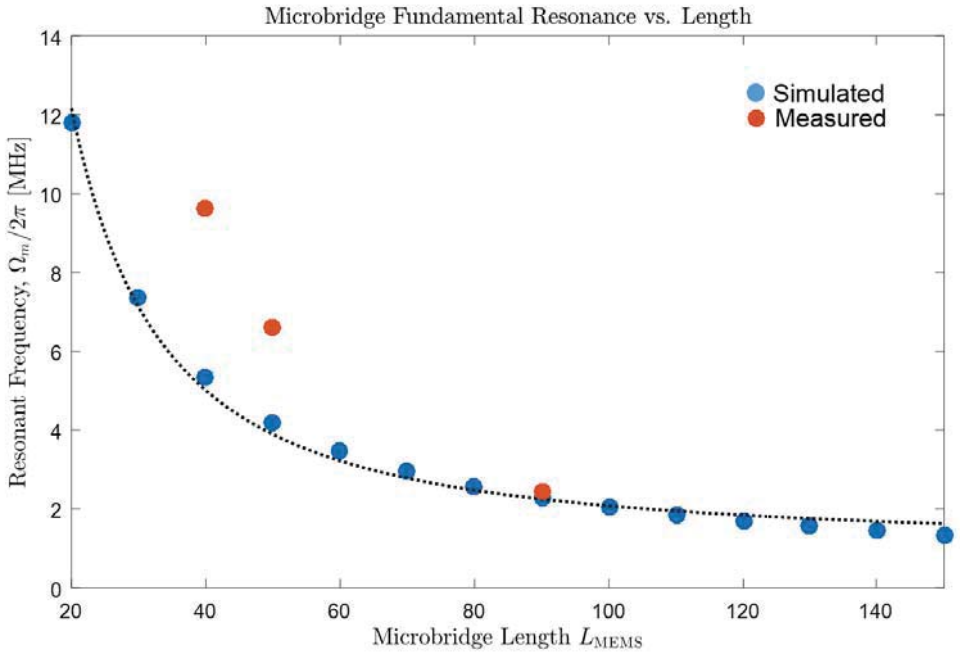

Figure 10: Fundamental resonance frequency vs. length for a SiN_x membrane with a 35 nm gold electrode. The dashed line, representing a $\Omega_m \propto L_{\mathrm{MEMS}}^{-3/2}$ curve fit, demonstrates excellent agreement between the simulated result and the trend predicted by Euler-Bernoulli beam theory. For these simulations, the intrinsic stress has been set to 1000 MPa to better approximate the resonances measured in this project, which are shown in red. Differences between the measured and simulated resonances are attributed to small variations between the simulated and measured geometries and physical parameters.

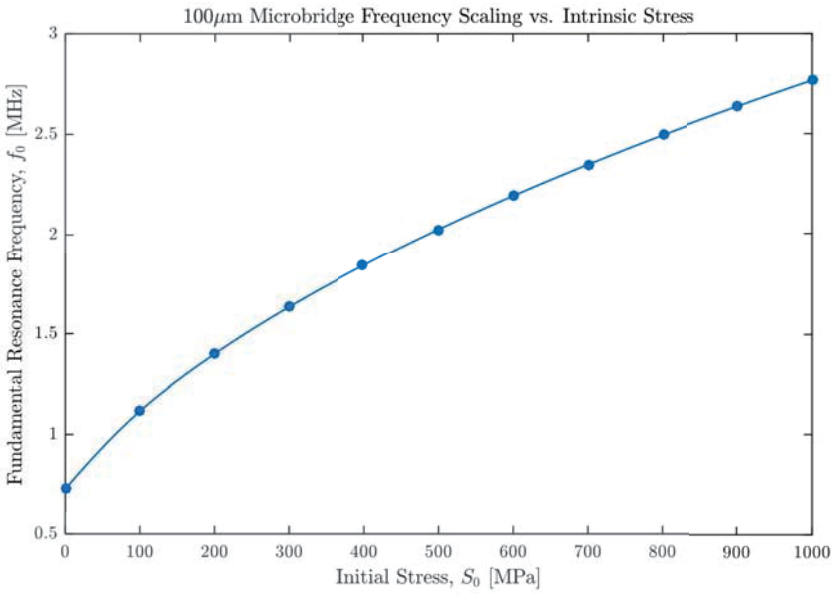

Figure 11: Fundamental resonance scaling for a 100 μm microbridge under varying levels of intrinsic stress (in-plane).

6.3 DC Bias Study

Following simulation of the bare microbridge, the direct electrostatic actuation-based architecture was studied. For these simulations, a variable DC bias was applied between the bridge and side electrode for bridges of variable length. For each bias point, the average displacement, capacitance, and resonant frequency were calculated. Figure 12 demonstrates the typical microbridge displacement profiles generated during the tests. Initially, under no DC bias, the bridge is slightly (by $<$ 1nm) bowed upwards due to the intrinsic stress within the silicon nitride. However, as the DC bias increases, the bridge is gradually displaced towards the underlying silicon nitride layer until the MEMS pull-in voltage [25] is reached (at which point a small increase in the DC bias quickly pulls the bridge into contact with the underlying silicon nitride). Note that, due to the aspect ratio of the bridge and electrode geometry, the horizontal displacement of the bridge is negligible [11].

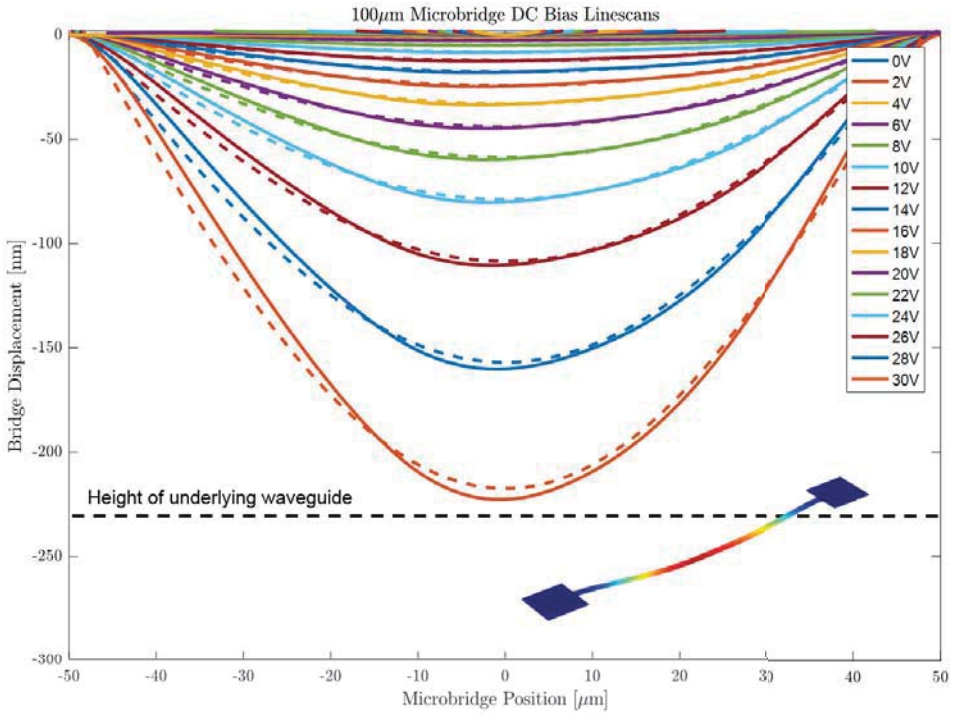

Figure 12: Displacement profiles of a 100 micron long microbridge under a DC bias placed between bridge and side electrodes. The dashed lines, representing a cosine function fit to each profile, closely model the computed displacement. The rate of displacement increases until the pull-in voltage [25] is met, at which point the bridge is clamped downwards and contacts the underlying waveguide. Given a default air gap of 230 nm, the pull-in condition is met at ∼30V.

6.3.1 Capacitive Spring Softening

As predicted by Equation 13 in Appendix A, the resonant frequency of the bridge is expected to decrease with respect to the square of the applied DC bias. Comparing the bridge to a simple spring, this decrease in resonance frequency corresponds to a reduced spring constant, or "spring softening" [51]. The computationally simulated eigenfrequencies at various DC biases, shown in Figure 13, confirms this relationship, and therefore serves as a partial verification of the theoretical model used to derive the device transfer function.

Experimentally, the spring softening effect can also be analyzed for comparison to the computational results and to better characterize the overall system.

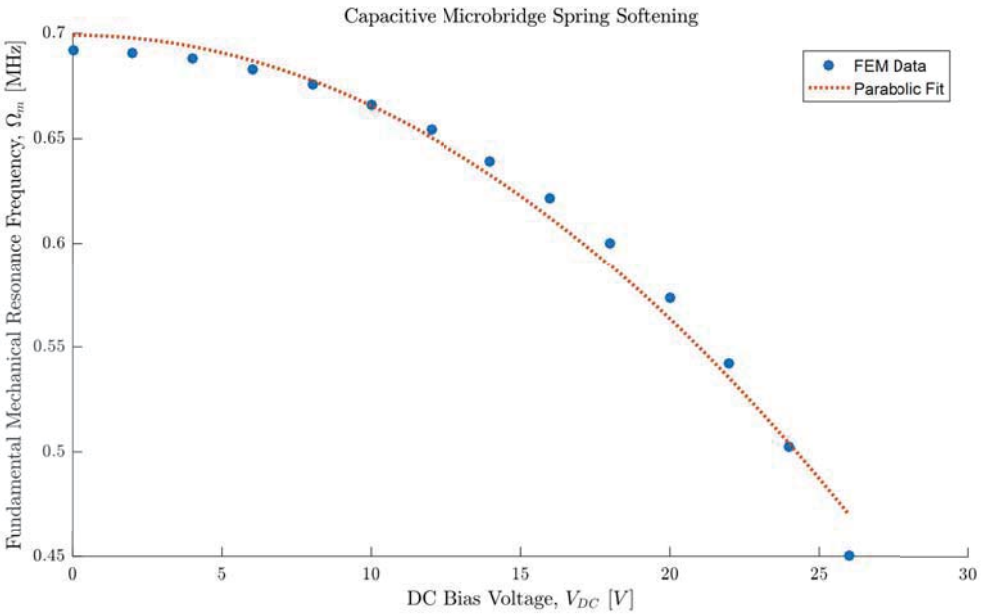

Figure 13: As expected, the resonant frequency for the biased device decreases with respect to the square of the applied DC bias voltage. This serves as a baseline verification of the theoretical model used to represent the electrostatic system.

6.3.2 Electrostatic Tuning

The principal goals of the DC bias studies were to characterize the efficiency of electrostatic actuation, i.e. the mechanical displacement that is generated from an applied bias voltage. For each bias point, the average gap between the microbridge's bottom surface and underlying silicon nitride layer was calculated. The capacitance was also computed, thus enabling the calculation of the energy required for a given displacement. The results of these FEM simulations for various bridge lengths are shown in Figure 14.

The electrostatic gap tuning results demonstrate that the rate of displacement with respect to the applied DC bias increases dramatically as the bias approaches the MEMS pull-in voltage. Since the bridge displacement directly affects the spacing between the two electrodes, the device capacitance demonstrates a similar characteristic. Therefore, since $G_{em} \propto \partial C(x_0)/\partial x$, biasing the device closer to the pull-in voltage will yield the strongest electromechanical coupling.

The energy required to displace the microbridge is also of interest, and is a key benefit of the proposed architecture. The advantage of an electrostatically-actuated phase shifter is that the tuning energy required is simply a function of the capacitance. As opposed to thermo-optic phase shifters and tuners, which require continuous power, the capacitor energy $\frac{1}{2}C(x_0)V_{dc}^2$ is the only energy required to displace the microbridge to the desired position, assuming no leakage [26]. Furthermore, for the simulated devices the tuning energy is on the order of 1 pJ. The utility of this remarkable metric is immediately realized when considering the demands of modern integrated photonic circuits, which may, for example, include networks of numerous ring resonators [27]. With manufacturing variability, these optical resonators all need to be tuned to the appropriate resonant frequency [28] – a task that is currently accomplished with thermo-optic heaters which require continuous power. An electrostatically-actuated microbridge tuner would serve as a much lower

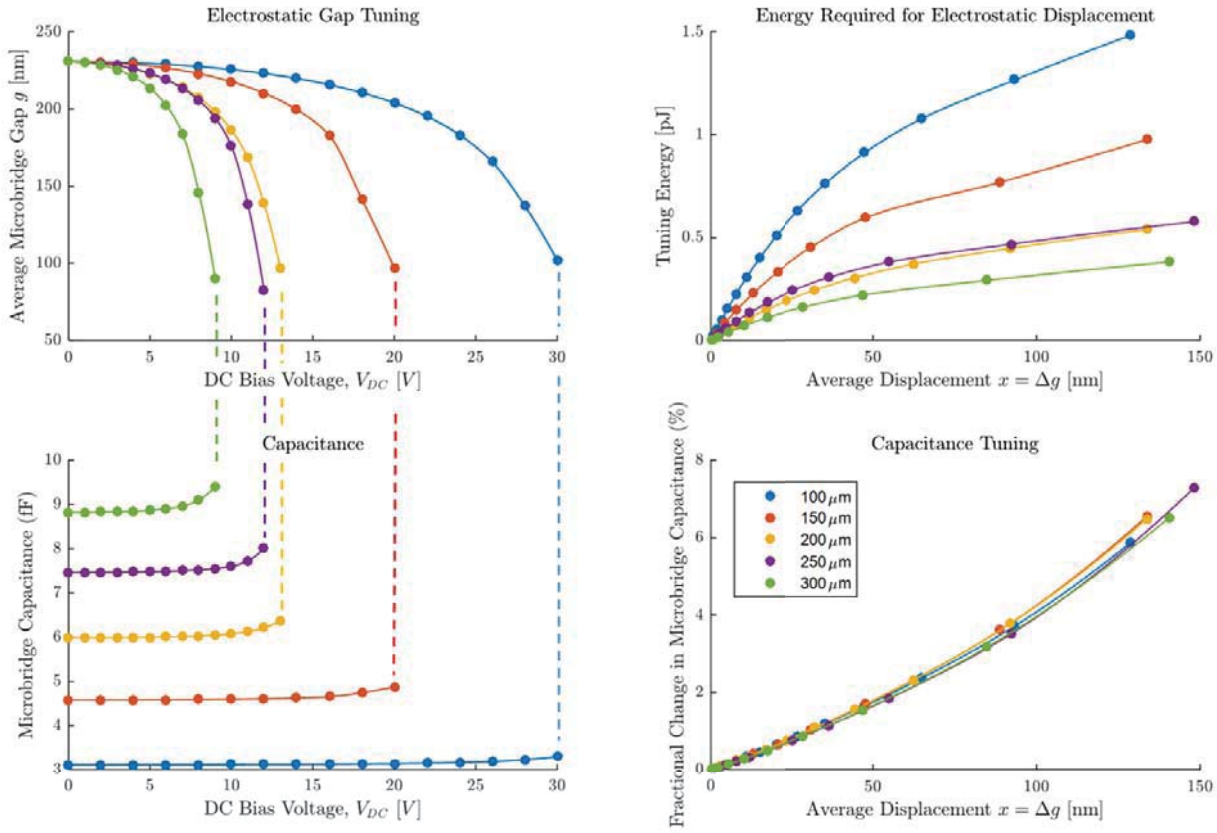

Figure 14: DC bias electrostatic actuation study results for various microbridge lengths (shown as different colors). As L_{MEMS} increases, the pull-in voltage (dashed lines) decreases along with the energy required for a given displacement distance. Capacitance, however, increases due to the increasing surface area of the electrodes. Fractional change in capacitance versus displacement is approximately equal, as expected from the constant device geometry.

power alternative, especially for large-scale networks where several tuning elements are required.

The results also indicate that the displacement and capacitance tuning are directly affected by the microbridge length L_{MEMS}. Due to the increase in mechanical compliance with bridge length, the pull-in voltage decreases with an increasing length. The bridge electrode surface area also increases for longer bridges, leading to a larger overall capacitance and a larger change in capacitance as the bridge is actuated. Despite this increase in capacitance, the energy required to actuate longer bridges decreases due to the decreased bias voltage required for a given displacement. As expected, the fractional capacitance change as a function of displacement is essentially constant regardless of microbridge length.

6.4 Summary

By conducting electromechanical DC bias tests, a mechanical displacement vs. bias curve, similar to that for a 100μm bridge shown in Figure 15, can be simulated. The results of these tests

quantify the first step of the RF-to-optical transduction process – electromechanical coupling. The displacement vs. bias curves also reveal that, as expected, the bridge should be biased as close to the pull-in voltage as possible in order to most effectively convert small voltage fluctuations into mechanical oscillations. This phenomena is graphically illustrated in Figure 15 by a growing slope with increasing DC bias. By fitting a smooth interpolation to the computed data, we can calculate a functional form of the relationship between bias and displacement. When combined with a similar relationship between optical phase shift and displacement, which is simulated in the following section, the complete transduction response can be approximated.

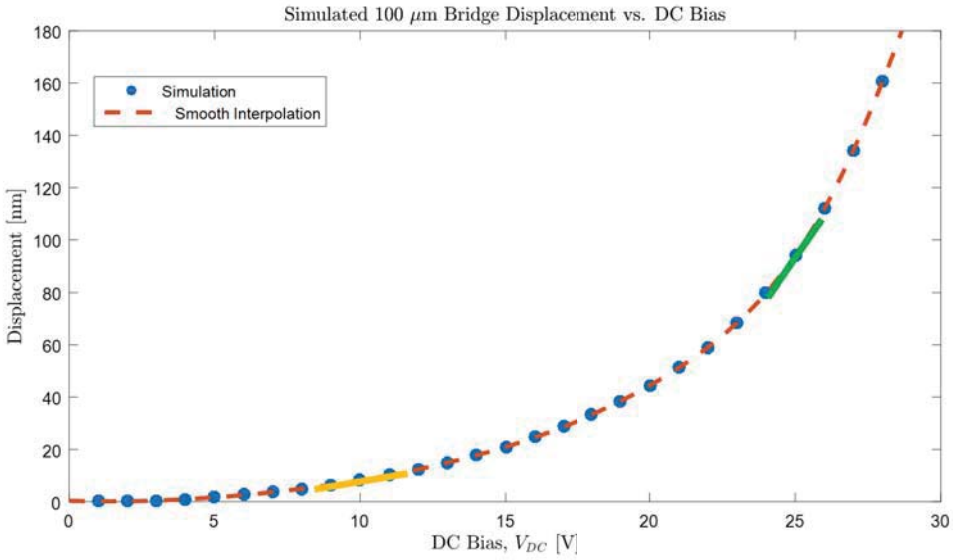

Figure 15: Simulated center-point displacement vs. applied DC bias for a 100 micron long micro-bridge. For optimal electromechanical coupling, the DC bias should be set near the pull-in voltage (approximately 30V here) such that small voltage oscillations about the DC bias will correspond to larger mechanical oscillations. This concept is visually illustrated by the notable increase in the slope from 10V (orange) to 25V (green) DC bias.

7 Optomechanical Simulation

To quantify the optomechanical coupling parameter $G_{om} \equiv \partial n_{\text{eff}}/\partial x$, a series of 2D perturber FEM simulations were conducted using the geometry depicted in Figure 16. The initial parameters, established to model the experimental devices used in [12], are outlined in Table 1. For each geometry tested, the effective index of the fundamental TE mode at 1550 nm was then computed as the microbridge-waveguide gap h_{MEMS} was swept. In an attempt to optimize the effective index tuning performance, the effect of varying several geometric parameters was thoroughly explored. The results of these analysis are listed in Appendix H.

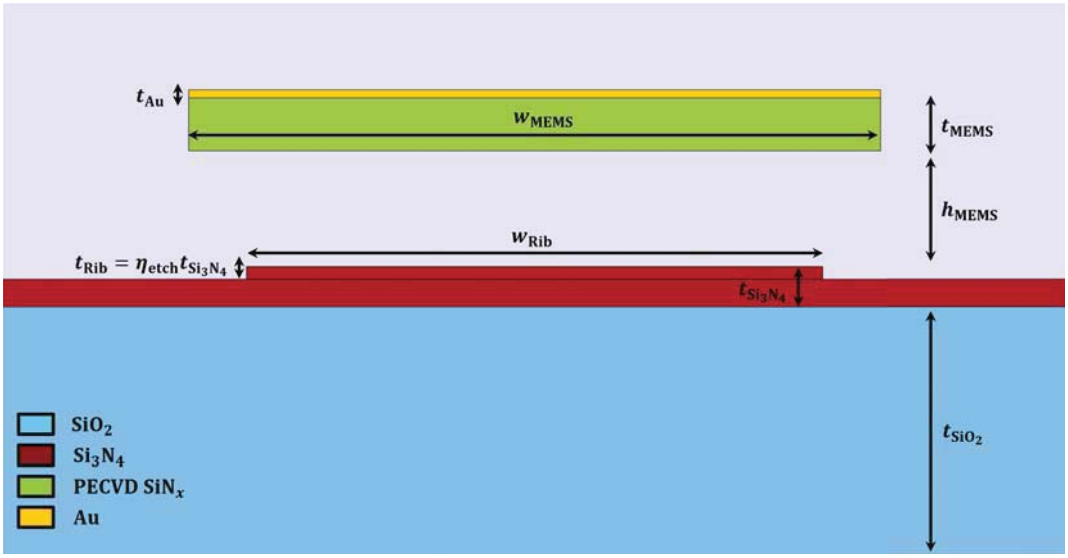

Figure 16: The COMSOL geometry, along with associated dimensions, created for determining the optomechanical coupling strength through simulation of the interaction between the suspended perturber and evanescent field in air.

7.1 2D Perturber Test Results

The simulation results for the default geometry parameters used in the fabricated devices is shown in Figure 17. Since the evanescent field strength of the rib waveguide decays exponentially away from the guide, the effective index tuning likewise decays exponentially as the air gap h_{MEMS} between the waveguide and microbridge increases. The resulting effective index tuning range ($\Delta n_{\text{eff}} > 0.1$) considerably exceeds that of common electro-optic modulators [44].

Since the optical phase shift is proportional to the change in effective index ($\Delta\phi = \frac{2\pi}{\lambda} L_{\text{MEMS}} \Delta n_{\text{eff}}$), the effective index vs. displacement plot effectively quantifies the performance of the second process required for the RF-to-optical transduction scheme – conversion of a microbridge displacement into an optical phase shift. Note that, similar to the displacement versus bias curve discussed in Section 6, the slope of this performance curve increases as the bridge is displaced further into the evanescent field of the underlying waveguide mode. Therefore, in order to obtain optimal index variations in response to a given amplitude of displacement oscillation, the bridge should be displaced as close as feasible to the underlying waveguide.

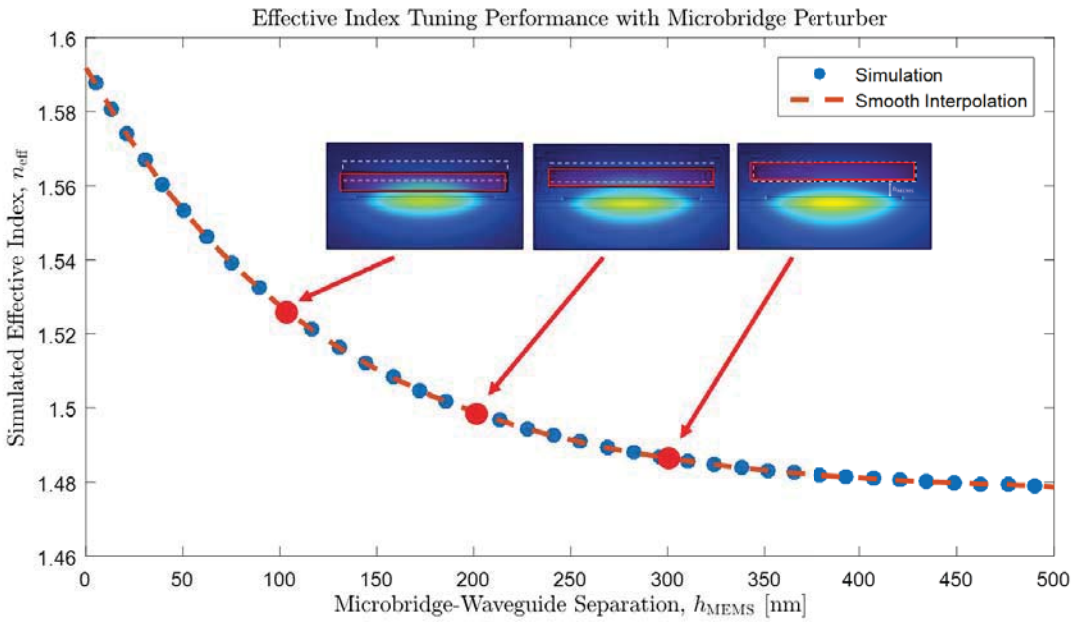

Figure 17: Simulated effective index tuning performance of the microbridge perturber with the dimensions described in Table 1. The mode profile insets depict increasing capture of the optical mode within the microbridge as it is lowered from 300 to 100 nm above the underlying waveguide.

Further details on optomechanical simulation and optimization can be found in Section 7 and Appendix H, respectively.

8 Expected Performance

By combining the computationally derived voltage-to-displacement transfer function from Section 6 with the displacement-to-effective index transfer function (Section 7), the overall transducer response can be estimated.

First, we can approximate the DC response as

$$\Delta\phi = \frac{2\pi}{\lambda} L_{\text{MEMS}} \underbrace{\left[n_{\text{eff}}(h_{\text{MEMS}}|_{V_{DC}}) - n_{\text{eff}}(h_{\text{MEMS}}|_{V_{DC}=0})\right]}_{\text{change in index due to DC displacement}}. \tag{4}$$

At any given DC bias point, the small signal transduction gain – the amplitude of phase oscillations that result divided by the amplitude of the input voltage fluctuation – is represented as

$$\left.\frac{\delta\phi}{\delta V_s}\right|_{V_{DC}} = \text{transducer gain} = \left|T_{\text{bare}}\right|_{V_{DC},\omega\approx 0}. \tag{5}$$

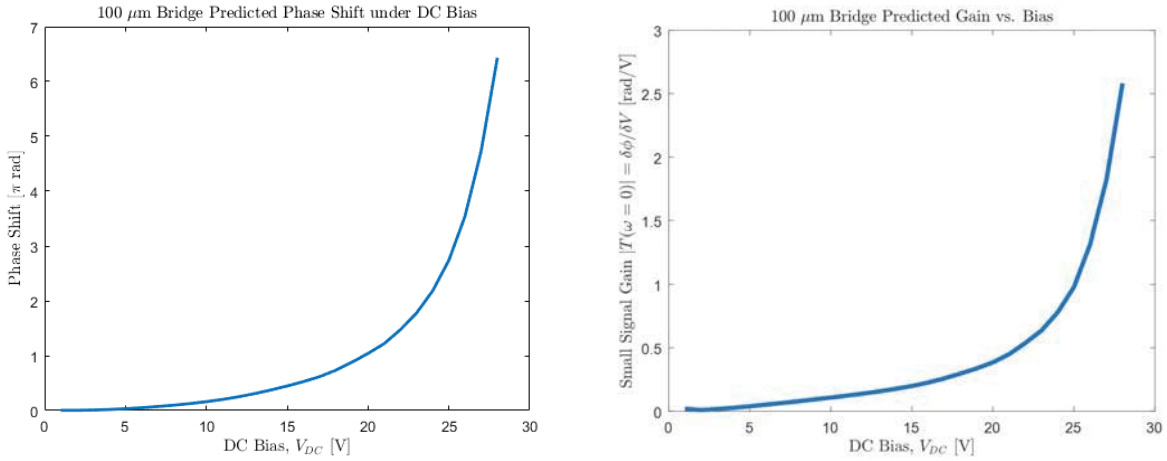

(a) DC Response

(b) Low Frequency Small Signal Response

Figure 18: The predicted DC and low-frequency AC responses of a 100 micron-long microbridge. These responses are found by evaluating the value (DC) or slope (AC) of the electromechanical and optomechanical coupling performance curves and combining the results in accordance with the device transfer function.

These two characteristics are plotted in Figure 18 for the sample 100 micron bridge analyzed in the previous sections. The DC response on the left hand side, which is essentially a combination of the constituent displacement vs. DC bias and effective index vs. displacement plots, demonstrates characteristics similar to these previous plots. Namely, the slope of the curve increases sharply as the pull-in voltage is approached. This results from the combination of: 1) the increased displacement sensitivity to voltage near the pull-in voltage, and 2) the increased coupling between the microbridge and evanescent field when the bridge is displaced closer to the underlying waveguide.

The low frequency RF small signal response, or gain curve, shown in Figure 18b is found by evaluating the *slopes* – versus the *values* used for the aforementioned DC phase shift response curve – of the two constituent performance curves at a set DC bias point. The resulting small signal gain,

$\delta\phi/\delta V_s$ depicts a similar dependence on DC bias as the previous results.

Due to the mechanical properties of the microbridge, which is characterized by the complex susceptibility factor χ_m^0, the small signal gain at RF frequencies cannot be found by simply taking the derivative of Figure 18a. Instead, the device transfer function must be evaluated. Due to the Lorentzian nature of T_{bare}, the response contains a sharp peak near the mechanical resonance frequency Ω_m. The width of this peak is described by the mechanical damping coefficient Γ_m. Figure 19 depicts the small signal frequency response of the transducer for the computed 100 micron bridge fundamental resonant frequency of 2.04 MHz and a quality factor $Q = \Omega_m/\Gamma_m = 100$, a typical value for a microbridge in air [11].[2] This result, as with the previous low frequency response curves, is found by substituting the electromechanical and optomechanical response curves into the device transfer function.

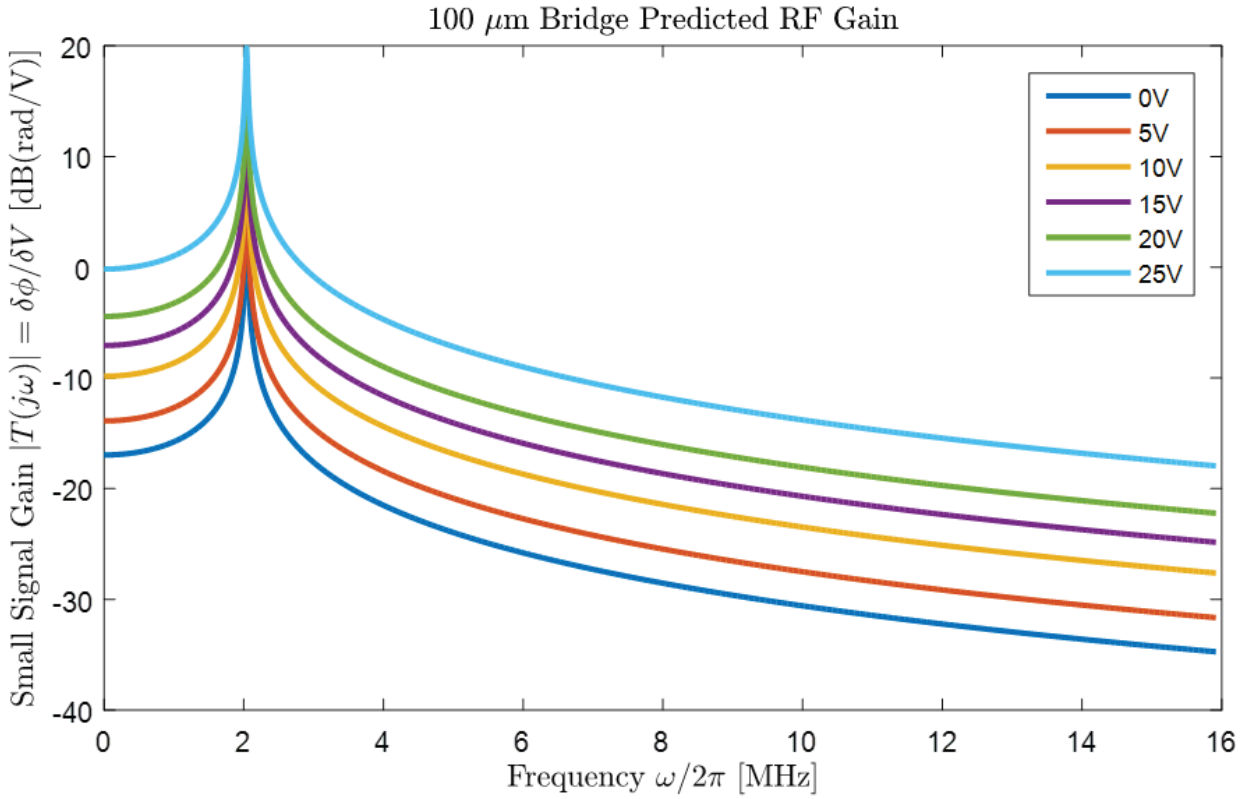

Figure 19: The RF frequency response of the proposed RF-to-optical transducer for several DC bias voltages (shown in different colors). The small signal gain $\delta\phi/\delta V_s$ has a peak at the mechanical resonance frequency of the microbridge, in this case 2.04 MHz. The response is shown on a logarithmic (i.e. decibel or "dB") scale to avoid having the plot of the resonance dominate the response over the rest of the frequency range.

At a DC bias of 25V (close to pull-in), the peak small signal gain is approximately 100 rad/V. The on-resonance half-wave voltage V_π – a common performance metric which conveys the input voltage required to induce an optical phase shift of π – can therefore be calculated as approximately

[2]The quality factor Q is a commonly used metric when analyzing resonant peaks which relates the rate of oscillation to that of the energy dissipation within the resonator.

30 mV, or around two orders of magnitude lower than the same quantity in typical electro-optic and thermo-optic devices [44, 26]. This reduced modulation voltage is one of the key advantages of this technology; however, it should be noted that the performance advantage is only obtained within the narrow bandwidth of the mechanical resonance. As the quality factor Q of the bridge increases, the peak gain also increases, but at the expense of even further narrowing the resonance bandwidth. In other words, the microbridge is characteristic of a very prominent gain-bandwidth trade-off. Nonetheless, the RF characteristics unveiled in this analysis demonstrate the potential performance advantages that can be obtain when only a narrow bandwidth of operation is necessary.

8.1 Summary and Direction

In this section, we presented the results of computational simulations which we conducted and analyzed. These results serve as a baseline estimate of the performance expected from the proposed RF-to-optical transducer. To verify these characteristics and to provide a proof-of-concept implementation of the proposed transduction technique, test photonic integrated circuit chips were subsequently fabricated at the Naval Research Laboratory. In the following section, the fabrication process is briefly outlined before analyzing the experimental work conducted with the fabricated samples.

9 Device Fabrication

In the previously conducted DC analysis of the microbridge phase shifter [12], the MEMS resonators were placed above one arm of an integrated interferometer to enable sensitive detection of the phase shifts introduced by the bridge. This design mirrors the requirements set forth in the RF-to-optical transduction architecture discussed in Section 4. Therefore, this design was modified and used for fabrication of new test devices for RF experimentation. The layout file for a sample transducer is depicted in Figure 20. In this layout, a continuous wave laser is coupled to one of two input waveguides on the LHS of the image. The narrowed region just to the right of the input, within which the two waveguides are in close proximity to one another, is known as a "directional coupler." Similar to the simple waveguide branch shown for the MZI in Figure 6, a directional coupler enables the controllable division of power from one or two input ports into two output ports. For the pursued application, equal 50-50 power splitting between the two output waveguides is desired. Once the input light has been broken into two arms, it propagates to the output direction coupler, where the light is recombined and split between the two output ports. However, before the light reaches the output directional coupler, the light in the bottom waveguide of the MZI encounters the MEMS bridge fabricated within the evanescent field of the waveguide. The interaction between the optical signal's evanescent field and the mechanical microbridge induces a phase shift in that arm, which is then measured by the interferometer's output intensity. The two waveguide arms of the interferometer also have a built-in path length imbalance of 100 microns, which enables the operating point to be tuned by changing the input laser's wavelength. This tuning capability is a result of an *optical* path length imbalance which varies as a function of input wavelength over the fixed *physical* length imbalance ΔL_{MZI} (an analytic treatment of this feature is detailed within the MZI transfer function derivation in Appendix B). The three other bridges illustrated beside the waveguides are test structures that are used for non-optical testing, such as measurement of mechanical displacement under an applied DC bias.

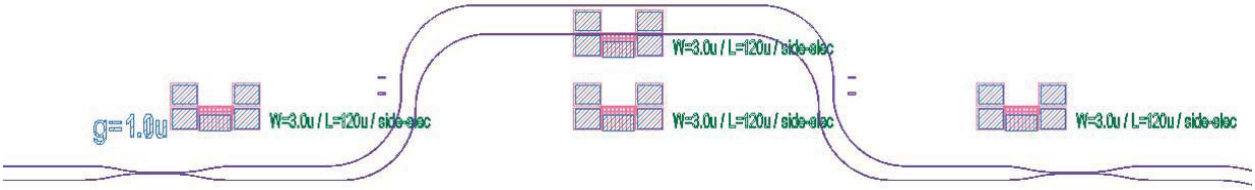

Figure 20: The layout of a single test device contains two waveguides of different lengths coupled together at the input and output by two directional couplers, thus forming an optical interferometer. Within the interferometer, a 120 micron bridge is placed on the bottom waveguide arm.

To obtain multiple test devices, the design shown in Figure 20 is tiled vertically until a complete 12.5 mm $\times$ 5 mm chip is filled. The resulting layout, along with an image of the fabricated chip is shown in Figure 21. The final design is also host to a series of test devices at the bottom of the chip which are used to calibrate the fabrication etch times. At the top of the chip, three ring resonators are included for future exploration of cavity-assisted readout to improve transduction performance.

The original fabrication run for the previous study leveraged electron beam lithography [48] to pattern precision features. In electron beam lithography, an electron beam illuminates regions of a "photoresist" that are to kept in the fabrication process. Areas exposed to the electron beam develop a protective photoresist coating which prevents them from being removed when a subse-

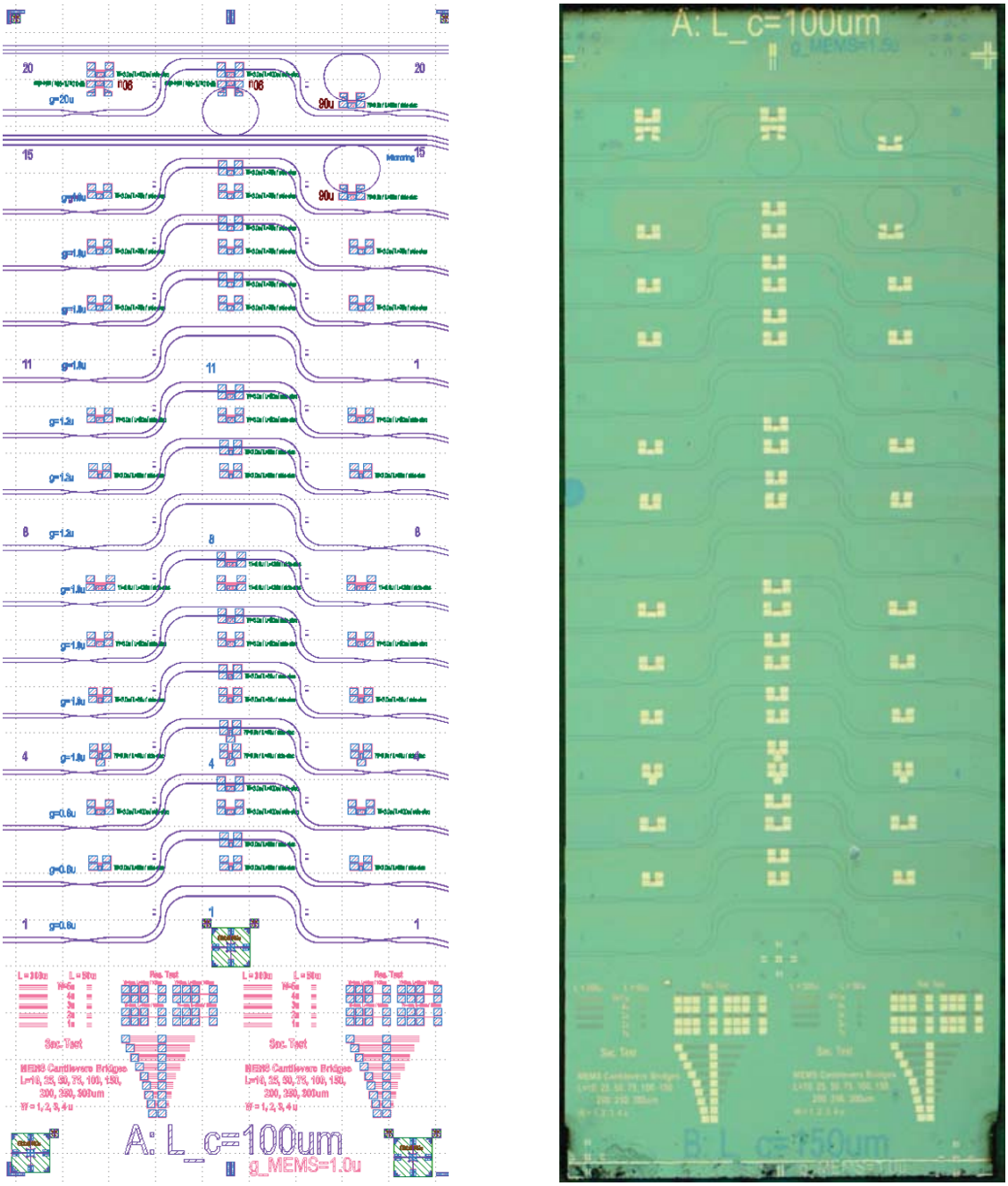

(a) GDS Layout File for PIC Chip

(b) Fabricated PIC Chip

Figure 21: The design file and competed photonic integrated circuit ($\sim 10\times$ magnification).

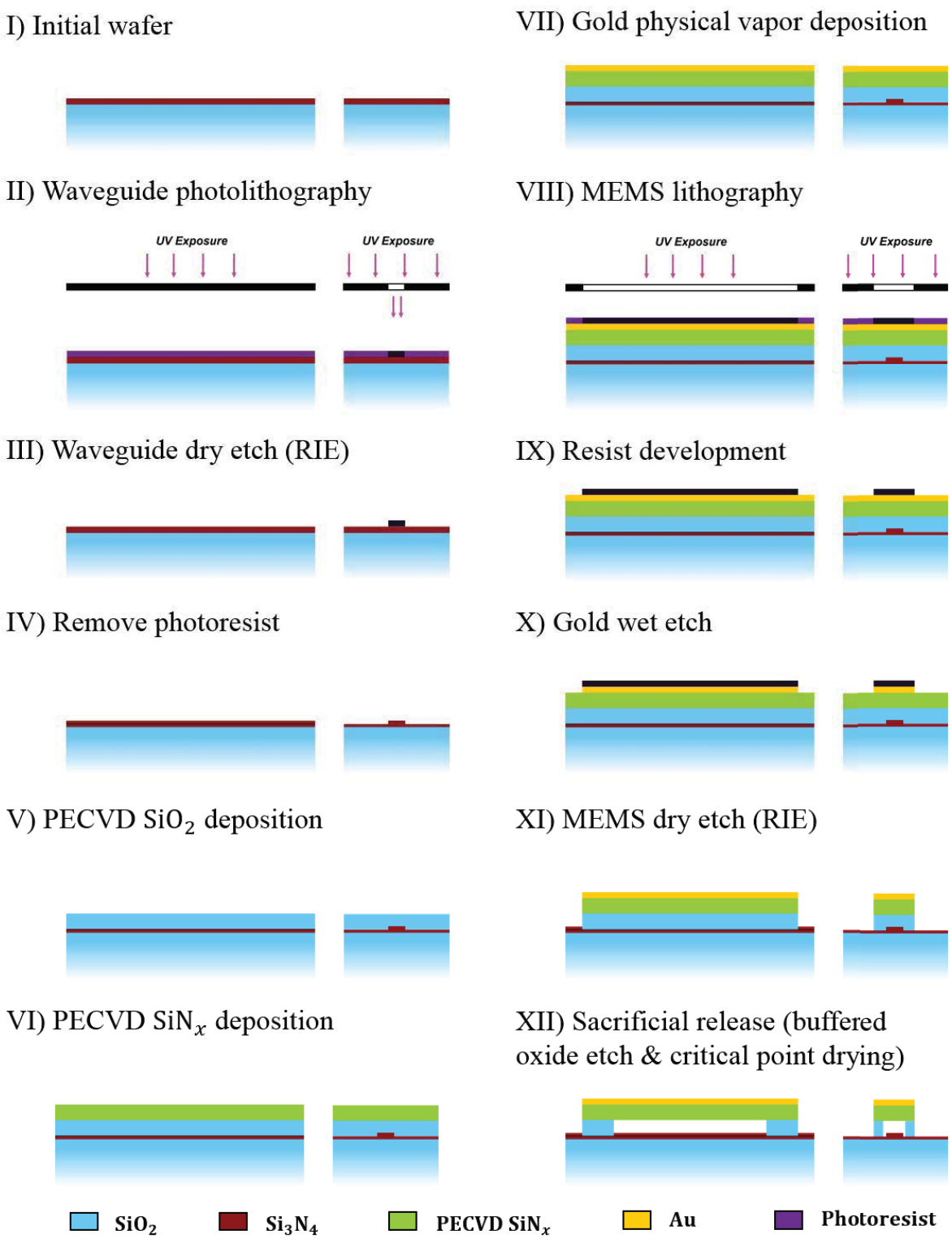

Figure 22: An overview of the steps required for fabrication of on-chip waveguides and MEMS structures (dimensions not to scale). The left side of each image depicts the side profile, while the right side shows a cross sectional view from one end of the MEMS microbridge.

quent etch, or material removal, is conducted. While electron beam lithography affords enhanced resolution for fabricating devices with dimensions smaller than a wavelength of visible light, it is also slower than traditional techniques since the writing, or scanning, of the electron beam across all of the pattern features takes a substantial amount of time. Optical lithography, on the other hand, exposes the entire pattern of a design at once using a high-intensity UV lamp. A glass "photomask" is placed between the source and the photoresist-coated sample to block light from areas that are not to be exposed. Similar to electron-beam lithography, the exposed regions are then considered protected from degradation during future etch steps.

Due to the relative speed of optical lithography, the fabrication process for the samples used in this study was modified to enable its use. This redesign involved the simulation and layout of a new directional coupler with larger feature sizes that could be reliably patterned with optical lithography. The smallest dimension, termed the "critical dimension," of an optical lithography-based design must typically be on the order of 0.5 microns, approximately one wavelength of UV light, or greater. By virtue of the lengthening of the interaction region of the directional coupler – the region within which the two waveguides are in close proximity to one another and are able to exchange energy – the critical dimension of the design was increased from 0.6 microns to 0.8-1.0 microns.

After laying out the PIC chip photomask with the waveguide and MEMS patterns, the fabrication cycle was commenced. Figure 22 outlines the various steps required to complete the sample. Starting with a silicon nitride on insulator (silicon dioxide) wafer, the interferometer waveguides are patterned with an MA-6 contact aligner, an industry standard tool for optical lithography. A reactive ion dry etch was then carried out to etch a rib waveguide into the silicon nitride. After the rib waveguides have been fabricated on the sample, a 250 nm layer of oxide is deposited with an Oxford Instruments plasma enhanced chemical vapor deposition (PECVD) tool. This step is followed by a similar deposition of 250 nm thick PECVD silicon nitride. A thin 35 nm gold layer, which will eventually form the contact on the top of the MEMS bridge is then sputtered onto the top of the silicon nitride layer using electron beam physical vapor deposition. Photoresist is spun onto the surface and subsequently patterned with optical lithography using the MEMS layer portion of the photomask. The gold-SiN_x-oxide stack is then etched away through a series of wet and dry etches, leaving a microbridge-shaped stack of gold and silicon nitride supported on top of oxide. This oxide lying beneath the portion of the bridge to be suspended is known as the sacrificial oxide – it is etched away with a timed buffered oxide etch to leave the silicon nitride microbridge suspended above two oxide anchors (these anchors are preserved during the oxide etch, with is time limited to prevent significant undercut of these supports). To complete the fabrication cycle, the sample is dried in a critical point dryer [49], an instrument which leverages the controlled phase transition of liquid CO_2 to avoid the destructive adhesive forces involved with regular drying that tend to collapse microbridges.

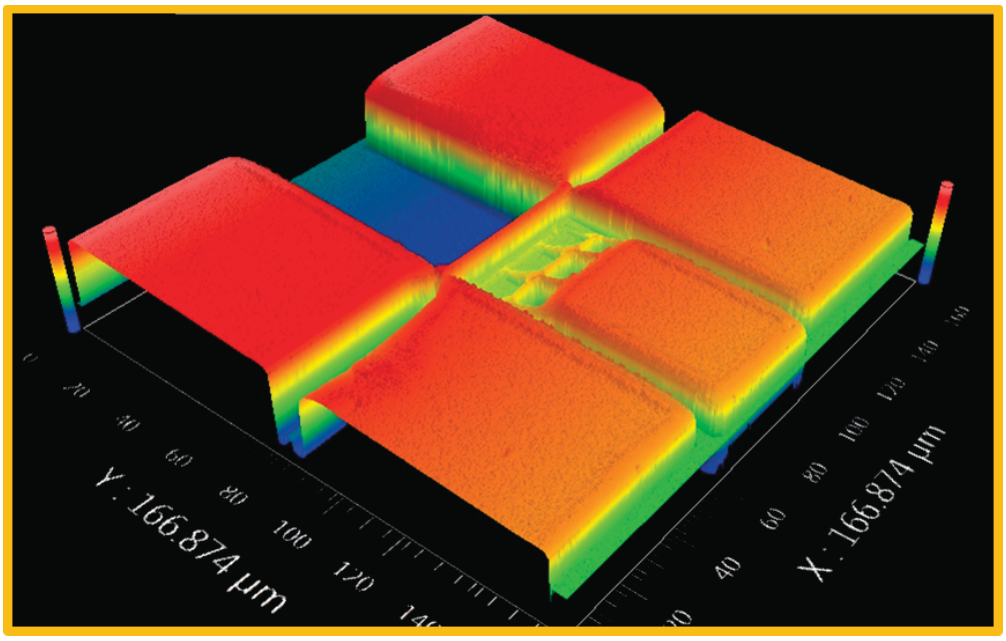

Figure 23: A height profile of a typical microbridge collected with a white light optical profilometer. The color represents the height above the surface (blue). A precise measurement of this structure yields a post height of approximately 500 nm, which is expected after the deposition of 250 nm of oxide and 250 nm of silicon nitride.

Using a Zygo optical profilometer, the height profile of various microbridges was collected. One example, which depicts a taut bridge suspended between four supports, is shown in Figure 23. Two supports on either side of the bridge are required to suspend the microbridge without interfering with the underlying waveguide which runs along the channel parallel to the microbridge.

10 Experimental Design and Methodology

To validate the results of the computational characterization provided in Section 8, the dependence of the fabricated device's response upon input RF signal frequency, RF power, and DC bias voltage was experimentally determined. An experimental apparatus, shown in Figure 24, was first designed and constructed to enable complete parametric control of the transducer. Namely, the setup was designed to allow for variation in the wavelength of light input into the system, the DC bias applied across the microbridge, as well as the frequency and amplitude of the RF input signal.

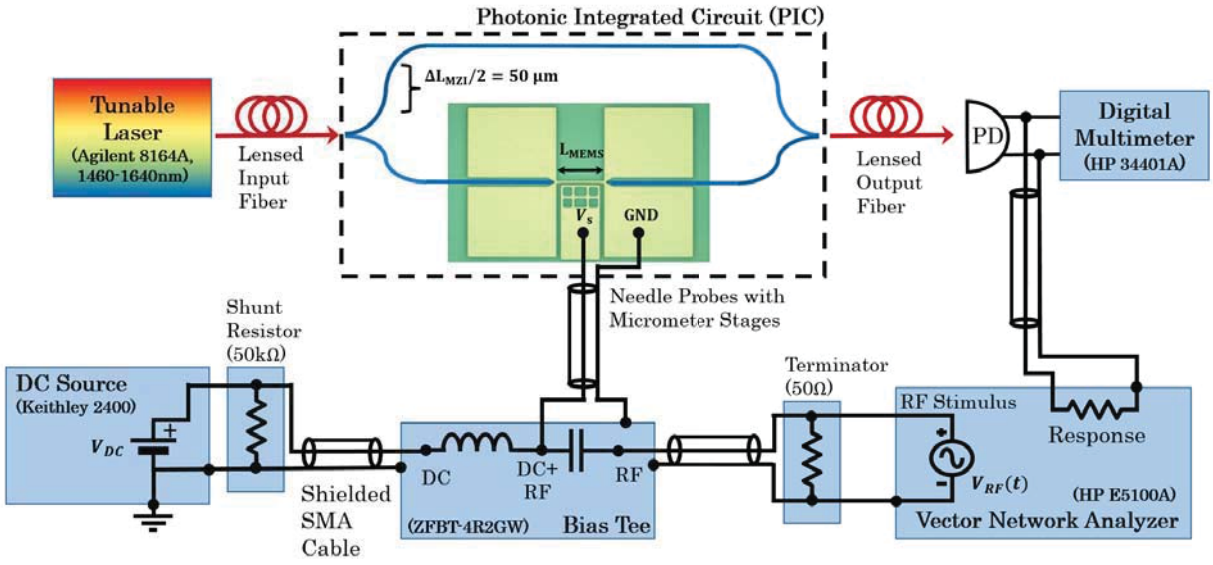

Figure 24: An overview of the experimental apparatus constructed to study the fabricated test devices. The setup features a composite DC+RF voltage which can be placed across the microbridge to drive the system. By connecting the RF output of a vector network analyzer to the microbridge and the interferometer's output photodetector to the network analyzer's input, the system response can be determined as a function of frequency.

The photonic integrated circuit (photograph in Figure 25) was placed on a translation stage for alignment purposes. An input lensed fiber connected to a tunable laser was edge-coupled (Figure 26) to an input port of an on-chip interferometer. A second lensed fiber was connected between the interferometer output and a photodetector which included an in-house developed transimpedance amplifier. The photodetector's frequency response, which is indicative of a detection bandwidth of ∼5 MHz, is shown in Figure 27. Shielded probes on micrometered stages are used to apply the electrical input signal across the microbridge, as depicted in Figure 28.

The probes are connected to a shielded SMA cable which is in turn linked to the output of a bias tee, which combines input DC and RF stimuli onto a common signal. The DC input of the bias tee is driven by a benchtop Keithley 2400 DC power supply. This source is shunted with a 50kΩ terminator for stabilization. The tee's RF input is connected through a 50Ω in-line termination (for proper impedance matching between the source and load) to the RF stimulus from a vector network analyzer. The network analyzer response is provided by the photodetector output, which

is connected in parallel to a benchtop digital multimeter for visualization of the DC photodetector output level.

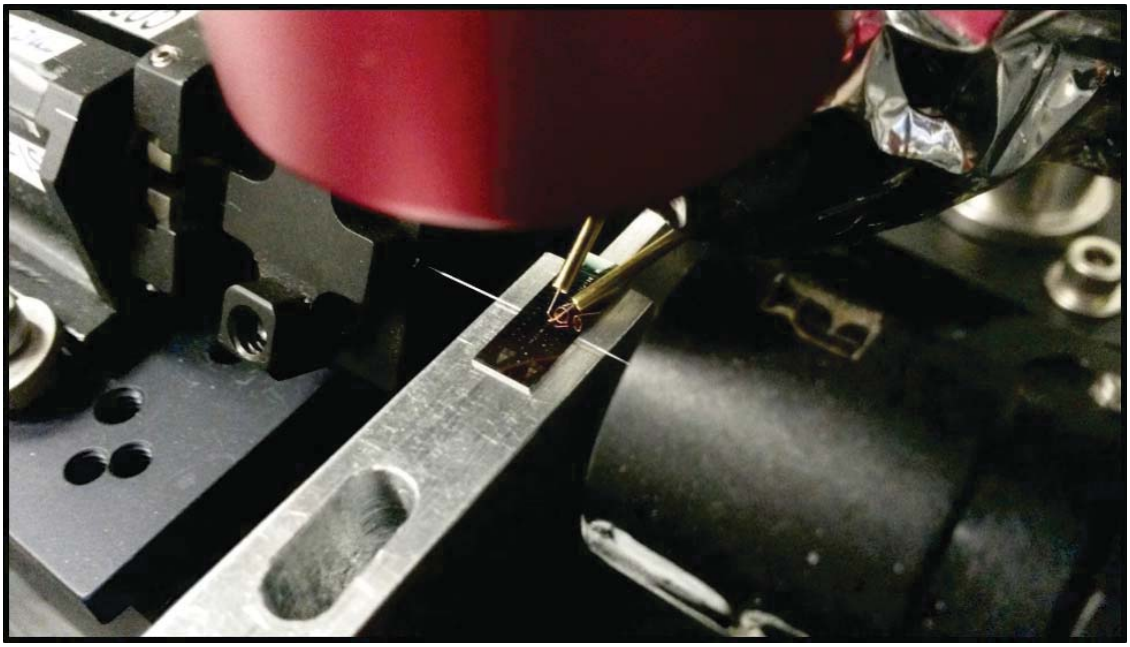

Figure 25: An image of the photonic integrated circuit with input and output lensed fibers coupled to the respective on-chip interferometer ports. Micrometered probes, monitored under a microscope (red objective) connected to a live video feed, are used to connect to the bridge electrodes in order to actuate the devices. The probes are encased in aluminum foil to avoid coupling unwanted ambient noise into the measurement.

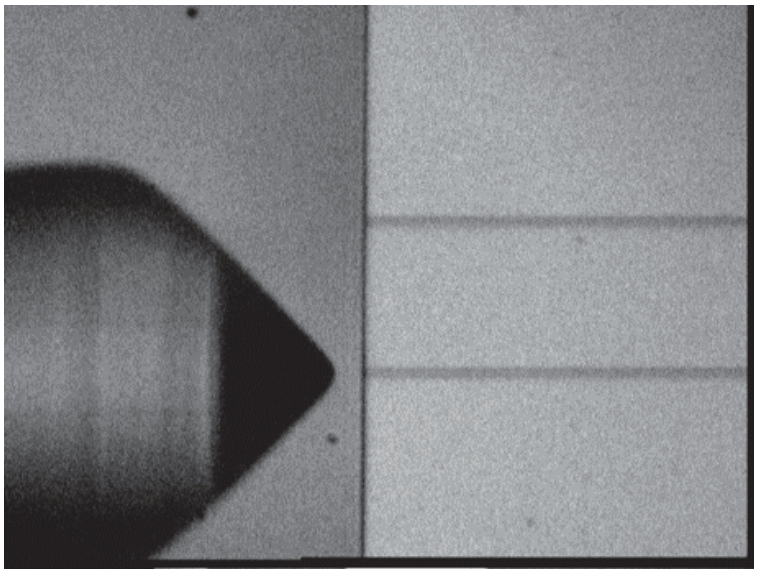

Figure 26: A video-captured image of the lensed fiber coupled to an input port of an on-chip MZI.

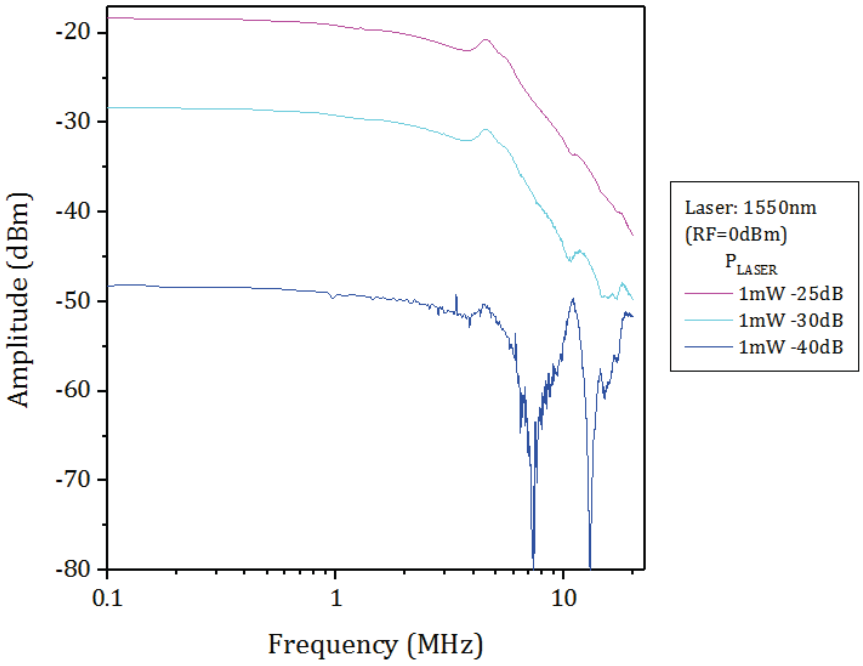

Figure 27: The photodetector frequency response for a 1550 nm laser with varying power. A corner frequency of the transimpedance amplifier is readily apparent at approximately 5 MHz; beyond this frequency, the detector response rapidly drops off at approximately 40 dB/decade, thus indicating the presence of a second-order low-pass filter.

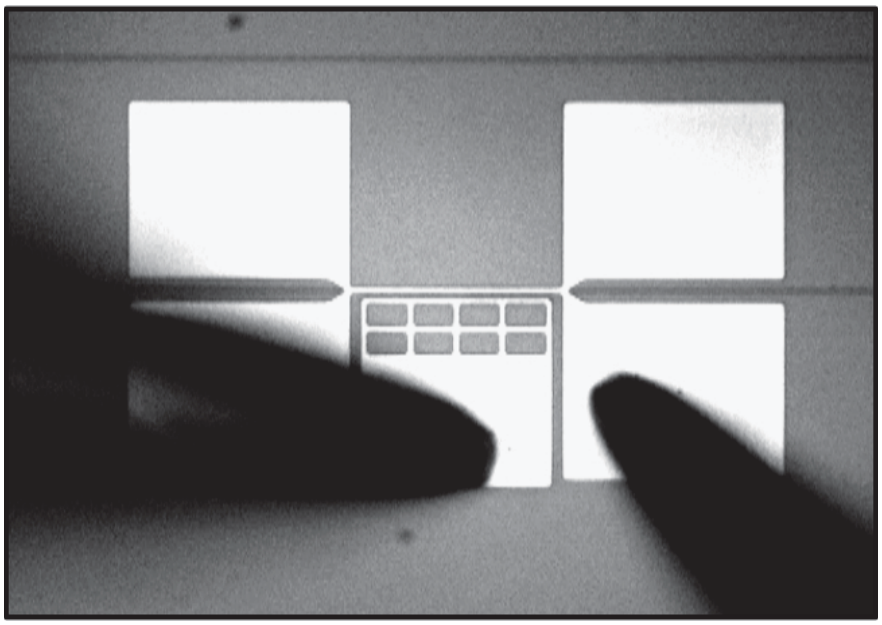

Figure 28: A video-captured image of the probes connected across the actuation electrodes for the microbridge. The RHS probe is connected to ground, while the LHS is the positive voltage source.

11 Experimental Results and Analysis

Before biasing any of the bridges, baseline spectra of each interferometer were taken by varying the input wavelength of the tunable laser source. Given a constant path length imbalance of 100 microns between the two arms, the varying wavelength corresponds to a change in optical phase shift between the arms (see Section 4), thus yielding a sinusoidal, wavelength-dependent output intensity spectrum. Due to the four-port directional couplers at the input and output of each interferometer, there are four possible measurement combinations (explained in Figure 29) from which this spectrum can be collected.

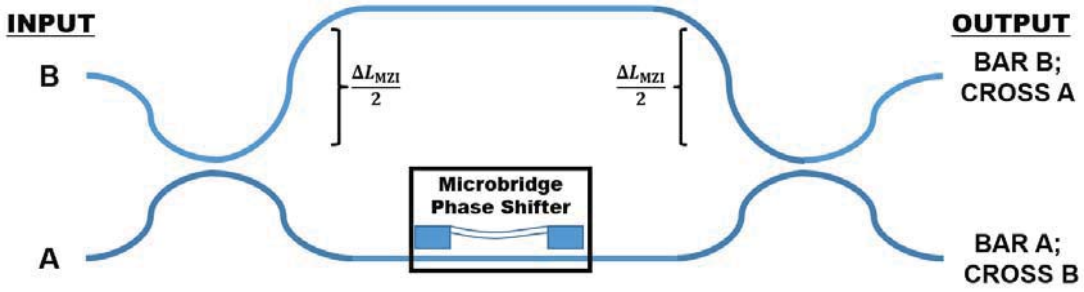

Figure 29: The on-chip Mach-Zehnder interferometers (MZIs) are constructed with two 2×2 directional couplers instead of simple "Y-branches." Therefore, four possible optical spectra can be obtained from the device due to the four combinations of input and output ports. If the output signal is measured from the waveguide that it is launched into, the output port is denoted BAR n, where n is the input port. Otherwise, if the output is taken from the opposite arm than the one which it was launched in, it is noted as the CROSS n. Note that physical pathlength difference between the two arms is ΔL_{MZI}.

Two obtained spectra are shown in Figure 30. Although the two devices have the same interferometer design (neglecting any manufacturing variability), one device is a bare MZI, while the other is an MZI with a 90 micron bridge coupled to one arm of the interferometer. The periodic nature expected from the MZI transfer function (Appendix B) is readily apparent for each, and indicates a period, or free spectral range (FSR), on the order of 10 nm. The extinction ratio, or ratio between maximum and minimum power, achieves a peak value of nearly 25 dB for the CROSS B measurement, indicating ideal power splitting by the input and output directional couplers. As derived in Appendix B, the change in FSR is expected from bridge-induced phase shifts, and can be used to calculate the change in effective index within the region where the bridge is interacting with the optical signal. The simple relations (Appendix B)

$$n_g = \frac{\lambda^2}{\Delta L_{\mathrm{MZI}}(\mathrm{FSR})} \qquad \Delta n_{\mathrm{eff}} = \frac{\Delta L_{\mathrm{MZI}} \Delta n_g}{L_{\mathrm{MEMS}}}, \tag{6}$$

where λ is the laser wavelength in the medium and ΔL_{MEMS} is the intrinsic path length mismatch within the MZI, can be combined to estimate the change in index by the 90 micron bridge to be on the order of 0.05. This value is in agreement with that expected from the simulated effective index vs. displacement curve, and also demonstrates that the microbridge is placed within the optical mode with non-zero optomechanical coupling.

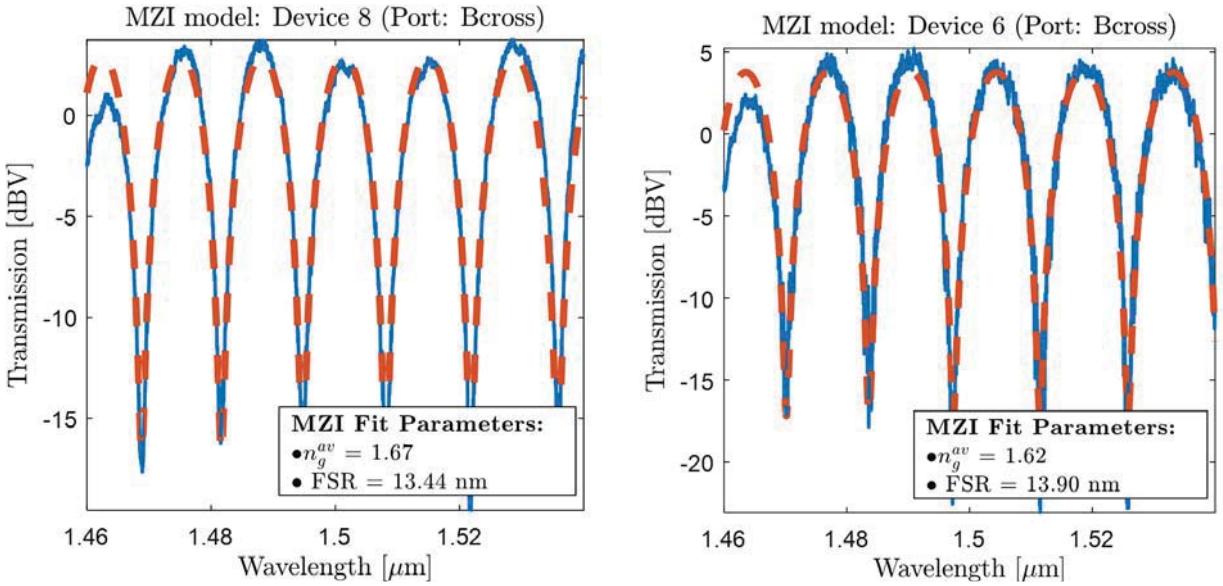

(a) Bare MZI without a coupled microbridge.

(b) MZI with a 90 micron-long microbridge.

Figure 30: MZI spectra for two interferometers, one without any coupled bridge, and the other with an overlying 90 micron-long microbridge on one arm. The change in the group index Δn_g indicates a change in effective index (corresponding to an optical phase shift) produced by the bridge, thus implying interaction between the bridge and optical mode without any electrostatic actuation. The dashed red line indicates a sinusoidal fit, the parameters of which are used to calculate the group index and free spectral range (FSR).

After confirming proper functionality of the interferometers and isolating the system from environmental noise (Appendix J), a DC bias test was conducted in which the wavelength spectrum of the photodetector was collected as the DC input voltage to the interferometer was swept. At each DC bias point, a displacement of the bridge results in an added, yet constant, phase imbalance between the two interferometer arms. As a result, the fringes, or pattern, of the MZI spectrum shifts. The optical phase shift can then be found by comparing the fringe shift (computed with an autocorrelation across several FSRs for accuracy) to the FSR. The phase shift is therefore calculated as

$$\Delta\phi = 2\pi \frac{\text{fringe shift}}{\text{FSR}}. \tag{7}$$

This wavelength shift, depicted in Figure 31 for a 90 micron bridge under DC biases ranging from 0 to 3.5V in 0.1V increments, is typically on the order of nanometers for a ∼10 nm FSR.

The transducer's optical response to a DC voltage placed across the bridge is found by calculating the phase shift at each bias point and plotting it as a function of the applied DC voltage. The result, shown in Figure 32, is in agreement with the amplitude scaled simulation of phase shift vs. DC bias.

Next, the RF transducer response can be found by 1) biasing the bridge to a reasonable deflection, 2) tuning the laser wavelength to a half power point, 3) engaging the vector network analyzer's (VNA's) RF drive at a given power level, and 4) measuring the amplitude of photodetector voltage fluctuations (proportional to phase shifts) across a wide frequency range. The first step ensures that a modest optomechanical interaction between the bridge and optical field is achieved. The

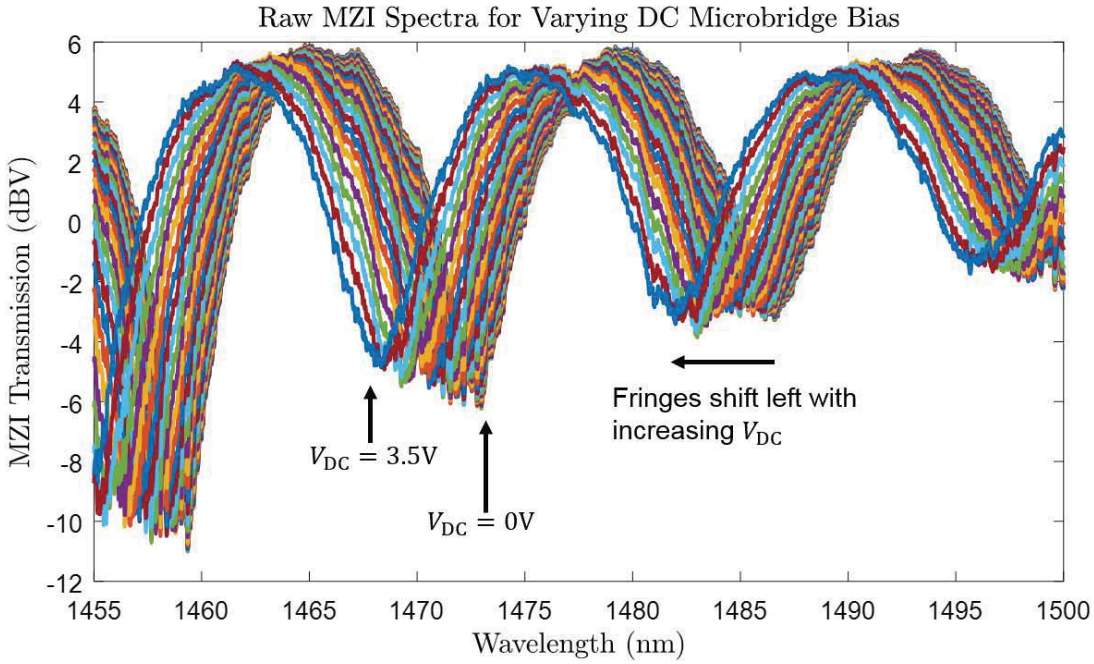

Figure 31: As the DC bias is increased, the fringes shift nonlinearly to the left. The "extinction ratio," or difference between maximum and minimum MZI transmission, decreases as V_{DC} increases due to optical losses caused by interaction between the bridge (and its associated metal electrode) and waveguide mode.

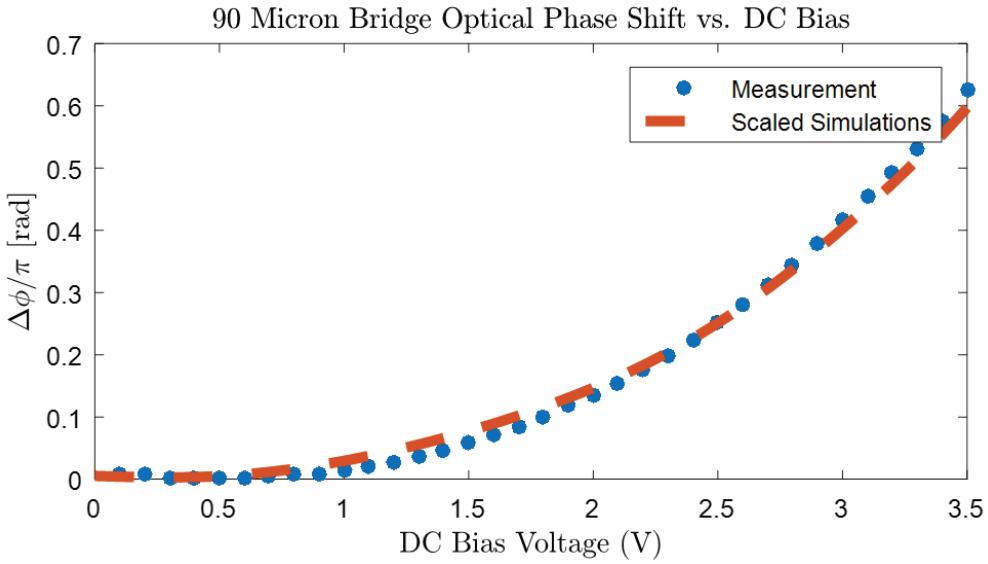

Figure 32: The phase shift of a 90 micron bridge actuated with a variable DC bias. The response characteristic mimics that of the simulation-derived curve, demonstrating qualitative agreement between the results.

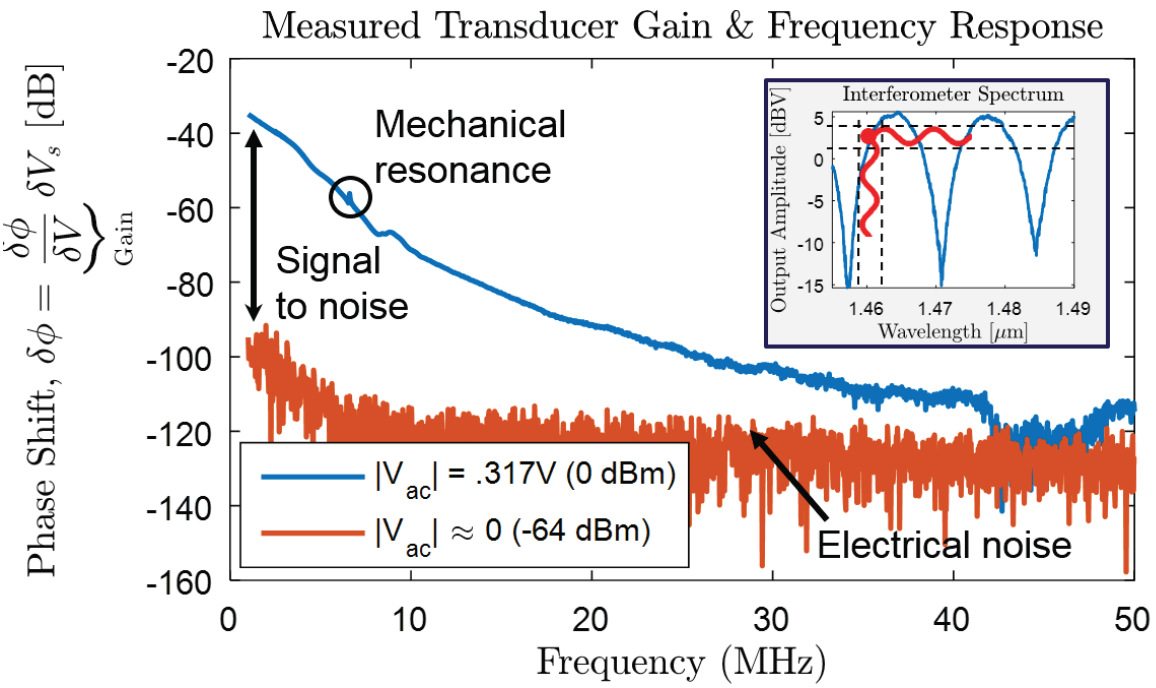

Figure 33: RF response of a 50 micron bridge biased with a 5V DC bias. The blue curve depicts the measured amplitude of phase oscillations induced from a 0.3V amplitude RF signal, whereas the red data depicts the electronic noise data. The inset demonstrates that the system is operating at a -3dB, half-power optical bias point to maximize the output phase shift amplitude.

RF drive then causes the bridge to oscillate, thus inducing phase oscillations which are read out by the MZI. Ensuring condition (2) is met yields the maximum output voltage fluctuation for a given phase oscillation amplitude.

The result is shown in Figure 33. The amplitude of the response is the phase shift; however, this quantity can be converted to the transduction gain, $\delta\phi/\delta V$ by simply dividing by the RF stimulus amplitude δV_{ac}. The response of the 50 micron bridge at low frequency depicts a signal-to-noise ratio of nearly 60 dB, indicating that the output phase shifts are six orders of magnitude greater than those due to electronic noise in the photodetection scheme. The small signal gain curve shown in Figure 33 also illustrates a sharp decrease in transduction efficiency as frequency increased. Past 5 MHz, this falloff can be partially attributed to the photodetector's frequency response; however, other sources of loss may also be present. In the current configuration, frequencies of up $\sim$40 MHz are detectable. Beyond that point, the signal-to-noise ratio drops to less than 1. It should also be noted that the small peak visible at $\sim$ 6.63 MHz appears to be a mechanical resonance peak.

This RF response and gain will always be dependent upon laser wavelength (which establishes the phase shift to photodetector voltage conversion based upon the MZI transfer function), DC bias (which tunes both the electromechanical and optomechanical coupling strength), and RF power (which determines the amplitude of mechanical displacements, and therefore optical phase shifts and output voltage fluctuations generated by the transducer). By always biasing the interferometer at a half power wavelength, the wavelength dependence can be eliminated from the RF gain. However, it is useful to note that the wavelength dependence can be used to confirm that the measured photodetector voltage fluctuations are in fact optically induced. Figures 34 and 35 demonstrate

this phenomenon.

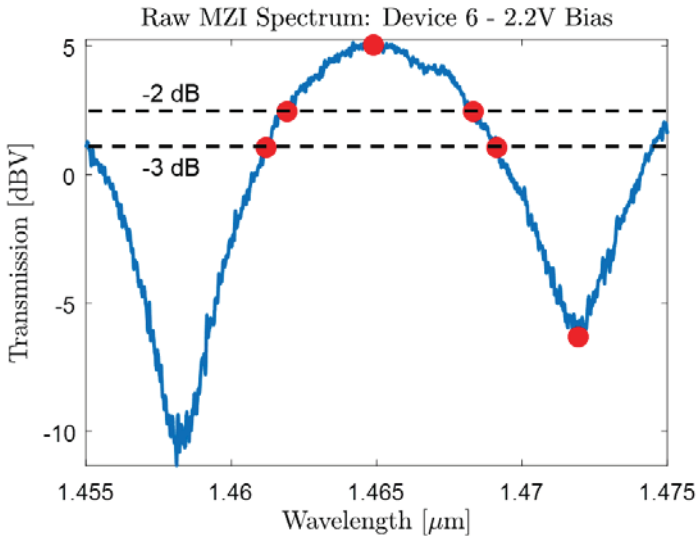

Figure 34: The intensity vs. wavelength spectrum for a sample interferometer with a 90 micron microbridge. The red points depict the bias points to which the laser was tuned to ensure that the output fluctuations were the result of changes in optical phase.

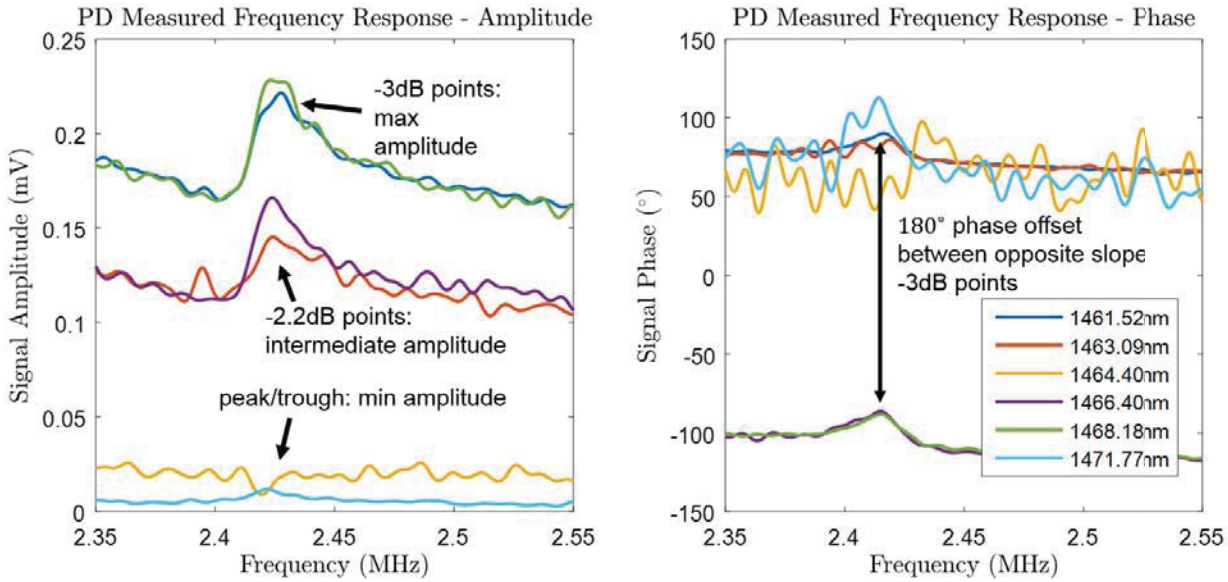

Figure 35: As expected, -3dB bias points have the maximum output amplitude, while peaks and troughs of the intensity vs. wavelength spectrum yield a minimal output. Furthermore, the 180 degree phase difference depicted between bias points on opposite sides of the peak intensity wavelength even further illustrates the connection between input voltage and output optical phase fluctuations.

By tuning the wavelength to different bias points across the interferometer intensity vs. wavelength spectrum, the amplitude of the output voltage fluctuations should be maximized at half-power points and minimized at peaks and troughs. Figure 34 depicts one period of a 90 micron bridge interferometer's spectrum when biased with a 2.2V DC bias. The red points indicate bias points at which the response amplitude and phase were recorded about the mechanical resonant frequency at 6.63 MHz. These responses are shown in Figure 35. As expected, the amplitude of the response is maximized at the two -3dB half-power points, obtains an intermediate value at the -2.2 dB values (due to the non-maximized value of the slope of the intensity vs. wavelength curve at that point), and is minimized to nearly zero at both the peak and trough. Furthermore, the responses on opposite sides of the peak intensity value, where the slopes are negatives of one another, are out of phase by 180 degrees – a direct reflection of this slope reversal. Therefore, the wavelength tuning confirms via both amplitude and phase that the output voltage fluctuations are in fact optically induced.

Even when always biased to a half power point in order to maximize phase shift to output intensity transduction performance, the induced phase shift will always depend on the RF power of the drive tone as well as the DC bias applied across the microbridge. As a final experimental test, the amplitude of phase shifts is mapped as a function of these two variables. The mechanical resonance peak at 6.63 MHz presents itself as an ideal location from which to track this dependence.

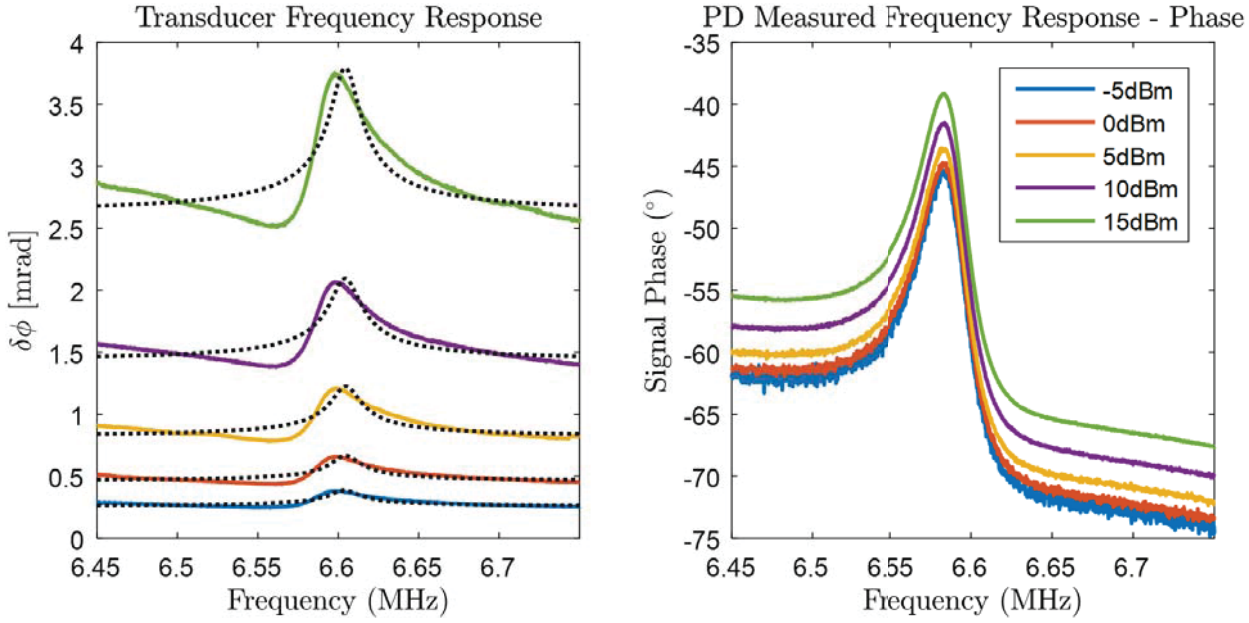

Figure 36: The transduced amplitude and phase for a 50 micron bridge biased at 5.5V and driven at varying RF powers. The black dotted lines represent Lorentzian curves fitted to each resonant peak.

Figure 36 demonstrates how data points were collected for the test. A set DC bias was applied to the bridge, and the RF amplitude was subsequently varied. This process was iterated as the DC bias was slowly incremented. The peak value of each curve was selected and plotted on Figure 37. Figure 37 depicts the expected dependency upon RF drive amplitude and DC bias. Due to the linear first order Taylor expansion of the MZI spectrum at the half-power point, increases in RF

amplitude are directly proportional to growth in the output phase shift. The dependence on V_{DC}, however, is nonlinear as predicted in Section 8. These measurements therefore are in qualitative agreement with the theoretical and computational trends presented in previous sections.

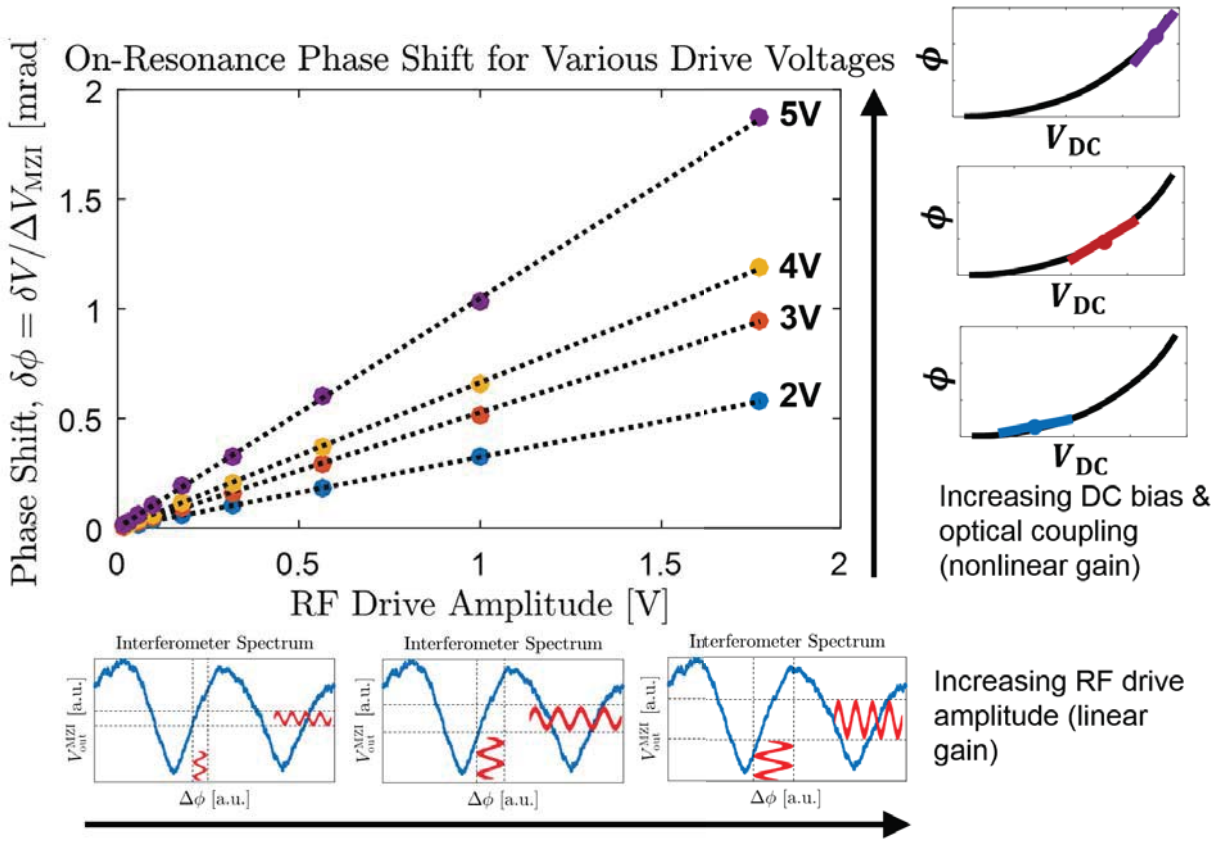

Figure 37: A map of on-resonance phase shifts for a 50 micron bridge biased with different DC voltages and RF signal amplitudes. As expected, the increase in RF drive amplitude produces a linear increase in output phase shift. The output phase shift, however, has a nonlinear relation to V_{DC}, as changing V_{DC} affects both the electromechanical and optomechanical coupling strengths.

12 Discussion and Future Work

While the majority of the experimental data trends, including the phase shift vs. DC bias, the effect of varying the interferometer's optical bias point, and the effect of increasing the amplitude of RF signal applied across the bridge, are in direct correspondence with the theoretical and computational predictions, some rifts still remain. Notably, the narrow, large-amplitude resonant peaks characteristic of the Lorentz functions simulated in Figure 19 are absent from the experimentally determined RF device response. A rapid gain drop-off for frequencies lower than that of the studied resonant peak is also depicted in Figure 33, while the amplitude of the theoretical transfer function is constant for frequencies lower than the resonant frequency. This performance decay at high frequencies can be partially attributed to the narrow bandwidth of the photodetector; however, considering the loss is evident well before the photodetector corner frequency, other loss mechanisms must be present in addition. In the future, a complete analysis of electrical, mechanical, and optical noise sources would contribute to a more accurate estimate of the expected device sensitivity.

To investigate these discrepancies and to further explore the experimental limits of the transducer's performance, future testing could be conducted with the photonic integrated circuit placed within a vacuum chamber. Doing so would minimize the effects of viscous damping, thereby increasing the quality factor of the mechanical microbridge [10]. This increase in Q may make the mechanical resonant peaks more readily visible in the RF response spectrum. Furthermore, the reduced bridge damping may also enable bridge displacements from thermal energy alone – in absence of any external electronic stimulus – to be detected. If so, this spectrum would enable a critical calibration of the optomechanical transduction's displacement sensitivity [50].

Once in vacuum, the microbridges can also be capacitively coupled to an external high-Q LC circuit to not only improve the electromechanical coupling performance, but to study the rich dynamics of strongly coupled electronic and mechanical oscillators [4].

Both of these extensions would aid in further connecting the theoretical work presented within this study to the device's experimental behavior – all while affording new environments within which the proposed electro-opto-mechanical RF-to-optical transduction technique could be evaluated.

13 Conclusions

This report details an extensive study of a novel, fully integrated method for RF-to-optical transduction in which a mechanical microbridge resonator placed within an integrated photonic circuit couples electronic and optical signals. After deriving a theoretical transfer function to characterize the transduction architecture, computational simulations were created to determine the efficiency of each step of the electro-opto-mechanical transduction process. To test the predictive reliability of our modeling and simulation results, we fabricated test devices at the Naval Research Laboratory and conducted a series of characterization tests to compare actual performance to our theoretical predictions. These tests validated the mechanical, optomechanical, and electromechanical functional blocks of our model and confirmed our understanding of the device behavior.

While the experimental portion of this research focused on investigating the first revision of the transducer, the potential for future optimization and improvement of the system was also presented. The design space of the transducer, including coupling techniques, physical parameters, and device geometries, was characterized, yielding optimum coupling conditions that bound the device's peak performance. Feasible experimental directions, such as the incorporation of a coupled electrical oscillator to improve electromechanical coupling, the variation of waveguide parameters to maximize optomechanical coupling, and the encapsulation of the microbridge in vacuum to reduce damping, were not only proposed, but also evaluated to estimate their effect on overall system performance.

The proposed technique is host to unique properties which may be advantageous to future applications. Notably, the transduction architecture enables complete integration into a single design which can be fabricated with common microelectronic techniques. The electrostatic actuation involved also enables low-power conversion of radio frequency signals. If actuated at a mechanical resonance frequency, our modeling demonstrates that the resulting transduction gain can drastically exceed that of common electro-optic and thermo-optic transducers. This enhanced performance, however, is only obtained within the narrow mechanical resonance bandwidth and at the low resonant frequencies of the bridge, which are on the order of 1-10 MHz. Depending upon the particular application, the drawbacks may be acceptable or even inconsequential when compared to the advantages. Thus, the results of this comprehensive study not only validate the potential for future development of the technology, but also add to the growing body of knowledge regarding electro-opto-mechanical transduction techniques.

In general, the use of mechanical structures to efficiently mediate conversion between radio frequency and optical signals has recently ignited widespread research interest due to the potential use of such transducers to solve a diverse set of technical challenges in fields ranging from sensing to quantum information science. An ideal transducer, for example, would enable the long-distance, low-noise detection and transmission of weak radio frequency signals – signals which would have been lost or hidden below thermal noise in traditional electronic systems. Before the complete realm of possible applications can be envisioned, however, the enabling technologies of such transducers must be fully explored and characterized. This research marks one step towards that end.

References

[1] Taylor, J. M., Sørensen, A. S., Marcus, C. M. & Polzik, E. S., Laser cooling and optical detection of excitations in a LC electrical circuit. *Physical Review Letters* **107**, 273601 (2011).

[2] Pruessner, M. W., et. al., An Opto-Electro-Mechanical Phase Shifter. *Proceedings from the 2015 CLEO Conference*.

[3] Aspelmeyer, M., Kippenberg, T.J. & Marquardt, F., Cavity optomechanics. *Reviews of Modern Physics* **86**, 1392-1452 (2014).

[4] Bagci, T., et. al., Optical detection of radio waves through a nanomechanical transducer. *Nature* **507**, 81-85 (2014).

[5] Bochmann, J., Vainsencher, A., Awschalom, D. D. & Cleland, A. N., Nanomechanical coupling between microwave and optical photons. *Nat. Phys.* **9**, 712-716 (2013).

[6] Andrews, R. W. et al., Bidirectional and efficient conversion between microwave and optical light. *Nat. Phys.* **10**, 321-326 (2014).

[7] Kraus, J.D., *Radio Astronomy* (McGraw, 1966).

[8] DARPA Optical Radiation Cooling and Heating in Integrated Devices (ORCHID) Program. `http://www.darpa.mil/program/optical-radiation-cooling-and-heating-in-integrated-devices`.

[9] DARPA Quantum-Assisted Sensing and Readout (QuASAR) Program. `http://www.darpa.mil/program/quantum-assisted-sensing-and-readout`.

[10] Cleland, A.N., *Foundations of Nanomechanics: from solid state theory to device applications*. Springer, Berlin (2010).

[11] Pruessner, M. W., et. al., An Optomechanical Transducer Platform for Evanescent Field Displacement Sensing. *IEEE Sensors Journal* **14**, 3473-3481 (2014).

[12] Pruessner, M., et. al., Broadband opto-electro-mechanical effective refractive index tuning on a chip. *Optics Express* **24** 13917-13930 (2016).

[13] Chrostowski, L. & Hochberg, M., *Silicon Photonics Design* (Cabridge University Press, 2015).

[14] Aspelmeyer, M., Kippenberg, T.J., & Marquardt, F., Cavity optomechanics. *Rev. Mod. Phys.* **86**, (2014).

[15] Garrido Alzar, C. L., Martinez, M. A. G. & Nussenzveig, P., Classical analog of electromagnetically induced transparency. *Am. J. Phys.* **70**, 37-41 (2002).

[16] Novotny, L., Strong coupling, energy splitting, and level crossings: A classical perspective. *Am. J. Phys.* **78**, 1199-1202 (2010).

[17] Palais, J. C., *Fiber Optic Communications 4th ed.*. Pearson Prentice Hall, New Jersey (2005).

[18] MIT 6.777J Material Property Database – PECVD Silicon Nitride. `www.mit.edu/~6.777/matprops/pecvd_sin.htm`.

[19] Lehnert, K.W. in *Cavity Optomechanics* (Aspelmeyer, M., Kippenberg, T.J., & Marquardt, F. ed.), 233-252 (Springer, 2014).

[20] Regal, C. A. & Lehnert, K. W., From cavity electromechanics to cavity optomechanics. *J. Phys. Conf. Ser* **264**, (2011).

[21] COMSOL Multiphysics, `www.comsol.com`.

[22] Unterreithmeier, Quirin P., Weig, Eva M., Kotthaus, J. P., Universal transduction scheme for nanomechanical systems based on dielectric forces. *Nature* **458**, 1001-1004 (2009).

[23] Schmid, S., Hierold, C. & Boisen, A., Modeling the Kelvin polarization force actuation of micro and nanomechanical systems. *J. Appl. Phys.* **107**, (2010).

[24] Southworth, D. R. et al., Stress and silicon nitride: A crack in the universal dissipation of glasses. *Phys. Rev. Lett.* (2009).

[25] Zhang, W., et. al., Electrostatic pull-in instability in MEMS/NEMS: A review. *Sensors and Actuators* **214**, (2014).

[26] Harris, N.C., et. al., Efficient, compact and low loss thermo-optic phase shifter in silicon. *Optics Express* **22**, (2014).

[27] Bogaerts, W., et. al., Silicon microring resonators, *Laser Photonics Rev.* **6**, (2012).

[28] Li, G., et. al., 25Gb/s 1V-driving CMOS ring modulator with integrated thermal tuning. *Optics Express* **19**, 20435-20443(2011).

[29] Teufel, J. D. et al., Circuit cavity electromechanics in the strong-coupling regime. *Nature* **471**, 204-208 (2011).

[30] Bagci, T., Opto-Electromechanical Devices for Low-Noise Detection of Radio Waves. *University of Copenhagen PhD Thesis*, (2014)

[31] Zalevsky, Z., Integrated micro- and nanophotonic dynamic devices: a review. *Journal of Nanophotonics* **1**, 012504-012504-24 (2007).

[32] Kippenberg, T.J. & Vahala, K. J., Cavity optomechanics: back-action at the mesoscale. *Science* **321**, 1172-1176 (2008).

[33] Regal, C. A. & Lehnert, K. W., From cavity electromechanics to cavity optomechanics. *J. Phys. Conf. Ser.* **264**, 012025-012025-8 (2011).

[34] Safavi-Naeini, A. H. & Painter, O., Proposal for an optomechanical traveling wave phonon-photon translator. *New J. Phys.* **13**, 013017-013017-30 (2011).

[35] Bochmann, J., Vainsencher, A., Awschalom, D. D. & Cleland, A. N., Nanomechanical coupling between microwave and optical photons. *Nature Phys.* **9**, 712-716 (2013).

[36] Devgan, P. S., Pruessner, M. W., Urick, V. J. & Williams, K. J., Detecting low-power and RF signals and using a multimode optoelectronic and oscillator and integrated optical filter. *IEEE Photonics Technol. Lett.* **22**, 152-154 (2010).

[37] Ilchenko, V. S. et al., Ka-band all-resonant photonic microwave receiver. *IEEE Photonics Technol. Lett.* **20**, 1600-1612 (2008).

[38] Kolpekwar, A., Blanton, R.D., & Woodilla, D., Failure Modes for Stiction in Surface-Micromachined MEMS. *1998 IEEE International Test Conference Proceedings*, 551-556.

[39] Mastrangelo, C.H., Adhesion-Related Failure Mechanisms in Micomechanical Devices. *Tribology Letters* **3**, 223-238 (1997).

[40] Savkar, A.A, et. al., On the Use of Structural Vibrations to Release Stiction Failed MEMS. *Journal of Microelectromechanical Systems* **16**, 163-173 (2007).

[41] Gupta, V., et. al., Recovery of Stiction-Failed MEMS Structures Using Laser-Induced Stress Waves. *Journal of Microelectromechanical Systems* **13**, 696-700 (2004).

[42] Leseman, Z.C., Koppaka, S., & Mackin, T.J., A Fracture Mechanics Description of Stress Wave Repair in Stiction-Failed Microcantilevers: Theory and Experiments. *Journal of Microelectromechanical Systems* **16**, 904-911 (2007).

[43] Stievater, T.H., et. al., Suspended photonic waveguide devices. *Applied Optics* **54**, 164-173 (2015).

[44] Lipson, M., Compact Electro-Optic Modulators on a Silicon Chip. *IEEE Journal of Selected Topics in Quantum Electronics* **12**, 1520-1526 (2006).

[45] Quigley, G.R., Harris, R.D., Wilkinson, J.S., Sensitivity enhancement of integrated optical sensors by use of thin high-index films. *Applied Optics* **38**, 6036-6039 (1999).

[46] Hahn, J., et. al. Measurement of the enhanced evanescent fields of integrated waveguides for optical near-field sensing. *Applied Optics* **47**, 2357-2360 (2008).

[47] Najafi, K., & Suzuki, K. A Novel Technique and Structure for the Measurement of Instrinsic Stress and Young's Modulus of Thin Films. *IEEE Micro Electro Mechanical Systems Proceedings, An Investigation of Micro Structures, Sensors, Actuators, Machines and Robots*, 96-97 (1989).

[48] Tseng, A.A., et. al. Electron Beam Lithography in Nanoscale Fabrication: Recent Development. *IEEE Transactions on Electronics Packing Manufacturing* **26**, 141-149 (2003).

[49] Jafri, I.H., Busta, H., Walsh, S.T. Critical point drying and cleaning for MEMS technology. *SPIE MEMS Reliability for Critical and Space Applications* **3880**, 51-58. (1999).

[50] Li, M., et. al. Harnessing optical forces in integrated photonic circuits. *Nature* **456**, 480-485 (2008).

[51] Kozinsky, I., Postma, H.W. Ch., Bargatin, I., & Roukes, M.L., Tuning nonlinearity, dynamic range, and frequency of nanomechanical resonators. *Applied Physics Letters* **88**, 253101 (2006).

Appendix A Transfer Function Derivations

A.1 Method 1: Bare Transducer

A.1.1 Equations of Motion

Assuming the microbridge in Figure 7 to be a point mass located at the resonator's center-of-mass, the system's Lagrangian can be expressed as

$$\mathcal{L} = T - U = \frac{1}{2}m\dot{x}^2 - \left[\frac{1}{2}m\Omega_m^2 x^2 + \frac{q^2}{2C(x)}\right], \tag{8}$$

where x is the displacement from the unbiased equilibrium, m is the effective mass of the microbridge (which is equal to the physical mass if x is center-of-mass displacement [14]), Ω_m is the microbridge's fundamental resonant frequency, q is the charge on the side electrode resulting from an applied voltage $V_s(t)$, and $C(x)$ is the parametric capacitance between the two electrodes. Applying the Euler-Lagrange equation $\frac{\partial \mathcal{L}}{\partial x} = \frac{d}{dt}(\frac{\partial \mathcal{L}}{\partial \dot{x}})$, we find the following equation of motion:

$$\frac{d^2x}{dt^2} + \Gamma_m\frac{dx}{dt} + \Omega_m^2 x - \frac{V_s(t)^2}{2m}\frac{\partial C(x)}{\partial x} - \frac{F_{\text{ext}}}{m} = 0, \tag{9}$$

where damping and external forces, $m\Gamma_m\dot{x}$ and F_{ext} respectively, have been added. Γ_m represents the mechanical decay rate.

Assuming that the applied voltage $V_s(t) = V_{\text{dc}} + \delta V_s(t)$ consists of a DC bias V_{dc} as well as the small reference signal to be modulated, $\delta V_s(t)$, we can approximate Equation 9 to first order in $\delta V_s(t)$, yielding

$$\frac{d^2x}{dt^2} + \Gamma_m\frac{dx}{dt} + \Omega_m^2 x - \frac{1}{2m}\frac{\partial C(x)}{\partial x}(V_{\text{dc}}^2 + 2V_{\text{dc}}\delta V_s(t) + \cancelto{0}{\delta V_s(t)^2}) - \frac{F_{\text{ext}}}{m} = 0. \tag{10}$$

This first order approximation is valid for the experiments conducted in Section 11 in which the RF drive amplitudes were typically less than ∼10% of the DC bias voltage. Ignoring the contribution of the external force (which can be considered a Langevin noise force δF_{ext}), the DC bias leads to a new static-equilibrium position and charge,

$$x_0 = \frac{V_{\text{dc}}^2}{2m\Omega_m^2}\frac{\partial C(x)}{\partial x}\bigg|_{x=x_0} \qquad\qquad q_0 = C(x_0)V_{\text{dc}}. \tag{11}$$

The electrostatic force between the two electrodes not only affects the static equilibrium, but also reduces the microbridge oscillator's resonant frequency through the capacitive force $F_c = -\partial U_C/\partial x$. Expanded to first order about x_0,

$$F_c(x_0 + \delta x) \approx F_c(x_0) + \frac{dF_c}{dx}\bigg|_{x=x_0}\delta x = F_c(x_0) - \frac{1}{2}\left(\frac{q_0}{C(x_0)}\right)^2\frac{\partial^2 C(x)}{dx^2}\bigg|_{x=x_0}\delta x.$$

The first term of the expansion results in the new equilibrium position; however, the second term represents an additional spring with spring constant [22]

$$k_1 = \frac{\partial F_c}{\partial x}\bigg|_{x=x_0} = -\frac{1}{2}\underbrace{\left(\frac{q_0}{C(x_0)}\right)^2}_{V_{\text{dc}}^2}\frac{\partial^2 C(x)}{dx^2}\bigg|_{x=x_0}.$$

The total effective spring constant for the parallel springs is thus $k = k_0 + k_1 = m\widetilde{\Omega}_m^2$, where $k_0 = m\Omega_m^2$ and $\widetilde{\Omega}_m$ represents the capacitively-softened [51] resonant frequency. The resulting reduced mechanical resonance frequency is

$$\widetilde{\Omega}_m = \sqrt{\frac{k_0}{m} - \frac{1}{2m}\left(\frac{q_0}{C(x_0)}\right)^2 \frac{\partial^2 C(x)}{dx^2}\bigg|_{x=x_0}} \approx \Omega_m \left(1 - \frac{1}{4k_0}\left(\frac{q_0}{C(x_0)}\right)^2 \frac{\partial^2 C(x)}{\partial x^2}\bigg|_{x=x_0}\right), \tag{12}$$

thus representing a change in frequency of

$$\Delta\Omega_m = \widetilde{\Omega}_m - \Omega_m = -\frac{\Omega_m}{4k_0}\left(\frac{q_0}{C(x_0)}\right)^2 \frac{\partial^2 C(x)}{\partial x^2}\bigg|_{x=x_0} = -\frac{V_{\rm dc}^2}{4m\Omega_m}\frac{\partial^2 C(x)}{\partial x^2}\bigg|_{x=x_0}. \tag{13}$$

This frequency shift is immediately realized upon linearizing the system's equation of motion about the equilibrium position. From Equation 10, the response to first order perturbations can be written as

$$\frac{d^2\delta x}{dt^2} + \Gamma_m \frac{d\delta x}{dt} + \left(\Omega_m^2 \underbrace{- \frac{V_{\rm dc}^2}{2m}\frac{\partial^2 C(x)}{\partial^2 x}\bigg|_{x=x_0}}_{2\Omega_m \Delta\Omega_m}\right)\delta x - \frac{V_{\rm dc}}{m}\frac{\partial C(x)}{\partial x}\delta V_s(t) - \frac{\delta F_{\rm ext}}{m} = 0. \tag{14}$$

Assuming that the quantity $(\Delta\Omega_m)^2$ is negligible,

$$\frac{d^2\delta x}{dt^2} + \Gamma_m \frac{d\delta x}{dt} + \widetilde{\Omega}_m^2 \delta x - \frac{V_{\rm dc}}{m}\frac{\partial C(x)}{\partial x}\delta V_s(t) - \frac{\delta F_{\rm ext}}{m} = 0. \tag{15}$$

Equation 15 is readily solved in frequency space. After taking the Fourier transform, we find

$$\boxed{-\omega^2 \delta X(j\omega) - j\omega\Gamma_m \delta X(j\omega) + \Omega_m^2 \delta X(j\omega) - \frac{V_{\rm dc}}{m}\frac{\partial C(x)}{\partial x}\delta V_s(j\omega) - \frac{\delta F_{\rm ext}(j\omega)}{m} = 0}. \tag{16}$$

For notational convenience, note that the resonant frequency Ω_m has been redefined to equal the reduced resonant frequency (i.e. $\Omega_m = \widetilde{\Omega}_m$). In Equation 16, and throughout the paper, we have used the $e^{-j\omega t}$ convention, and denote Fourier transform pairs as $X(j\omega) \Leftrightarrow x(t)$.

A.1.2 Signal Readout

For the bare system without an integrated LC resonator, the application of an external force or bias voltage results in a mechanical displacement as well as a corresponding optical phase shift. Therefore, the transduction performance can be analyzed by considering both mechanical and optical readouts.

Assuming the applied bias signal dominates the response of the system, the resulting electromechanical transfer function, which defines the mechanical motion in response to an electrical excitation, is

$$\frac{\delta X(j\omega)}{\delta V_s(j\omega)} = \frac{V_{\rm dc}}{m(\Omega_m^2 - \omega^2 - j\omega\Gamma_m)}\frac{\partial C(x)}{\partial x}\bigg|_{x=x_0} = V_{\rm dc}\chi_m^0 \frac{\partial C(x)}{\partial x}\bigg|_{x=x_0}, \tag{17}$$

where $\chi_m^0 \equiv \frac{\delta X(j\omega)}{\delta F_{\rm ext}(j\omega)}\Big|_{\delta V_s = 0} = \frac{1}{m(\Omega_m^2 - \omega^2 - j\omega\Gamma_m)}$ is the mechanical susceptibility for the external force-dominated system where δV_s is negligible.

The displacement-induced interaction with a weakly-confined waveguide mode results in optomechanical transduction which modifies the overall system gain. The optomechanical system consists the mechanical oscillator placed horizontally above a parallel underlying waveguide. Displacements of the mechanical resonator result in a controllable interaction with the large evanescent field of the waveguide, which changes the waveguide's effective index of refraction $n_{\text{eff}}(x)$ as a function of the vertical displacement x along the horizontal length of the resonator. For a phase shifter mounted in a Mach-Zehnder interferometer (MZI) [17], the resulting optical phase shift can be written as [12]

$$\Delta\phi = kL_{\text{MEMS}}\Delta n_{\text{eff}}(x), \tag{18}$$

where $k = 2\pi/\lambda$ is the wave number, L_{MEMS} is the horizontal length of the resonator, and x is the vertical displacement from h_{MEMS}, the average gap between the waveguide and overlying resonator. To first order, the effective index can be approximated as

$$n_{\text{eff}}(x_0 + \delta x) = n_{\text{eff}}(h_{\text{MEMS}}) + \underbrace{\frac{\partial n_{\text{eff}}}{\partial x}\Big|_{x_0=h_{\text{MEMS}}}\delta x}_{\Delta n_{\text{eff}}} = n_{\text{eff}}(h_{\text{MEMS}}) + G_{om}\delta x. \tag{19}$$

Here, we have defined the optomechanical coupling parameter $G_{om} \equiv \partial n_{\text{eff}}/\partial x\big|_{x_0=h_{\text{MEMS}}}$. The relationship between x, the equilibrium displacement, and h_{MEMS}, the average microbridge-waveguide gap, is clarified in Figure 7.

The overall device transfer function is simply the product of those for the electromechanical and optomechanical systems:

$$\boxed{T_{\text{bare}} = \frac{\delta\Phi(j\omega)}{\delta V_s(j\omega)} = \frac{2\pi}{\lambda}V_{\text{dc}}\chi_m^0 L_{\text{MEMS}}G_{om}\frac{\partial C(x)}{\partial x}\bigg|_{x=x_0}}. \tag{20}$$

A.2 Method II: *LC* Coupled System

A.2.1 Equation of Motion – DC Biased

Following the procedure and analysis technique proposed in [4], an alternative Lagrangian derivation can be implemented to determine the transducer's equations of motion. The Lagrangian [19] for the coupled system shown in Figure 39 can be expressed as

$$\mathcal{L}(x, \dot{x}, q, \dot{q}) = T - U = \frac{1}{2}m\dot{x}^2 + \frac{1}{2}L\dot{q}^2 - \left(\frac{1}{2}m\Omega_m^2 x^2 + \frac{q^2}{2C(x)} + qV_B\right), \tag{21}$$

where q is the charge on the capacitor and x is the center-of-mass displacement from equilibrium. Solving the Euler-Lagrange equation for the generalized coordinates x and q yields the equations of motion

$$\frac{d^2q}{dt^2} + \Gamma_{LC}\frac{dq}{dt} + \Omega_{LC}^2 q - \frac{1}{L}(V_b(t) + V_s(t)) = 0 \qquad \frac{d^2x}{dt^2} + \Omega_m^2 x - \frac{q^2}{2mC(x)^2}\frac{\partial C(x)}{\partial x} = 0, \tag{22}$$

where $\Gamma_{LC} = R/L$ is the electrical damping rate. This system can be further generalized by incorporating a mechanical damping force $m\Gamma_m\dot{x}$ and an external mechanical noise force F_{ext}. The generalized system is therefore

$$\frac{d^2q}{dt^2} + \Gamma_{LC}\frac{dq}{dt} + \Omega_{LC}^2 q - \frac{1}{L}(V_b(t) + V_s(t)) = 0 \tag{23a}$$

$$\frac{d^2x}{dt^2} + \Gamma_m\frac{dx}{dt} + \Omega_m^2 x - \frac{q^2}{2mC(x)^2}\frac{\partial C(x)}{\partial x} - \frac{F_{\text{ext}}}{m} = 0. \tag{23b}$$

Similar to the bare system, we can linearize these equations of motion about an equilibrium position established by a constant DC bias $V_B = V_{dc}$. The equilibrium position is found by equating the microbridge's spring force to the capacitive force $F_c = -\partial U_c/\partial x$, yielding

$$x_0 = \frac{q_0^2}{2m\Omega_m^2 C(x_0)^2}\frac{\partial C(x)}{\partial x}\bigg|_{x=x_0} \tag{24}$$

in which the equilibrium charge $q_0 = C(x_0)V_{dc}$ is established by the capacitance at a given DC bias voltage.

The system in Equation 23 can be linearized about the equilibrium position x_0, q_0 to determine the effect of harmonic perturbations on the oscillator dynamics [4]. To first order, mechanical displacements about equilibrium can be expressed as

$$\frac{d^2\delta x}{dt^2} + \Gamma_m\frac{d\delta x}{dt} + \Omega_m^2\delta x - \frac{q_0}{mC(x_0)^2}\frac{\partial C(x)}{\partial x}\bigg|_{x=x_0}\delta q \underbrace{-\frac{q_0^2}{2mC(x)^2}\frac{\partial^2 C(x)}{\partial x^2}\bigg|_{x=x_0}}_{2\Omega_m\Delta\Omega_m}\delta x - \frac{\delta F_{\text{ext}}}{m} = 0. \tag{25}$$

while fluctuations in charge are represented by

$$\frac{d^2\delta q}{dt^2} + \Gamma_{LC}\frac{d\delta q}{dt} + \frac{1}{LC(x_0)}\delta q - \frac{q_0}{LC(x_0)^2}\frac{\partial C(x)}{\partial x}\bigg|_{x=x_0}\delta x - \frac{1}{L}\delta V_s(t) = 0 \tag{26}$$

Note that, as with the bare system in Section A.1.1, Equation 25 can be simplified by approximating the capacitively reduced mechanical resonance frequency as $\widetilde{\Omega}_m^2 \approx \Omega_m^2 - 2\Omega_m\Delta\Omega_m$. Redefining Ω_m to the reduced resonance frequency (i.e. $\widetilde{\Omega}_m = \Omega_m - \Delta\Omega_m \to \Omega_m$) and introducing the electromechanical coupling parameter [19]

$$G_{\text{em}} = \frac{\partial\Omega_{LC}}{\partial x}\bigg|_{x=x_0} = -\frac{\Omega_{LC}}{2C(x_0)}\frac{\partial C(x)}{\partial x}\big|_{x=x_0}, \tag{27}$$

the equations of motion are

$$\frac{d^2\delta x}{dt^2} + \Gamma_m\frac{d\delta x}{dt} + \Omega_m^2\delta x + \frac{2V_{dc}}{m\Omega_{LC}}G_{em}\delta q - \frac{\delta F_{\text{ext}}}{m} = 0 \tag{28a}$$

$$\frac{d^2\delta q}{dt^2} + \Gamma_{LC}\frac{d\delta q}{dt} + \Omega_{LC}^2\delta q + \frac{2V_{dc}}{L\Omega_{LC}}G_{em}\delta x - \frac{1}{L}\delta V_s(t) = 0. \tag{28b}$$

This coupled, linearized system – analogous to the canonical cavity optomechanical system [3] which embodies coupled light-mater interactions – illustrates that electrical excitations induce a mechanical displacement, and that these displacements in turn yield a corresponding electrical excitation [19] as the displacements change the capacitance (and thus move charges onto or off of the microbridge). Furthermore, the strength of these exchanges is governed by the electromechanical coupling parameter G_{em}.

In frequency space, the system is represented as

$$(\Omega_m^2 - \omega^2 - j\Gamma_m\omega)\delta X(j\omega) + \frac{2V_{dc}}{m\Omega_{LC}}G_{em}\delta Q(j\omega) - \frac{\delta F_{\text{ext}}(j\omega)}{m} = 0 \tag{29a}$$

$$(\Omega_{LC}^2 - \omega^2 - j\Gamma_{LC}\omega)\delta Q(j\omega) + \frac{2V_{dc}}{L\Omega_{LC}}G_{em}\delta X(j\omega) - \frac{1}{L}\delta V_s(j\omega) = 0. \tag{29b}$$

A.2.2 Signal Readout

In addition to the optical and mechanical signal readouts of the bare system, the coupled system also enables electrical readout via measurement of the voltage across the microbridge capacitor $C(x)$. Due to the interaction between the electrical and mechanical resonators, the transducer's susceptibility to voltage and force inputs differs from those of the bare system in Section A.1.1. From Equation 29, the modified mechanical and electrical susceptibilities for the coupled system are realized:

$$\chi_m(j\omega) \equiv \left.\frac{\delta X(j\omega)}{\delta F_{\text{ext}}(j\omega)}\right|_{\delta V_s=0} = \left[\frac{1}{\chi_m^0(j\omega)} - \frac{4V_{dc}^2 G_{em}^2}{\Omega_{LC}^2}\chi_{LC}^0(j\omega)\right]^{-1} \tag{30a}$$

$$\chi_{LC}(j\omega) \equiv \left.\frac{\delta Q(j\omega)}{\delta V_s(j\omega)}\right|_{\delta F_{\text{ext}}=0} = \left[\frac{1}{\chi_{LC}^0(j\omega)} - \frac{4V_{dc}^2 G_{em}^2}{\Omega_{LC}^2}\chi_m^0(j\omega)\right]^{-1}, \tag{30b}$$

where $\chi_{LC}^0 \equiv \left.\frac{\delta Q(j\omega)}{\delta V_s(j\omega)}\right|_{\delta F_{\text{ext}}=0} = \frac{1}{L(\Omega_{LC}^2-\omega^2-j\omega\Gamma_{LC})}$. These susceptibilities, along with Equation 29, can then be utilized to determine the mechanical response of the transducer for a small input force and voltage:

$$\delta X(j\omega) = \chi_m(j\omega)\delta F_{\text{ext}}(j\omega) - \frac{2V_{dc}}{\Omega_{LC}} G_{em}\chi_m^0\chi_{LC}(j\omega)\delta V_s(j\omega) \tag{31}$$

Assuming the electrical input δV_s causes the second term in Equation 31 to dominate the system response, the mechanical transfer function is

$$\frac{\delta X(j\omega)}{\delta V_s(j\omega)} = -\frac{2V_{dc}}{\Omega_{LC}} G_{em}\chi_m^0\chi_{LC} \tag{32}$$

which, when combined with the constant optical transfer function from Section A.1.2, yields the optical transfer function

$$\boxed{T_{\text{coupled}} = \frac{\delta\Phi(j\omega)}{\delta V_s(j\omega)} = \frac{\delta X(j\omega)}{\delta V_s(j\omega)}\frac{\delta\Phi(j\omega)}{\delta X(j\omega)} = -\frac{2\pi}{\lambda}\frac{2V_{dc}}{\Omega_{LC}}\chi_m^0\chi_{LC}L_{\text{MEMS}}G_{om}G_{em}}. \tag{33}$$

The electrical output, found by probing the voltage V_c across the parametric capacitance $C(x)$ in Figure 39, is [4]

$$\frac{\delta V_c(j\omega)}{\delta V_s(j\omega)} = \left[\frac{1}{C(x_0)} - \frac{4V_{dc}^2}{\Omega_{LC}^2}G_{em}^2\chi_m^0\right]\chi_{LC}. \tag{34}$$

A.2.3 Equation of Motion – AC Biased

As evidenced here, the proposed transduction architecture is intrinsically narrow-band, since high-Q resonators are required to achieve optimal gain. One proposed alternative [4, 29] to extend the scheme to a larger bandwidth is to apply an AC bias to the microbridge resonator. In this system, the AC bias frequency could potentially mix the input electrical signal's frequency into the narrow mechanical resonance, thus serving to extend the functional bandwidth [29]. We aim to both theoretically and experimentally study such a system in order to determine its feasibility.

Appendix B Mach-Zehnder Interferometer Transfer Function Derivation

A phasor approach can be utilized to determine the Mach-Zehnder interferometer (MZI) transfer function, or the ratio of the interferometer's output and input intensities. If the MZI is composed of two identical arms of the same length and material composition, light split into the two arms will recombine constructively at the device output. However, as depicted by Figure 38, the introduction of a physical path length difference and a microbridge phase shifter results in the recombination of two phase shifted signals, which yields a variable output intensity. For the case of a physical path length imbalance ΔL_{MZI} and a microbridge phase shifter of length L_{MEMS} added to opposite interferometer arms, the ratio of output and input electric field amplitudes, E_o and E_i, respectively, can be expressed as

$$\frac{E_o}{E_i} = \frac{1}{2}\left[e^{-j(\beta\Delta L_{\text{MZI}})} + e^{-j(\Delta\beta L_{\text{MEMS}})}\right], \tag{35}$$

where $\beta = 2\pi n_{\text{eff}}/\lambda$ and $\Delta\beta = 2\pi\Delta n_{\text{eff}}/\lambda$ for a given input laser wavelength λ, waveguide effective index n_{eff}, and microbridge-induced change in effective index Δn_{eff}.

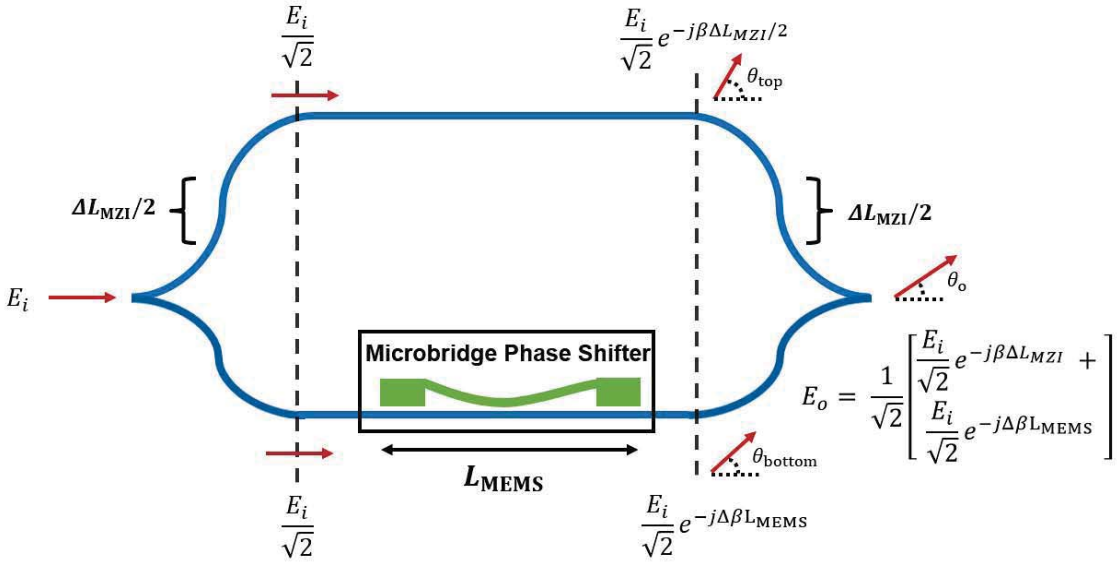

Figure 38: A simplified phasor representation of wave propagation through the Mach-Zehnder interferometer. The electric field amplitude and phase $Ee^{-j\theta}$ is listed at various points throughout the propagation path.

Since intensity is proportional to the square of electric field amplitude, the intensity ratio I_o/I_i can be simplified to:

$$\begin{aligned}
\frac{I_o}{I_i} &= \frac{1}{4}\left|e^{-j(\beta\Delta L_{\mathrm{MZI}})} + e^{-j(\Delta\beta L_{\mathrm{MEMS}})}\right|^2 \\
&= \frac{1}{4}\left|e^{-j\theta_{\mathrm{top}}} + e^{-j\theta_{\mathrm{bottom}})}\right|^2 \\
&= \frac{1}{4}\left[2\cos\left(\frac{\theta_{\mathrm{top}} - \theta_{\mathrm{bottom}}}{2}\right)\right]^2 \\
&= \cos^2\left(\frac{\theta_{\mathrm{top}} - \theta_{\mathrm{bottom}}}{2}\right) \\
&= \cos^2\left(\frac{2\pi n_{\mathrm{eff}}\Delta L_{\mathrm{MZI}}}{2\lambda} - \frac{2\pi\Delta n_{\mathrm{eff}} L_{\mathrm{MEMS}}}{2\lambda}\right) \\
&= \frac{1}{2}\left[1 + \cos\left(\frac{2\pi n_{\mathrm{eff}}\Delta L_{\mathrm{MZI}}}{\lambda} - \frac{2\pi\Delta n_{\mathrm{eff}} L_{\mathrm{MEMS}}}{\lambda}\right)\right] \\
\frac{I_o}{I_i} &= \frac{1}{2}\left\{1 + \cos\Big[\underbrace{\frac{2\pi}{\lambda^2}\left(n_{\mathrm{eff}}\Delta L_{\mathrm{MZI}} - \Delta n_{\mathrm{eff}} L_{\mathrm{MEMS}}\right)}_{k_{\mathrm{MZI}} = \frac{2\pi}{\mathrm{FSR}}}\lambda\Big]\right\}.
\end{aligned} \tag{36}$$

The period of the resulting sinusoidal spectrum, termed the free spectral range (FSR) is therefore

$$\mathrm{FSR} = \frac{\lambda^2}{n_{\mathrm{eff}}\Delta L_{\mathrm{MZI}} - \Delta n_{\mathrm{eff}} L_{\mathrm{MEMS}}}. \tag{37}$$

Although the FSR is a function of wavelength, it can be approximated as constant so long as the wavelength range is sufficiently narrow (where "narrow" depends upon the accuracy required).

The group index n_g governs the speed of pulse propagation in the MZI and can be written as [13]

$$n_g = \frac{\lambda^2}{\Delta L_{\mathrm{MZI}}(\mathrm{FSR})}. \tag{38}$$

Substituting the derived FSR, the group index is found to be

$$n_g = \frac{n_{\mathrm{eff}}\Delta L_{\mathrm{MZI}} - \Delta n_{\mathrm{eff}} L_{\mathrm{MEMS}}}{\Delta L_{\mathrm{MZI}}} = n_{\mathrm{eff}} - \frac{\Delta n_{\mathrm{eff}} L_{\mathrm{MEMS}}}{\Delta L_{\mathrm{MZI}}}. \tag{39}$$

Therefore, a decrease in the group index is expected when a microbridge in placed atop one of the waveguide arms of the interferometer. This shift is experimentally measured in Section 11.

Appendix C Theoretical Analysis of the *LC* Coupled Transducer

C.1 Electromechanical *LC* Coupled System

To enhance the efficiency of coupling between the input electrical signal and the resulting mechanical displacement, the microbridge can also be capacitively coupled to an electronic LC resonator. As a result, the voltage induced across the microbridge from an incident RF signal is magnified, and yields a larger displacement. In this configuration, similar to the bare system, an electrical excitation displaces the microbridge. As a result, the displacement-dependent parametric capacitance $C(x)$ of the microbridge changes, yielding a corresponding shift in the electrical resonance frequency $\Omega_{LC} = 1/\sqrt{LC(x)}$. A schematic diagram of the coupled system is shown in Figure 39. By tuning the LC resonant frequency to that of the microbridge, the electrical resonator affords a significant gain enhancement and, when the oscillators are strongly coupled [14], also allows for the realization of physical phenomena such as normal mode splitting and electromechanically induced transparency (EMIT) [15, 16].

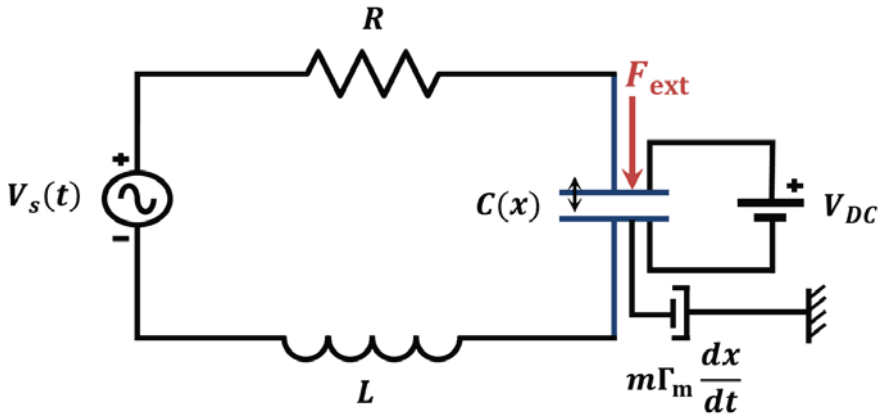

Figure 39: A schematic diagram of the coupled oscillator system. An electrical excitation potential $V_s(t)$ is injected into the RLC resonator, which displaces the parametric capacitance $C(x)$ formed by the flexible, electrostatically actuated microbridge (blue). The bridge, which is directly biased by the potential $V_{\rm dc}$, is damped at a rate Γ_m and is displaced by an external noise force $F_{\rm ext}(t)$.

The resulting frequency space transfer function (derived in Appendix A) is

$$T_{\rm coupled} = \frac{\delta\Phi(j\omega)}{\delta V_s(j\omega)} = \frac{\delta X(j\omega)}{\delta V_s(j\omega)}\frac{\delta\Phi(j\omega)}{\delta X(j\omega)} = -\left(\frac{2\chi_{LC}}{\Omega_{LC}}\chi_m^0 G_{em} V_{dc}\right)\left(\frac{2\pi}{\lambda}G_{om}L_{\rm MEMS}\right), \tag{40}$$

where the electromechanical coupling coefficient

$$G_{\rm em} = \left.\frac{\partial\Omega_{LC}}{\partial x}\right|_{x=x_0} = -\frac{\Omega_{LC}}{2C(x_0)}\left.\frac{\partial C(x)}{\partial x}\right|_{x=x_0}, \tag{41}$$

in units of rad $\rm s^{-1}m^{-1}$ describes the strength of coupling between the LC resonance circuit and mechanical microbridge, and

$$\chi_{LC}(j\omega) \equiv \left.\frac{\delta Q(j\omega)}{\delta V_s(j\omega)}\right|_{\delta F_{\rm ext}=0} = \left[\frac{1}{\chi_{LC}^0(j\omega)} - \frac{4V_{dc}^2 G_{em}^2}{\Omega_{LC}^2}\chi_m^0(j\omega)\right]^{-1}, \tag{42}$$

is the coupled electrical susceptibility (capacitor charge fluctuation δQ to input voltage fluctuation δV_s transfer function) which has been modified from the uncoupled ($V_{\text{dc}} = 0$) form $\chi^0_{LC} \equiv \left.\frac{\delta Q(j\omega)}{\delta V_s(j\omega)}\right|_{\delta F_{\text{ext}}=0} = \frac{1}{L(\Omega^2_{LC}-\omega^2-j\omega\Gamma_{LC})}$.

C.1.1 Optimum Coupling and Half-Wave Voltage

For peak phase transduction, there exists an optimal electromechanical coupling strength which can be found by maximizing Equation 40 with respect to G_{em}. At resonance ($\omega = \Omega_{LC} = \Omega_m$), the magnitude of T_{coupled} is maximized and the optimal coupling parameter is found to be

$$G_{em}^{\text{optimal}} = \frac{\Omega^2_{LC}}{2V_{dc}}\sqrt{mL\Gamma_m\Gamma_{LC}}. \tag{43}$$

If this peak coupling value is achieved, the half-wave voltage, i.e., the input voltage required to achieve an optical phase shift of π radians [17], is derived from Equation 40 to be

$$V_\pi\big|^{\omega=\Omega_{LC}=\Omega_m}_{G_{em}=G_{em}^{\text{optimal}}} = \frac{\lambda\Omega_m\sqrt{mL\Gamma_{LC}\Gamma_m}}{L_{\text{MEMS}}G_{om}}. \tag{44}$$

C.1.2 Default Parameters and Predicted Performance

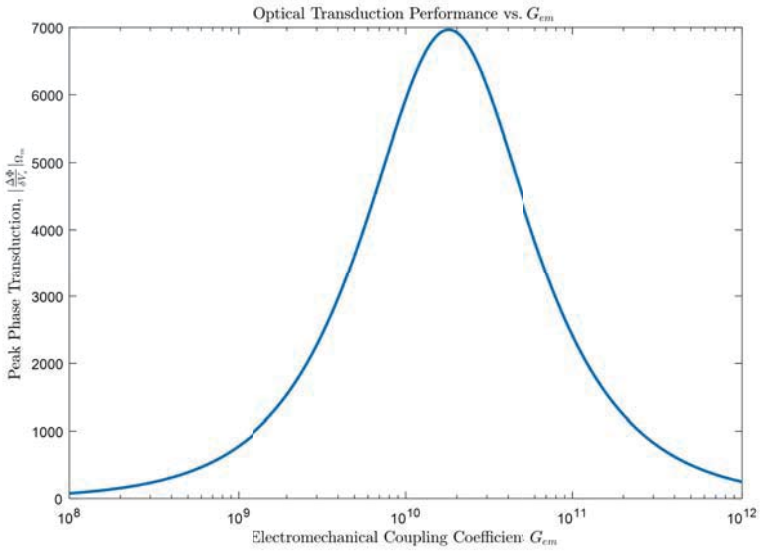

Figure 40: On resonance ($\omega = \Omega_m$) phase transduction gain for a variable electromechanical coupling coefficient (in units Hz/m). For peak phase transduction gain, the device should be designed to meet the peak coupling value.

The peak phase transduction for a system described by the default parameters in Table 2 is plotted against the coupling parameter G_{em} in Figure 40. The maximum gain of ~7000 rad/V at $G_{em} = G_{em}^{\text{optimal}} \approx 2\times10^{10}$ Hz/m dramatically exceeds that of the default system in which $G_{em} = 10^7$ Hz/m $\ll G_{em}^{\text{optimal}}$. Here, the optimal coupling coefficient for maximum gain is much larger than the values of G_{em} reported in recent literature [19], which can be primarily attributed to the low default mechanical Q-factor (103) used. For the revised parameters in Table 3, due to the increase

Parameter	Value	Description	Source
λ	1550 nm	Optical wavelength	Typical value
$[L, w, t]_{\text{MEMS}}$	[75, 250, 3.0] μm	Length, width, and thickness of SiN_x MEMS resonator	[12]
m	$\rho_{SiN_x} L_{\text{MEMS}} w_{\text{MEMS}} t_{\text{MEMS}}$	Physical mass of MEMS microbridge	[18]
Q_m	103	MEMS microbridge quality factor Ω_m/Γ_m	[12]
Ω_m	$2\pi \times 2.3$ MHz	Microbridge fundamental resonance frequency	[12]
V_{dc}	4.3 V	DC bridge bias voltage	[12]
Ω_{LC}	$2\pi \times 2.3$ MHz	LC resonance frequency (set equal to Ω_m)	[12]
R	20Ω	RLC circuit resistance	[4]
L	.64 mH	LC inductance	[4]
C	$1/(L\Omega_m^2)$	LC capacitance (set with tuning capacitor such that $\Omega_{LC} = \Omega_m$)	[4]
Γ_{LC}	R/L	LC damping rate	Standard value
G_{em}	10^7 Hz/m	Standard electromechanical coupling parameter $\partial\Omega_{LC}/\partial x$	[19]
G_{om}	.488 μm^{-1}	Optomechanical coupling parameter $\partial n_{\text{eff}}/\partial x$	[12]

Table 2: Default parameters for estimating the performance of the coupled RF-to-optical transducer.

Parameter	Value	Description	Source
$[L, w, t]_{\text{MEMS}}$	[250, 250, 3.0] μm	Length, width, and thickness of SiN_x MEMS resonator	[12]
Q_m	10^4	MEMS microbridge quality factor Ω_m/Γ_m	Reasonable value for microbridge in vacuum
Ω_m	$2\pi \times 1.0$ MHz	Microbridge fundamental resonance frequency	Approximate resonant frequency of 250 micron microbridges derived from FEM simulations
V_{dc}	5 V	DC bridge bias voltage	Typical bias voltage before device pull-in
G_{em}	10^8 Hz/m	Standard electromechanical coupling parameter $\partial\Omega_{LC}/\partial x$	Upper bound of FEM simulation results

Table 3: Revised system parameters based upon the results of the FEM simulations detailed in Section 6. Unlisted parameters are equivalent in value to those listed in Table 2.

in Q_m to 10^4, the optimal electromechanical coupling coefficient is on the order of 10^8 Hz/m – a much more realistically achievable value.

Assuming that the optimal coupling coupling coefficient is met, the transducer's half-wave voltage as a function of resonant frequency can be plotted, as in Figure 41 for the parameters in Table 3. The results demonstrate that half-wave voltages on the order of 10 μV should be achievable for 1 MHz oscillators, which represents over an order of magnitude improvement compared to recent devices [4].

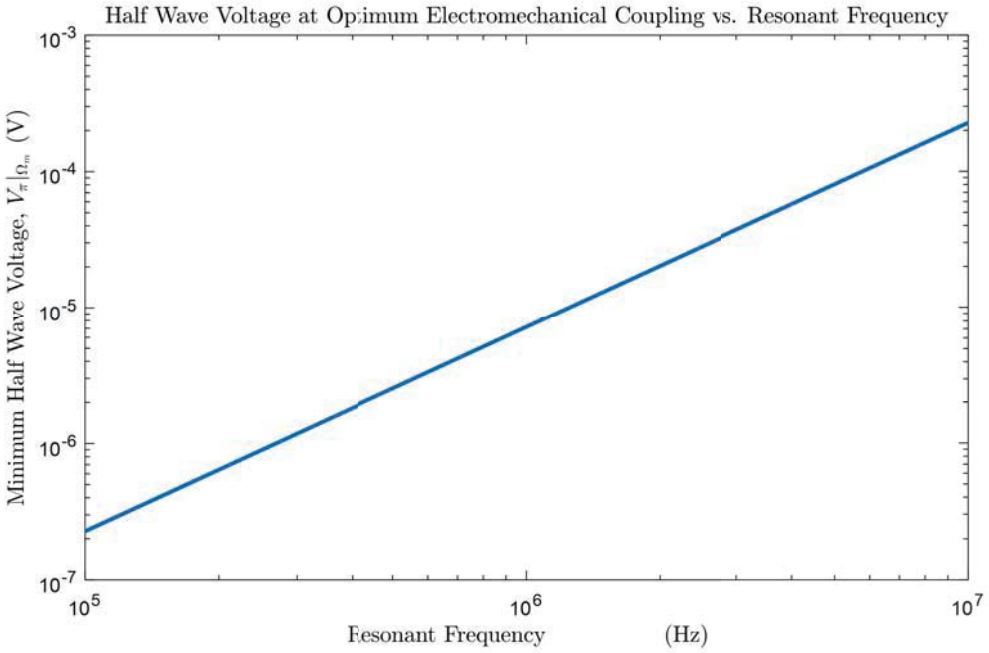

Figure 41: V_π plotted against the resonant frequency $\Omega = \Omega_m = \Omega_{LC}$ for the parameters in Table 3 assuming the optimal coupling strength is achieved. The results indicate that 10μV half wave voltages should be achievable for 1 MHz oscillators.

C.1.3 Device Input Impedance

To maximize power transfer between the source and transducer, the input impedance of the device should match that of the source. The input impedance is expressed as

$$Z_{\text{in}}(j\omega) = \frac{\delta V_s(j\omega)}{\delta I_s(j\omega)} = \frac{\delta V_s(j\omega)}{-j\omega\delta Q(j\omega)} = \frac{-1}{j\omega\chi_{LC}}. \tag{45}$$

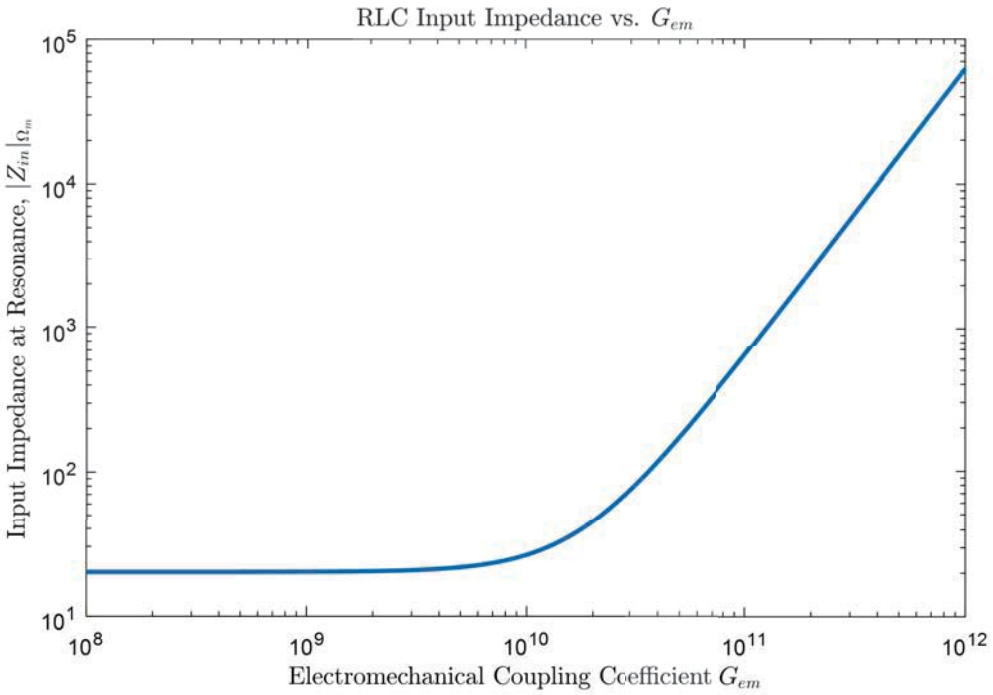

Figure 42: Transducer input impedance for the device characterized by the default parameters listed in Table 2 (with G_{em} in units of Hz/m and impedance in ohms). The weakly coupled system's impedance is approximately R (20Ω here), but grows significantly for $G_{em} > G_{em}^{\text{optimal}}$.

Figure 42 depicts the typical trend for input impedance – for weakly coupled oscillators, as expected, the input impedance is equal to the RLC resistance R; however, as G_{em} increases, the input impedance increases significantly.

C.1.4 Gain from *LC* Resonator

As previously mentioned, the incorporation of a coupled LC resonator yields a significant enhancement in transduction performance. Quantitatively, the LC resonator gain

$$\text{Gain}_{LC} = \left|\frac{T_{\text{coupled}}}{T_{\text{bare}}}\right| = \frac{\chi_{LC}}{C(x_0)} \tag{46}$$

is found by dividing the coupled and bare device transfer functions. As expected for the limiting case of $G_{em} = 0$ (uncoupled), the LC gain simplifies to

$$\text{Gain}_{LC}|_{G_{em}\to 0} = \frac{\Omega_{LC}}{\Gamma_{LC}} = Q_{LC},$$

where Q_{LC} is the traditional quality factor of an LC resonator. However, as the electromechanical coupling is increased, χ_{LC} decreases, and the LC gain rapidly approaches zero. These trends are depicted for a default system in Figure 43.

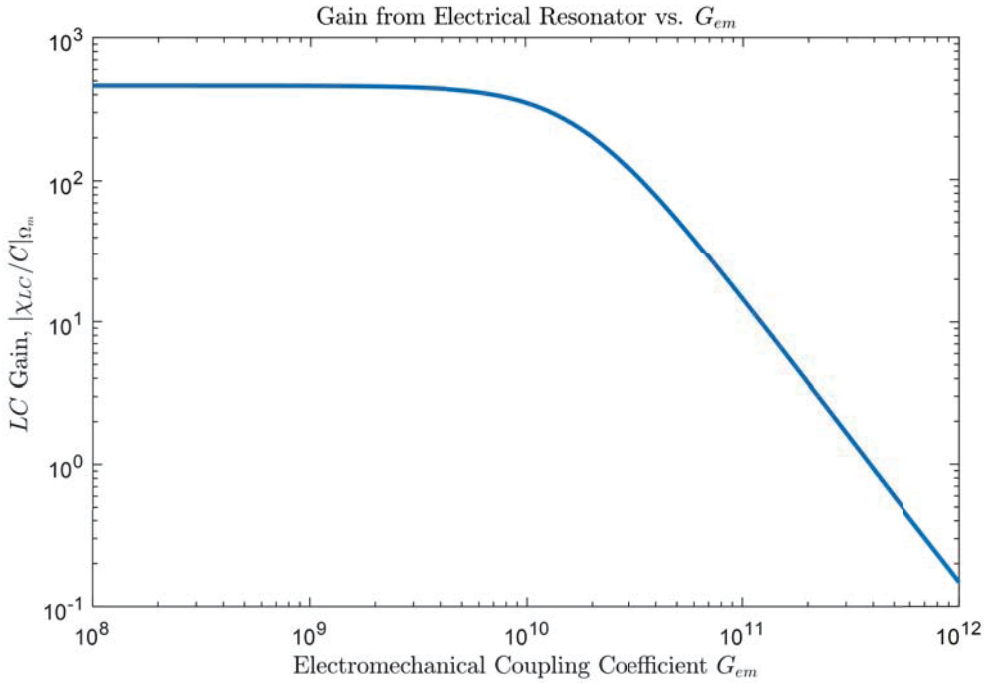

Figure 43: LC gain vs. electromechanical coupling coefficient G_{em} (shown in Hz/m) for the coupled system described by the default parameters outlined in Table 2 with $G_{em}^{\text{optimal}} \approx 10^{10}$ Hz/m. For $G_{em} \ll G_{em}^{\text{optimal}}$, the gain is approximately equal to the quality factor of the LC resonator.

Appendix D Transfer Function Behavior, Scaling, and Default Parameters

Given the coupled device transfer function T_{coupled}, the overall transducer gain can be approximated using a set of default parameters derived from recent literature. Table 2 outlines the value and source of these parameters.

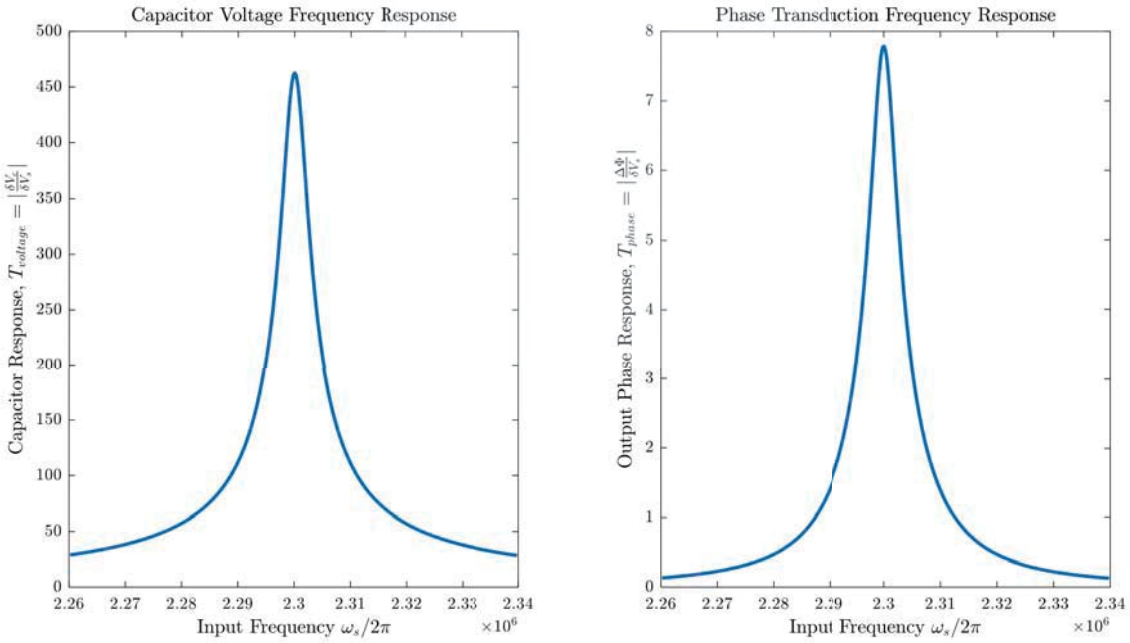

Figure 44: The electrical (left) and optical (right) frequency response for the coupled system described by the default parameters. On-resonance, the optical response indicates a half wave voltage of approximately 400 mV.

The electrical and optical response for the transducer characterized by these default parameters are shown in Figure 44. No characteristics of strong coupling, such as EMIT or normal mode splitting, are evident, and the peak phase transduction gain of ∼8 rad/V on resonance yields a half-wave voltage of approximately 400 mV. However, the system performance can be drastically improved by increasing the coupling strength and quality of the resonators.

Based on the FEM simulations discussed in Section 6, several default parameters were revised (see Table 3), yielding the modified system response shown in Figure 45. These changes in device metrics, most notably an increase in the mechanical quality factor to 10^4 and a increase of G_{em} by an order of magnitude, result in a system with a half-wave voltage of approximately 10 μV. Furthermore, as depicted by the narrow dip on resonance in the electrical frequency response, the strongly-coupled device illustrates electromechanically induced transparency (EMIT).

D.1 Strong Coupling

As an aside, we briefly summarize the effects which occur when the electrical and mechanical oscillators are strongly coupled. Strong coupling results in normal mode splitting, i.e. a split in the

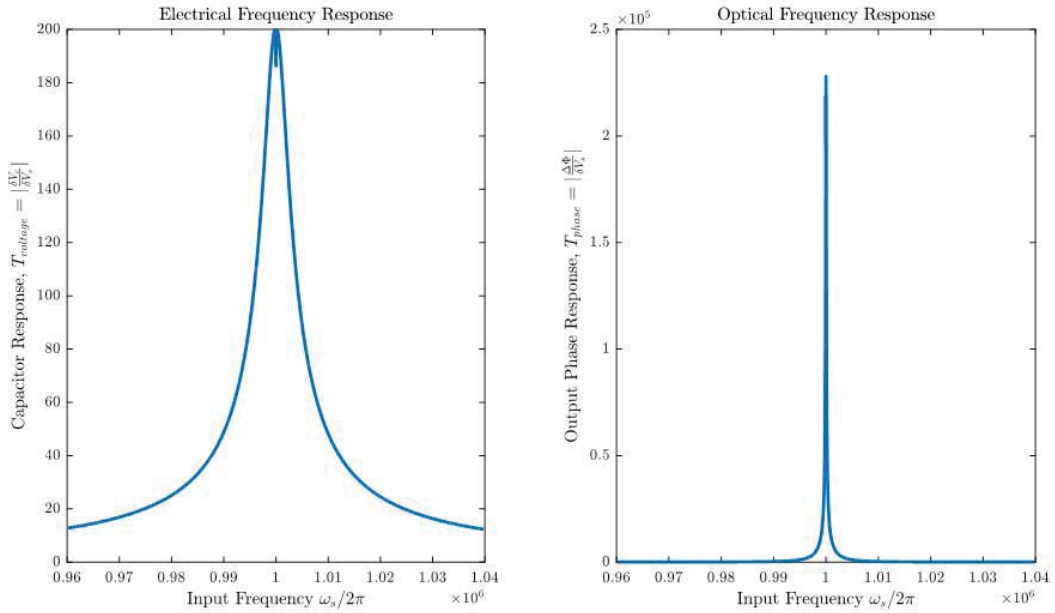

Figure 45: Electrical and optical system response for the coupled transducer described by updated parameters based upon the results of FEM COMSOL simulations (Table 3). From the computationally derived values, the system lies on the verge of strong coupling (as evidenced by the small dip in the electrical frequency spectrum resulting from electromechanically induced transparency) and yields revised half wave voltage on the order of 10 μV.

response's resonance peak as the degenerate electrical and mechanical modes hybridize into two normal electromechanical eigenmodes [4]. Theoretically, this occurs when the coupling rate [14]

$$g_{em} = G_{em} x_{\mathbf{zpf}} = G_{em} \sqrt{\frac{\hbar}{2m\Omega_m}} \tag{47}$$

(where $x^2_{\mathbf{zpf}} = \langle 0| \hat{x}^2 |0\rangle$ is the zero point fluctuation of the mechanical oscillator in the ground state $|0\rangle$) exceeds the damping rate of the mechanical and electrical resonators, Γ_m and Γ_{LC}, respectively [14]. Experimentally, the coupling rate can be found as half the frequency difference between the two hybridized resonant peaks in the device response [4]. Electromechanically induced transparency (EMIT), another phenomenon associated with strong coupling evidenced by a narrow dip in the device's resonant frequency response, occurs before normal mode splitting as the increasing coupling strength transitions the device between weak and strong coupling [4]. Although a strongly coupled device exhibits non-optimal phase transduction characteristics, it is still of interest for the device's potential application to coherent quantum state transfer [20].

D.2 Performance Scaling

By varying the parameters affecting T_{coupled}, the system behavior can be better understood under various conditions. Notably, the value of the electromechanical coupling parameter G_{em} determines whether the system is weakly or strongly coupled, and therefore has a dramatic effect upon the system dynamics.

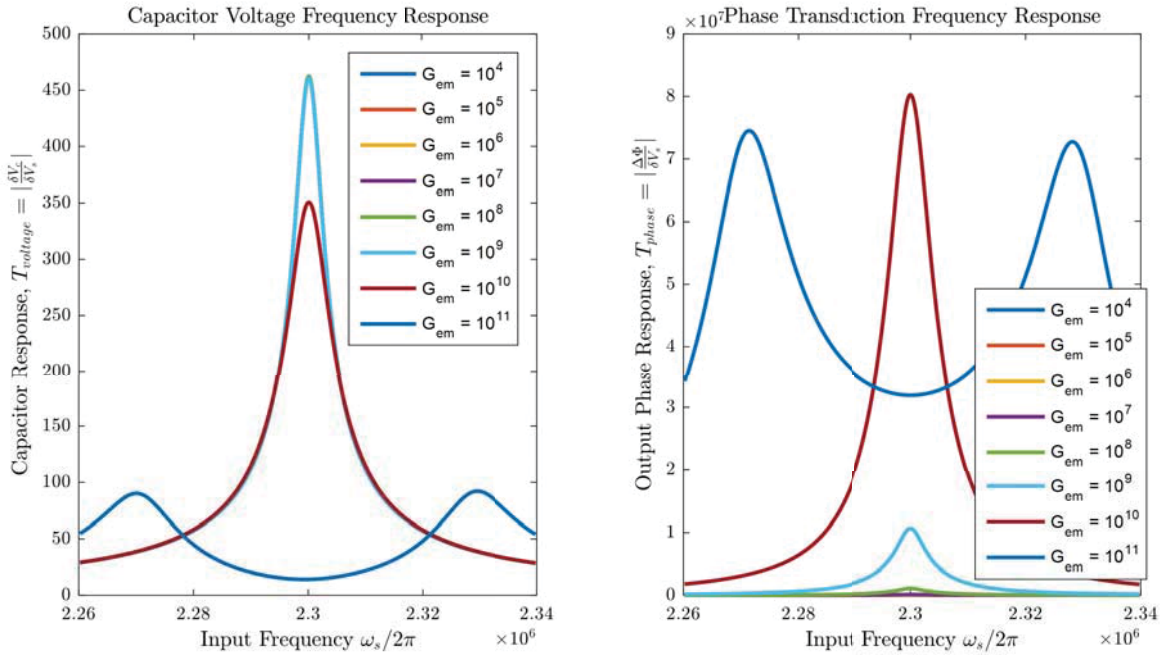

Figure 46: System response for varying coupling strengths. Peak phase transduction is achieved at the optimal coupling strength ($G_{em} \approx 10^{10}$ Hz/m. Past the optimum coupling rate, the oscillators become strongly coupled, as evidenced by the normal mode splitting seen within the electrical and optical responses.

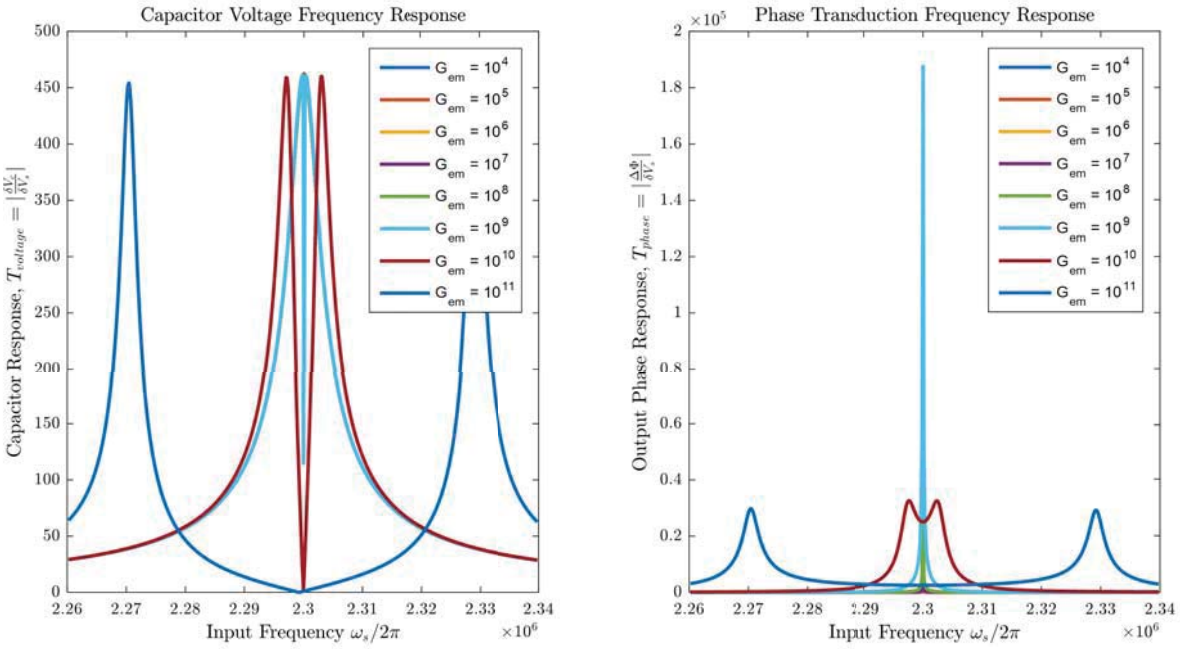

Figure 47: The system response resulting from an increased mechanical quality factor $Q_m = 10^5$. In this case, an optimal coupling coefficient value is clearly evident, since phase transduction is significantly damped for the instances of normal mode splitting.

Figure 46 demonstrates the change in the device's frequency response when G_{em} is swept across several orders of magnitude. Initially, when $G_{em} \ll 10^{10}$ Hz/m, increasing the coupling strength yields a direct improvement in the peak phase transduction as shown in the RHS of Figure 46. However, further increases in G_{em} past the peak value discussed in Section C.1.1 ($\sim 10^{10}$ Hz/m here) yield a normal mode splitting as depicted by the two resonant peaks in Figure 46 for $G_{em} = 10^{11}$ Hz/m.

The presence of an optimum coupling strength becomes readily apparent when considering higher-Q oscillators. Figure 47 demonstrates this effect for a modified system with $Q_m = 10^5$. Here, the onset of EMIT for $G_{em} = 10^{10}$ Hz/m is clearly visible, yielding a peak phase gain of nearly one order of magnitude larger than the strongly coupled system for higher values of G_{em}. Therefore, these results not only depict two phenomena associated with strongly coupled oscillators, but also further manifest the necessity of achieving the optimal coupling strength discussed in Section C.1.1 in order to realize peak transduction gain.

Appendix E Simulated Performance of *LC*-based System

E.1 Electromechanical Coupling

From the results of the DC bias study, the electromechanical coupling parameter $G_{em} = -\frac{\Omega_{LC}}{2C(x)}\frac{\partial C(x)}{\partial x}\Big|_{x=x_0}$ can be readily calculated. The results for each bridge length and bias point are shown in Figure 48. As expected, the coupling strength increases as the bridge is displaced further downwards (i.e., as V_{dc} increases). Although $\partial C(x_0)/\partial x$ increases for longer bridges, the decrease in resonant frequency outweighs this improvement, and the coupling strength thus favors shorter bridge lengths.

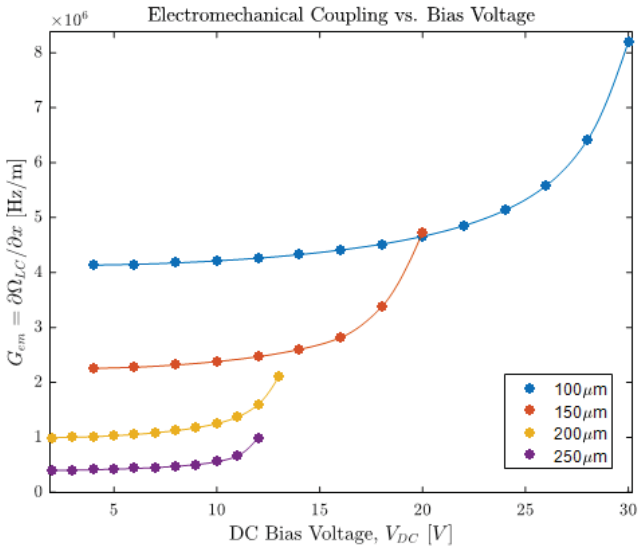

Figure 48: Electromechanical coupling parameter G_{em} for the bridge lengths studied in the DC bias analysis. As the bias approaches the pull-in voltage, the electromechanical coupling strength grows, as $G_{em} \propto \frac{\partial C(x)}{\partial x}$. It should be noted that a constant resonant frequency is assumed for each bridge length (i.e. not accounting for capacitive spring softening).

These coupling strengths can be compared to the optimal values derived in Section C.1.1. Figure 49 demonstrates that for both the original parameters listed in Table 2 as well as for improved resonator Q-factors listed in Table 3, the resulting electromechanical coupling strengths both fall short of the optimal values desired.

Based on the theoretical results provided in Appendix C, the parameters affecting optimal system design can be investigated. For a system specifically intended to minimize the half-wave voltage, Equations 41, 43, and 44 define the design parameters of greatest importance. In order to minimize the required optimal coupling strength for peak performance (maximum phase transduction gain), the system resonant frequency should be minimized. Furthermore, the mass of the microbridge, damping rates of the respective oscillators, and LC inductance should all be minimized. In contrast, to *attain* the optimal coupling condition, we seek to maximize G_{em}. The electromechanical coupling coefficient can be increased by: 1) increasing the resonant frequency (in opposition to the minimization sought for G_{em}^{optimal}); 2) minimizing the total capacitance; or 3) designing the capacitor geometry and appropriately biasing the device to maximize $\partial C(x)/\partial x$. A brief overview

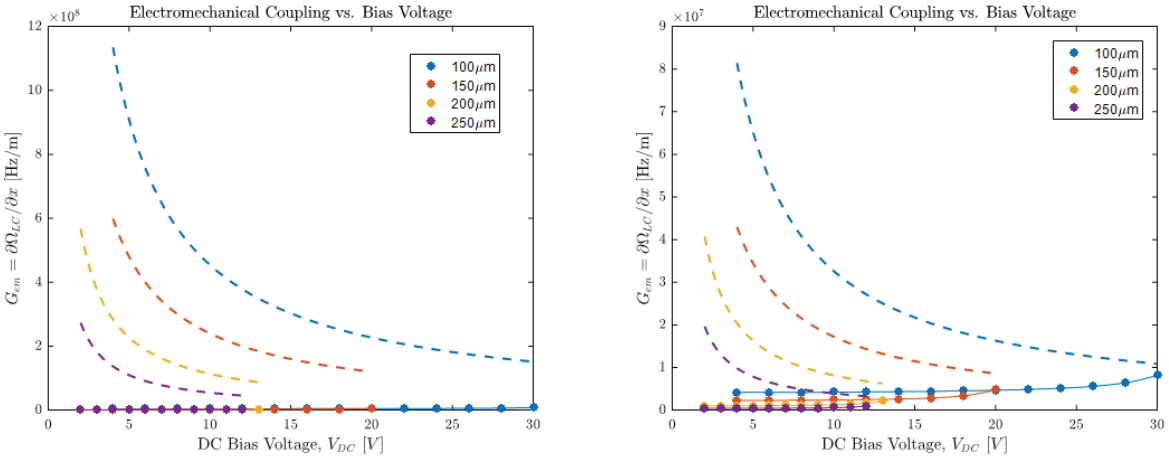

(a) $Q_m = 103$, $R = 20\Omega$ (b) $Q_m = 10^4$, $R = 10\Omega$

Figure 49: Derived and optimum values of G_{em} (solid and dotted, respectively) versus DC bias for various bridge lengths.

of these three considerations follows.

1. Particular notice should be paid to the optimal resonant frequency. The opposing trends of the optimal coupling $G_{em}^{\text{optimal}}(\propto \Omega_{LC}^2)$, which we seek to minimize, and $G_{em}(\propto \Omega_{LC})$, which must be increased to reach G_{em}^{optimal}, yield a half-wave voltage directly proportional to Ω_{LC}. As evidenced by the finite element method (FEM) simulations discussed in Section 6, an increased bridge length L_{MEMS} yields a greater mechanical compliance which reduces its resonant frequency Ω_m, thus improving (reducing) V_π through two parameters.

2. Minimizing the total capacitance significantly improves the maximum coupling strength since $G_{em} \propto C(x_0)^{-1}$. Ideally, this optimization can be achieved by mitigating parasitic capacitance and setting the inductance such that $\Omega_{LC} = \Omega_m$ for a minimal capacitance. The large resulting inductance does however degrade the minimum half wave voltage since $V_\pi \propto L^{1/2}$.

3. Finally, the capacitance tuning about the equilibrium point, $\frac{\partial C(x)}{\partial x}\big|_{x=x_0}$, should be enhanced. This can be achieved by either tuning the equilibrium point with the applied DC bias, or modifying the microbridge capacitor's geometry. These two methodologies are another focus of our modeling and simulation studies detailed in Section 6.

As demonstrated by this brief analysis, it is clear that the transducer's design must be carefully considered in order to minimize the half wave voltage V_π.

With this in mind, two possible options to achieve G_{em}^{optimal} are to: 1) change the values of L and C while maintaining a constant Ω_{LC}; and 2) to revise the device geometry to achieve greater capacitance tuning. We briefly investigate these two possibilities here.

E.2 Achieving Optimal Electromechanical Transduction – Varying *L*

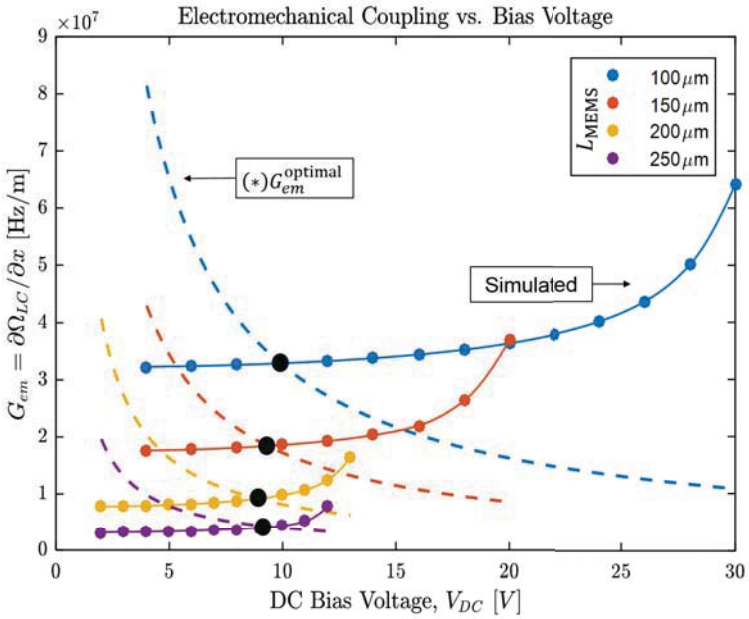

Figure 50: As depicted by the intersection of the optimal and simulated coupling curves (shown as black points), changing the LC circuit inductance from .64 mH to 5 mH enables optimal coupling to be achieved.

Assuming an LC inductance on the order of 1 mH (coinciding with the value listed in [4]), the required capacitance for a 1 MHz oscillator is on the order of 10 pF. Since the microbridge capacitance is roughly on the order of fF, a parallel tuning capacitor, which accounts for the vast majority of the circuit's overall capacitance, is required to achieve the desired resonance frequency [4]. By increasing the inductance, the required capacitance of this tuning capacitor, and therefore the overall capacitance, decrease significantly. Since $G_{em} \propto C(x_0)^{-1}$, this decrease in capacitance accounts for an increase in the coupling strength. The coupling strength resulting from incorporation of a larger 5 mH inductor (compared to the default value of .63 mH) is depicted in Figure 50. As indicated by the intersection of the simulated and optimal coupling curves, the experimental system should be able to be biased at the optimal coupling point for all simulated bridge lengths. As the bias voltage increases beyond optimal coupling, the results similarly indicate the possibility of achieving strong coupling.

Thus, these results clearly illustrate that a tunable inductance yields a feasible mechanism by which the coupling strength can be modified, and by which the transducer bias point can be varied between weak, optimal, and strong coupling regimes.

E.3 Achieving Optimal Electromechanical Transduction – Revised Geometry

Alternatively, the coupling strength can also be improved by optimizing the geometry. To increase the change in capacitance for a given displacement, the direct electrostatic geometry was modified by decreasing the height of the microbridge from 230 nm to 100 nm and decreasing the horizontal standoff distance of the side electrode from 1 micron to 100 nm. The principal advantage of the

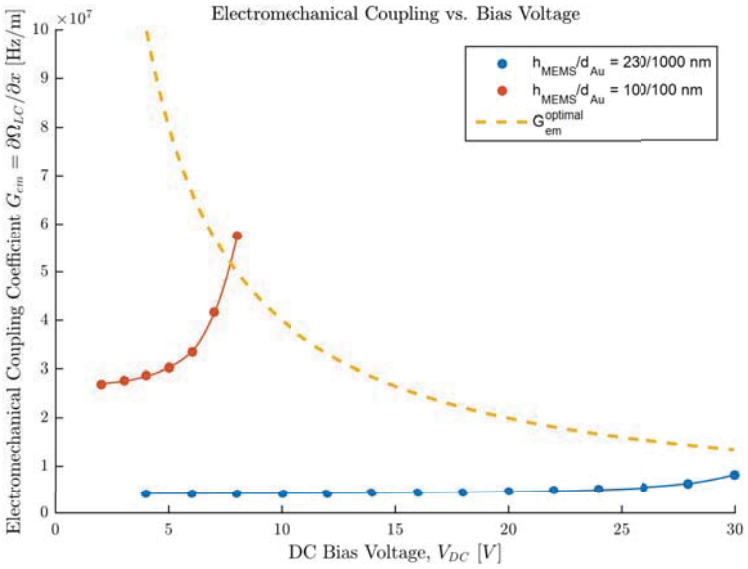

Figure 51: G_{em} vs. V_{dc} comparison between the original and modified electrostatic geometries. The optimal coupling parameter value, plotted in orange given the revised parameters in Table 3, is only met by the modified geometry.

optimized geometry is an improvement in capacitance tuning. Figure 51 illustrates that this enhancement enables the realization of optimal electromechanical coupling. Based upon the limits of fabrication, the geometry could be further modified to improve the coupling strength.

E.4 Summary

In this section, we compared the simulation-derived electromechanical coupling coefficient G_{em} to its optimal value set by Equation 43. Since the simulated coupling coefficient does not obtain the optimal value for either the bare or enhanced parameters established in Tables 2 and 3, respectively, two alternative optimization methods are investigated: 1) readjusting the ratio of capacitance to inductance in the *LC circuit* and 2) revising the microbridge geometry. Both of these methods are shown to improve G_{em} enough to achieve the optimal coupling value, thus maximizing transduction gain and minimizing the resulting V_π.

Appendix F Comparison of Electrostatic Actuation Techniques

As opposed to direct electrostatic actuation using a bridge and side electrode, the Kelvin polarization-force based geometry can be utilized to electrostatically actuate the microbridge [22]. By conducting a DC bias study of this geometry with a 100 micron bridge, the scheme's efficiency can be compared to that of direct electrostatic actuation. The results, shown in Figure 52, indicate that the default gradient electric field actuation geometry is a less apt technique for sensitive transduction applications. Not only are the DC bias and required energy an order of magnitude greater than those of the direct actuation geometry, but the capacitance tuning is also significantly degraded.

The actuation efficiency can, however, be improved by moving the bias electrodes closer together. Figure 53 depicts the improved performance that results as the separation decreases from the default value of 4 microns – the pull-in bias is significantly reduced, and the capacitance tuning increases significantly. An exception to this general trend of improvement exists between the displacements of 4 and 5 microns, which could be an artifact of the FEM simulation conducted. Despite the improvement, the coupling strength of the direct actuation scheme still dominates the polarization-based technique.

The predominant advantage of a Kelvin polarization force-based geometry is the noninvasive actuation – no electrode, and therefore bias probe, needs to be mounted onto the bridge [30]. The bridge's Q-factor is therefore preserved, and the actuation technique can be used on an array of arbitrary MEMS geometries [4, 22]. For our application, the degradation of the mechanical resonator resulting from the application of an electrode and bias probe should be carefully analyzed in order to determine it's significance – if it induces a substantial performance decay, the polarization-based actuation scheme may yield a more feasible technique.

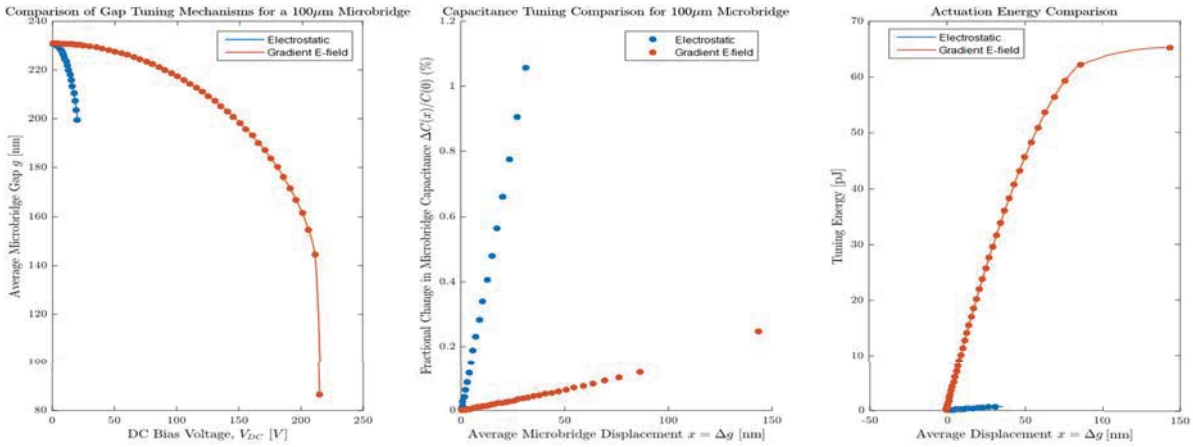

Figure 52: DC bias study comparison between direct electrostatic actuation, and Kelvin polarization force-based actuation. The decreased pull-in voltage, increased capacitance tuning, and decreased energy required favor the implementation of direct electrostatic actuation for a RF-to-optical transduction application.

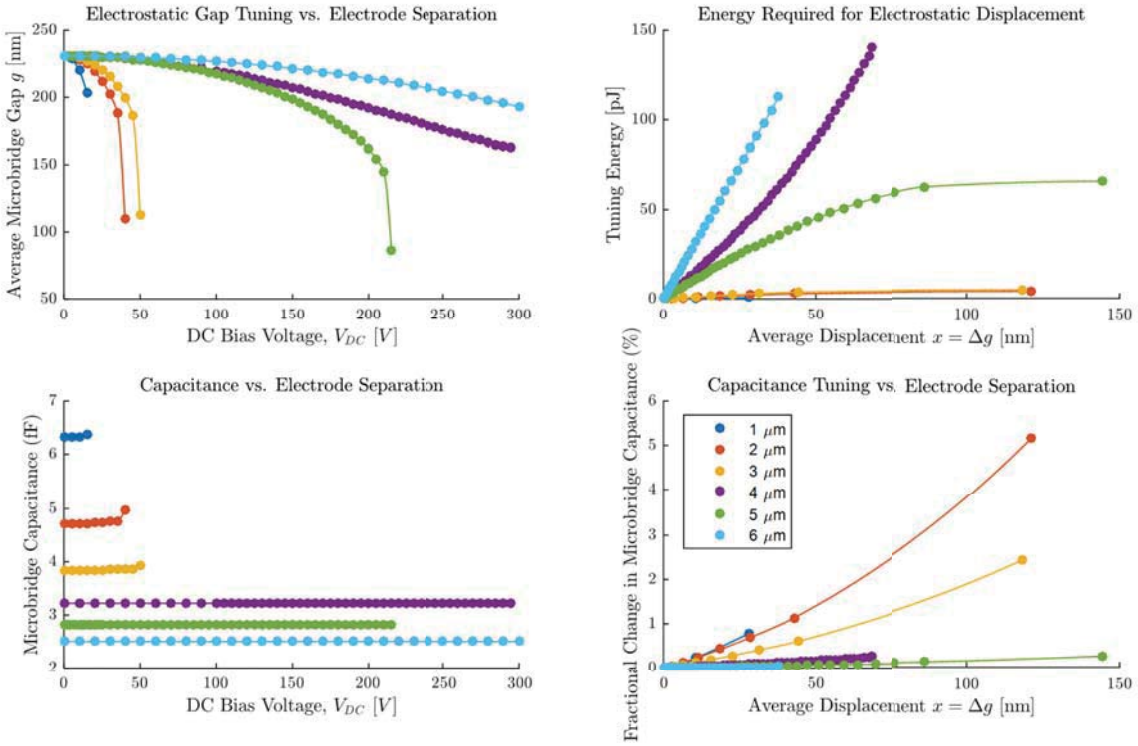

Figure 53: DC bias study results for the Kelvin polarization force-based actuation scheme for variable displacements between the two side electrodes. In general, as the electrodes are placed closer together, the architecture becomes more suitable for efficient displacement at lower bias voltages as well as stronger electromechanical coupling.

Appendix G Microbridge Design Optimization

The doubly-clamped microbridge used for these investigations suffers from several drawbacks. The two suspension points, for example, prevent the bridge from having a uniform deflection profile along its length, which results in a undesired variation in the optical effective index across the length of the optomechanical interaction region. Furthermore, the doubly-clamped architecture yields a non-optimal pull in voltage and requires specially designed supports to avoid interference with the waveguide placed below the suspended bridge. To address these limitations, an alternative cantilever-supported design was investigated. For this architecture, five 30 micron long, 0.75 micron wide, and 150 nm thick cantilevers – fixed at one end to a side support and connected to the suspended microbridge at the other – we placed at uniform intervals on each side along the length of the bridge.

Due to the reduced spring constant of the cantilevers compared to the spring constant of the original doubly-clamped bridge, an applied bias results in a greater deflection across the length of the cantilevers than across the microbridge, yielding a more uniform displacement across the length of the microbridge. Figure 54, which compares the two designs, demonstrates that the central (center 10%, or 10 microns for a 100 micron-long bridge) displacement is reduced to under 20% of its original value when the cantilever design is implemented. Additionally, the pull-in voltage is reduced by an order of magnitude, indicating that, for a constant applied voltage, a greater displacement is induced in the optimized structure than in the original. The overall transduction gain, which is a function of the electrostatic coupling efficiency, is therefore improved. Overall, this experiment demonstrates that a judicious choice of perturber design parameters can significantly improve transduction efficiency.

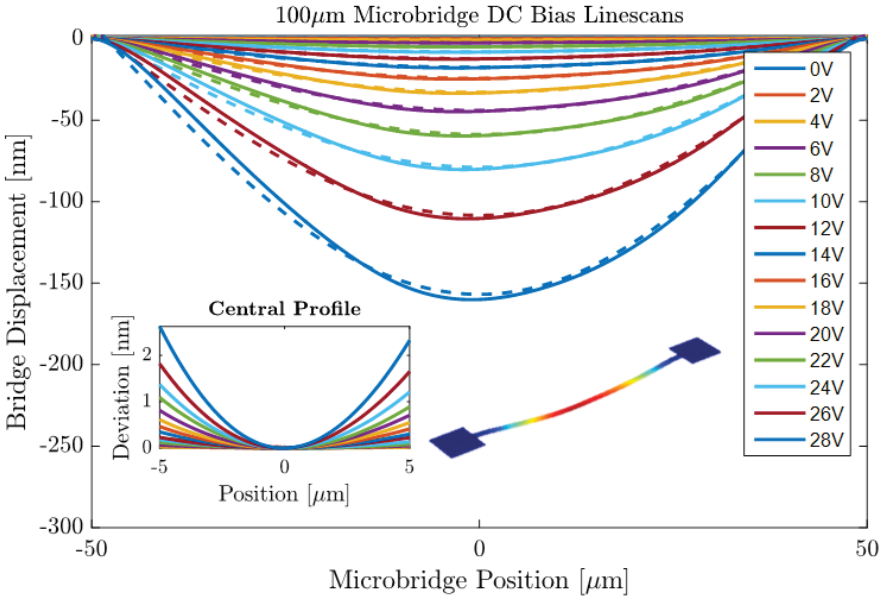

(a) Original doubly-clamped beam.

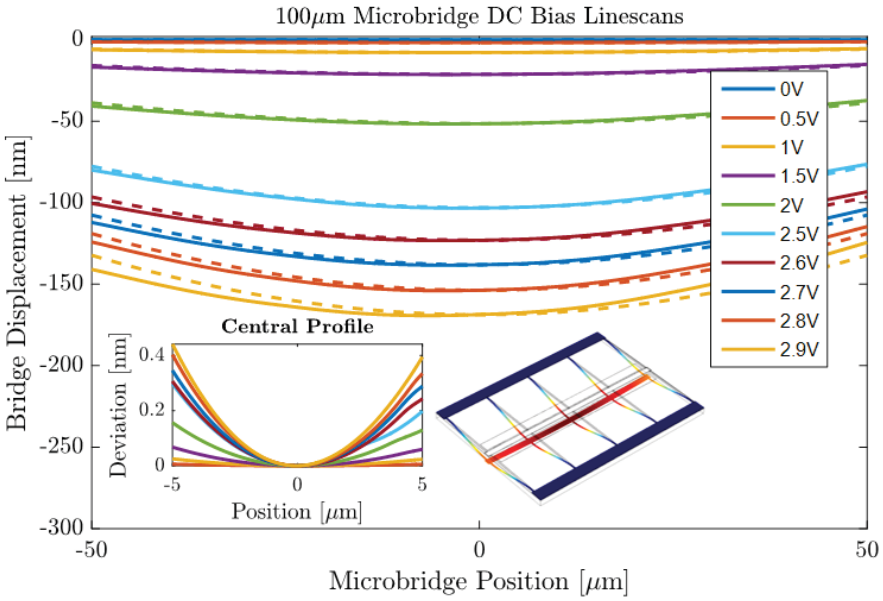

(b) Optimized cantilever-suspended beam.

Figure 54: FEM simulated displacement profiles for an electrostatically actuated 100 micron doubly-clamped beam suspended 230 nm above the substrate (a). Within the central 10 microns, the height varies by less than 3 nm. To achieve a flatter bridge profile, a cantilever-suspended beam design was created with ten 30 micron-long cantilevers (b), yielding nearly an order of magnitude reduction in both actuation voltage and height variation with the central region.

Appendix H Optomechanical Coupling Optimization

The optomechanical coupling parameter $G_{om} \equiv \frac{\partial n_{\text{eff}}}{\partial x}$ dictates the effectiveness of the microbridge effective index tuning mechanism. Since the half wave voltage of the mechanically mediated transducer is inversely proportional to G_{om}, we explore the optimization of this coupling parameter by analyzing 1) the waveguide dimensions, 2) the perturber characteristics, and 3) the addition of a field-enhancing high-index film to the waveguide.

H.1 Waveguide Optimization

By varying the dimensions of the silicon nitride waveguide, we can determine the waveguide size that minimizes the optical confinement, defined by the ratio of the optical energy density W integrated over the waveguide to that integrated over the entire mode area [13]

$$\Gamma = \frac{\iint_{\text{WG}} |W| dA}{\iint_{\text{mode}} |W| dA}. \tag{48}$$

When this ratio is minimized, the percent of optical power in air is maximized, leading to optimum index tuning efficiency since the microbridge interacts with a larger evanescent field.

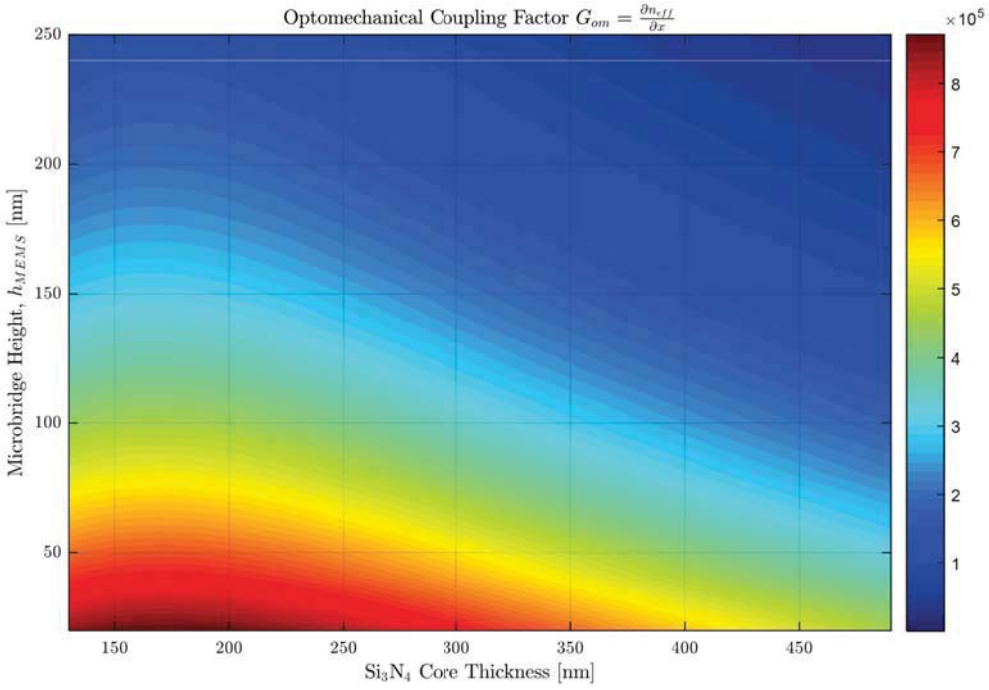

Figure 55: The optomechanical coupling factor G_{om} as a function of the waveguide core thickness and the microbridge-waveguide gap. A constant 31% etch depth is assumed. Note that the coupling is maximized for a waveguide core thickness of approximately 175 nm. The maximum value is on the order of 10^6 m^{-1}.

Parametric sweeps of the rib waveguide core thickness, etch depth (as a percentage of the core thickness), and core width were conducted. While the etch depth and core width had little effect on the tuning performance, varying the waveguide core thickness yielded a significant change in

the optical confinement. The results, shown in Figure 55, confirm the previous determination [11] of an optimal core thickness $t_{\text{Core}} \approx 170$ nm.

H.2 Perturber Optimization

Similarly, the dimensions of the microbridge perturber can also be varied to determine their effect on G_{om}. Increasing the microbridge thickness t_{MEMS}, for example, lends to a corresponding improvement in optomechanical coupling as shown in Figure 56. However, the thickness of the perturber cannot be increased without bound since beyond a critical thickness the microbridge becomes an independent waveguide and can itself support a propagating optical mode, yielding significant optical loss [12].

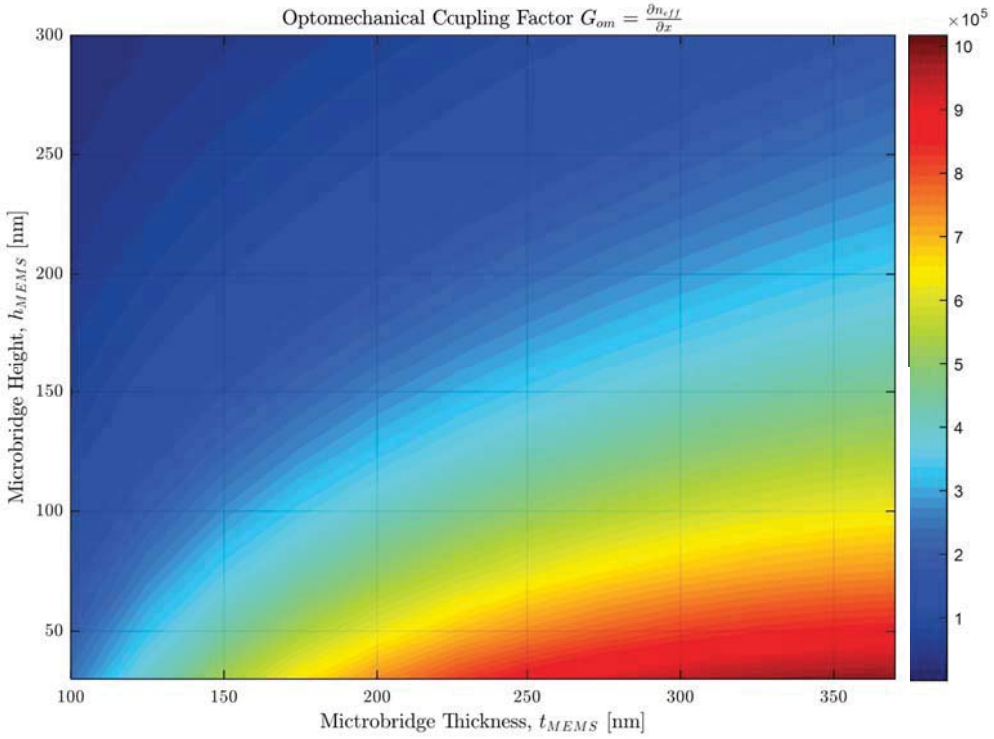

Figure 56: As the perturber's thickness increases, the optomechanical coupling increases, as more optical power from the waveguide's evanescent field is confined within the microbridge.

H.3 Thin Film High-Index Cladding

The percent of optical power in air, and thus the efficiency of the microbridge coupling to the evanescent field, can also be optimized by coating the waveguide with a thin high-index film. This technique has been successfully implemented in previous evanescent field sensing devices, and has been found to increase the peak intensity of the electric field at the waveguide-air interface by an order of magnitude [45, 46].

The results of our mode simulations, shown in Figure 57, confirm this experimental conclusion. Figures 58 and 59 depict the resulting enhancement in the optomechanical coupling factor when a thin film coat ($n = 4.0$) of variable thickness is applied to the waveguide. A peak improvement in

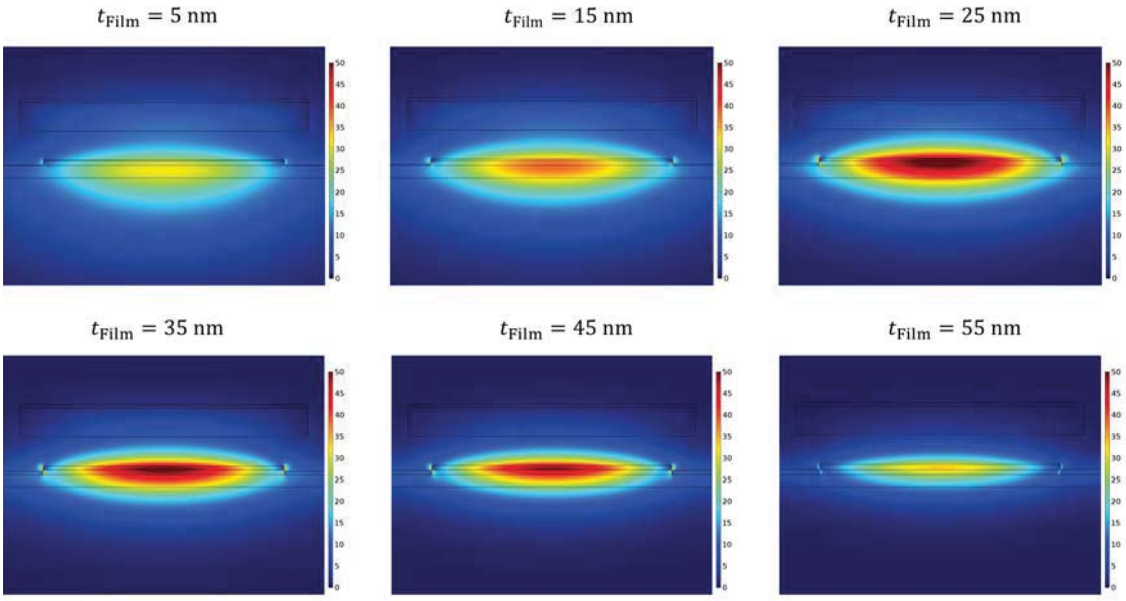

Figure 57: Optical mode profiles (electric field magnitude) for varying thicknesses of high-index ($n = 4.0$) waveguide film coating. As the thickness increases to its optimum value, the mode is "pulled" up into the air, and the peak electric field magnitude intensifies. For thicknesses greater than the optimal value of ∼40 nm, the film becomes a new waveguide core and the peak intensity decreases.

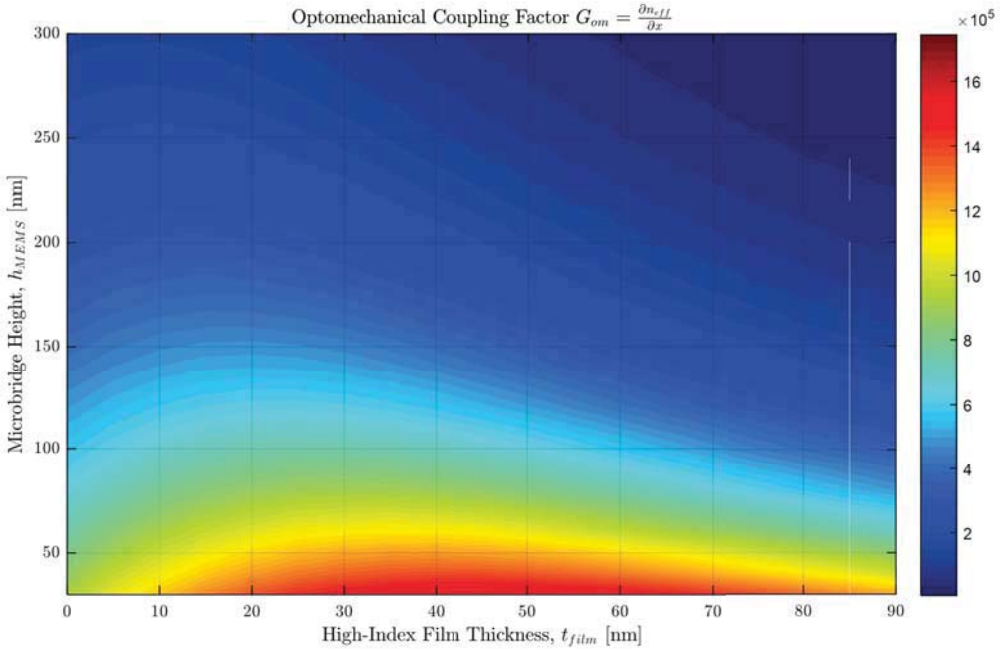

Figure 58: G_{om} plotted as a function of microbridge height for various thicknesses of high index film ($n = 4.0$). The film effectively "pulls" the optical mode upwards, and optimizes the percentage of optical power in air. For greater than optical thicknesses ($t_{\text{film}} < 40nm$), the efficiency decreases since the high index film begins to support the optical mode, thus becoming the new waveguide core.

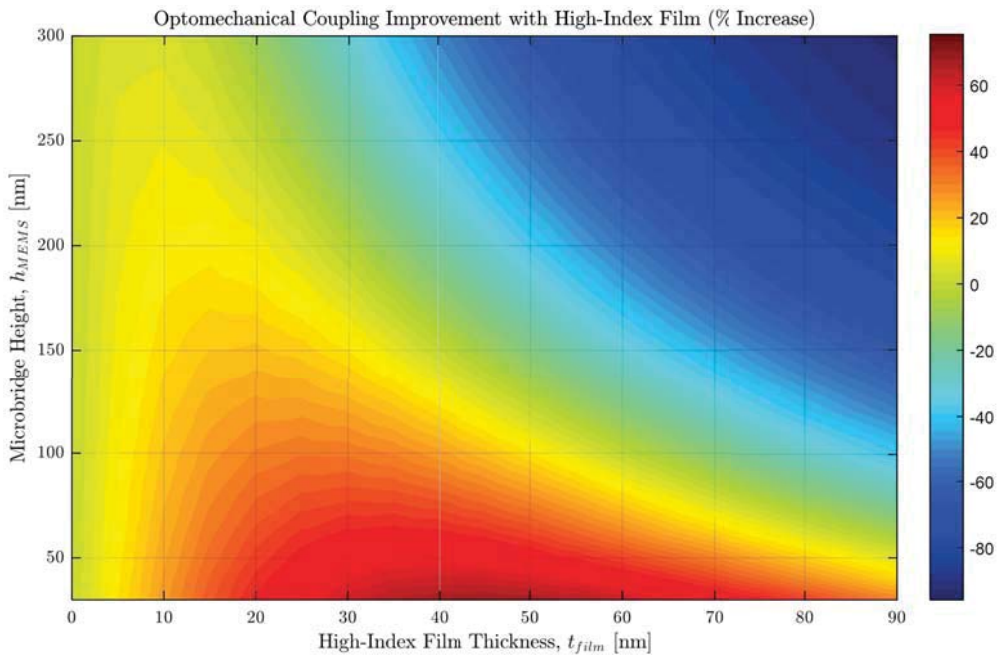

Figure 59: For the optimal thickness of approximately 40 nm, the peak value of the optical coupling coefficient increases by over 60% through the application of a high index ($n = 4.0$) waveguide coating film. However, for waveguide-perturber gaps greater than ∼200 nm, the application of the high-index film actually reduces transduction sensitivity.

G_{om} of over 60% for a 40 nm thick film was found, thus confirming the validity of the technique to maximize the optomechanical coupling performance.

Appendix I Experimental Challenges – Stiction Failure

Prior to experimental testing, the development of theoretical device transfer functions enabled the exploration of optimum RF-to-optical transduction performance for two different systems, one with an LC resonator and one without. Furthermore, computational simulations verified the feasibility of achieving the optimal bias point required for peak transduction gain. Having completed these analysis, we now explore the experimental characterization of fabricated devices.

Originally, an existing fabricated electro-optomechanical chip used in previous studies, was to be re-purposed for these experiments. Prior to electrically actuating the devices or conducting any optical testing, an optical profilometer was used to characterize the structural integrity of the previously used devices. Profilometry scans of each bridge revealed that all of the previously usable microbridges had been pulled into contact with the underlying waveguides, and were bonded to them by internal forces. This failure mechanism, commonly known as "stiction," has been cited as a common mode of failure for MEMS devices [38, 39]. Sample results from the optical profilometry testing are shown in Figure 60, which contrasts the flat bridge elevation profile of a suspended bridge to the bowed profile of a stiction-failed bridge.

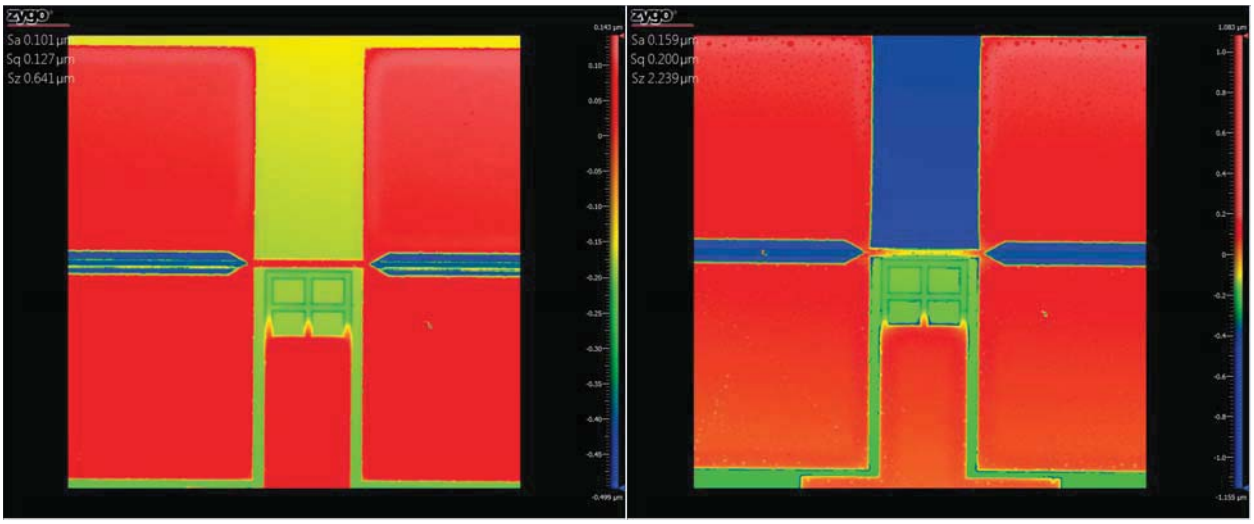

(a) Suspended Bridge (b) Stiction Failed Bridge

Figure 60: Optical profilometry scans of 40 micron long microbridge which was initially suspended (a) and subsequently experienced stiction-induced failure (b), which can be noted by the depressed bridge elevation throughout the length of the bridge.

To conduct any further testing, suspended bridges were required. Several attempts to repair the stiction-failed bridges were thus conducted using a variety of techniques. Initial trials consisted of applying a downward-sloping linear frequency modulated chirp RF signal to the bridge, an idea proposed in [40]. In this fashion, the initially high frequency of the signal would match the resonant frequency of the "unstuck" portion of the bridge, thus effectively vibrating it and potentially decreasing the length of the stuck portion of the bridge. The decreasing frequency would then continue to match the resonant frequency of the lengthening suspended beam until the bridge was completely unstuck. However, this technique prove ineffective for the failed devices, as the bridges were almost completely adhered to the underlying waveguide. Another alternative repair technique

attempted was heating the devices with a hot plate. The thermal expansion expected from heating would further tension the bridge, and possibly provide the restoring force required to unstick the bridge. Despite heating to 110°C, this technique failed to free any bridges. Other published repair techniques, such as laser-induced stress wave recovery [41, 42], were not pursued due to lack of required equipment. Finally, the sample chip was immersed in a isopropyl alcohol and placed in an ultrasonic bath in an attempt to vibrate the MEMS microbridges free. After a one hour sonication, the sample was dried with a critical point dryer, and the bridge profiles were subsequently reevaluated with the Zygo optical profilometer.

Although this final technique led to the repair of one device, fabrication of a new sample was pursued as an alternative course of action.

Appendix J Experimental Challenges – Electrical Pickup Isolation

When the bias probes were connected to the initial microbridge devices as shown in Figure 28, a large amplitude, low frequency oscillation was noted in the the optical output even when no bias voltage – DC or RF – was applied. By taking a discrete Fourier transform of the photodetector output sampled by the benchtop digital multimeter, we were able to determine that the pickup consisted primarily of 60 Hz noise and its associated higher frequency harmonics (blue spectrum in Figure 61a).

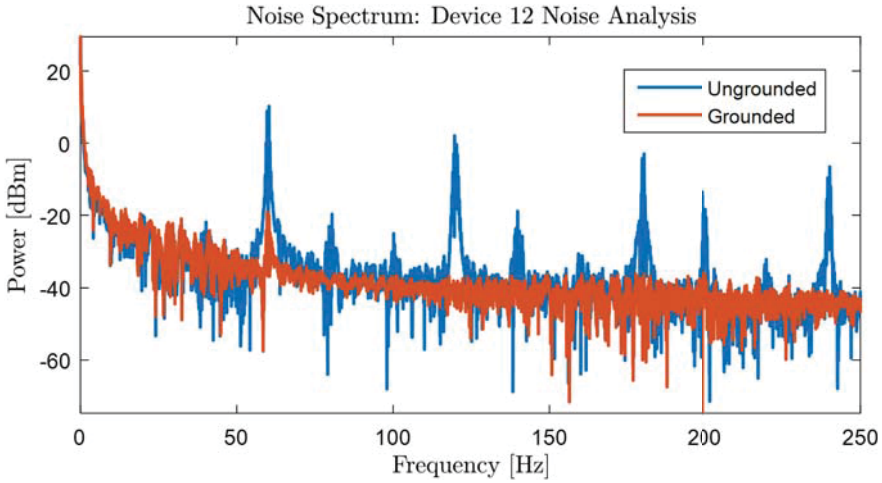

(a) Device 12 (75 micron bridge; probes connected) noise spectrum with and without optical table grounded.

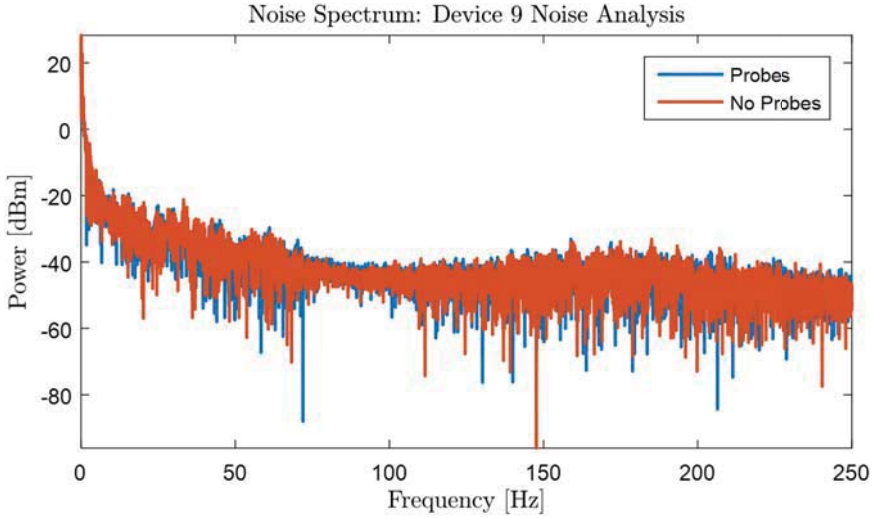

(b) Device 9 (50 micron bridge) noise spectrum with and without probes connected.

Figure 61: (a) When bias probes were connected the device, 60 Hz electrical pickup was modulated onto the optical output. This signal was significantly attenuated when the electrically-floating optical table was grounded to the benchtop DC bias source (red curve). (b) Further isolation provided by aluminum foil shielding placed around open electrical components yielded minimal noise variation between the output with and without probes connected.

In the process of measuring the floating potential of various objects throughout the room, the optical table was found to be electrically-floating with an RMS voltage of nearly 0.4V. After connecting the metal table to the ground port of the DC bias source, thereby tying the entire lab apparatus to the building's AC ground, the optical response to the pickup was attenuated by nearly 30 dB (red curve in Figure 61a).

Aluminum foil was then wrapped around the exposed ground connections of the electrical bias instruments and components to further reduce the electrical pickup. The final result, depicted in Figure 61b, was a nearly identical noise level in the optical output when the electrical probes were either connected or disconnected. While this noise issue emerged as a experimental challenge, it also demonstrated the viability of the intended device functionality – optical detection of low-frequency electrical signals.